

Enhancement of Biomolecule Binding on Biosensors Using AC Electrokinetics

A Thesis

Submitted to the Faculty

of

Drexel University

By

Robert Weisbein Hart

In partial fulfillment of the
requirements for the degree

of

Doctor of Philosophy

February 2010

© Copyright 2009

Robert Weisbein Hart. All Rights Reserved

ACKNOWLEDGEMENTS

I would like to express my gratitude to the many people who provided me with guidance and support throughout my tenure as a Ph.D. student. Their assistance has made the attainment of my degree possible.

First, I would like to thank my two advisers, Dr. Hongseok (Moses) Noh, and Dr. Ryszard M. Lec for their mentorship both in technical realms and philosophical. Their stewardship has changed the way I approach research and the world as a whole and their contributions to this thesis are greatest among my many supporters.

Second, I am grateful to my committee members, Drs. Kambiz Pourrezaei, Kenneth Barbee, Timothy Kurzweg and Dr. Cameron Abrams who have always made themselves available for advice and who have contributed many concrete improvements to my research.

Third, I would like to express my appreciation to my graduate student colleagues who have been selfless with their time in training me, providing me with technical assistance and in supplying aid in other countless ways. These colleagues include Dr. Johann DeSa, Dr. Ertan Ergezen, Dr. Marek Swoboda, Himanshu Mehta, Nishit Mehta, Mark Mattiucci, Doh-hyoung Lee, Jonghyun Oh and Jorge Capurro.

Finally a special thanks to my wife Jessica and son Jacob who provide me with moral support and affection.

TABLE OF CONTENTS

ACKNOWLEDGEMENTS.....	iv
TABLE OF CONTENTS.....	v
LIST OF TABLES.....	xi
LIST OF ILLUSTRATIONS.....	xii
ABSTRACT.....	xxiv
CHAPTER 1: INTRODUCTION & BACKGROUND.....	1
1.1 Thesis Organization.....	1
1.1.1 Article-based Thesis.....	1
1.2 Motivation and Approach.....	3
1.3 Specific Aims.....	6
1.3.1 Aim 1: Characterize AC electrokinetic forces in a microchannel.....	6
1.3.2 Aim 2: Evaluate the effect of AC electrokinetics on transport-limited heterogeneous immunoassays.....	8
1.3.3 Aim 3: Quantify the effect of AC electrokinetics on a biosensor system.....	8
1.4 Background & Literature Review.....	9
1.4.1 The transport-limited system – a major source of long detection times in biosensor systems	9
1.4.2 Background on antibodies – the essential component in immunoassays.....	10

1.4.3	Enzyme Linked Immunosorbent Assay (ELISA) – the current gold standard	12
1.4.4	Fluorescent Immunoassays	13
1.4.5	Background on Florescein, the fluorophore used	13
1.4.6	Microfluidics history and background	15
1.4.7	AC Electrokinetics background	17
1.4.8	Alternative Mixing Techniques	24
1.4.9	Finite Element Models of AC Electrokinetics	37
1.4.10	Fundamentals of Biosensors	42
CHAPTER 2: COMPREHENSIVE ANALYSIS OF PARTICLE MOTION UNDER NON-UNIFORM AC ELECTRIC FIELDS IN A MICROCHANNEL		48
2.1	Problem Statement	48
2.2	Introduction to AC Electrokinetics	48
2.2.1	Brief Overview of AC Electrokinetic Phenomena	50
2.3	Theoretical description of AC Electrokinetic Forces	52
2.3.1	Dielectrophoresis	52
2.3.2	AC Electroosmosis	57
2.3.3	Electrothermal Effects	59
2.4	Experimental Observations of Microparticles in Nonuniform Electric Fields	61
2.4.1	Experimental Method For Observation of Microparticles In The Presence of AC Electrokinetics	61
2.4.2	Characterization and Analysis of Particle Behaviors	67

2.5	Finite Element Model of AC Electrokinetic Forces.....	83
2.5.1	Description of the Finite Element Simulation.....	83
2.5.2	Discussion of the Simulation Results.....	88
2.6	Conclusions.....	101
CHAPTER 3: ENHANCEMENT OF HETEROGENEOUS IMMUNOASSAYS USING AC ELECTROOSMOSIS		102
3.1	Problem Statement	102
3.2	Introduction to the use of ACEO to alleviate transport limitations	102
3.2.1	AC Electroosmosis overview.....	106
3.2.2	Description of an Immunoassay Surface Reaction	106
3.3	Finite Element Simulation of an Immunoassay in the Presence of AC Electroosmosis	109
3.3.1	Description of the Finite Element Simulation.....	109
3.3.2	Simulation results.....	112
3.4	Use of ACEO to Improve Fluorescent Immunoassays	117
3.4.1	Immunoassay Experimental Method	117
3.4.2	Fluorescent Assay Results	120
3.4.3	Surface Concentration Nonuniformity.....	126
3.5	Conclusions.....	133
CHAPTER 4: IMPROVED PROTEIN DETECTION ON AN AC ELECTROKINETIC QUARTZ CRYSTAL MICROBALANCE		135

4.1	Problem Statement	135
4.2	Introduction.....	135
4.2.1	AC electroosmosis	137
4.2.2	The transport limited system.....	138
4.2.3	Quartz crystal microbalance.....	139
4.3	Materials and methods	139
4.3.1	QCM modification	139
4.3.2	Measurement system and calibration.....	140
4.3.3	Antibody adsorption assays	141
4.4	Results and Discussion	143
4.4.1	Electrical testing and calibration.....	143
4.4.2	Antibody sensor detection.....	146
4.4.3	Immunoassay on glass IDEs	148
4.4.4	Electrode damage at high voltages.....	149
4.5	Conclusion	151
CHAPTER 5: CONCLUSION & FUTURE WORK		152
5.1	Specific Aims.....	153
5.1.1	Aim 1: Characterize AC electrokinetic forces	153
5.1.2	Aim 2: Evaluate the effect of AC electrokinetics on transport-limited heterogeneous immunoassays	153
5.1.3	Aim 3: Quantify the effect of AC electrokinetics on a biosensor system	154

5.2	Contributions.....	155
5.2.1	Contributions from CHAPTER 2:COMPREHENSIVE ANALYSIS OF PARTICLE MOTION UNDER NON-UNIFORM AC ELECTRIC FIELDS IN A MICROCHANNEL	155
5.2.2	Contributions from CHAPTER 3:ENHANCEMENT OF HETEROGENEOUS IMMUNOASSAYS USING AC ELECTROOSMOSIS	157
5.2.3	Contributions from CHAPTER 4:IMPROVED PROTEIN DETECTION ON AN AC ELECTROKINETIC QUARTZ CRYSTAL MICROBALANCE	158
5.3	Future work.....	160
5.3.1	Improvements to modeling and predictive tools.....	160
5.3.2	Exploration of the protein patterning effects	161
5.3.3	Other means of micromixing	161
5.3.4	Sensor and application-driven development.....	162
	REFERENCES	165
	APPENDIX I - AC ELECTROKINETIC QCM PROTOTYPES	172
	APPENDIX II - MICROFABRICATION TECHNIQUES.....	174
	APPENDIX III - FLUORESCENCE IMAGE ANALYSIS.....	176
	APPENDIX IV – INTER- AND INTRA-DEVICE BINDING VARIABILITY	178
	APPENDIX V – RELATIVE BINDING CAPACITY OF NONSPECIFICALLY ADSORBED IGG ON GOLD AND GLASS	181

APPENDIX VI - FURTHER DISCUSSION ON THE POSSIBLE INFLUENCE OF DEP ON IGG BINDING	183
APPENDIX VII - PSEUDOCODE FOR RESONANCE FREQUENCY MEASUREMENT SOFTWARE IN LABVIEW	190
APPENDIX VIII - COMSOL MATLAB CODE FOR ACEO-ENHANCED BINDING FOR HETEROGENEOUS IMMUNOASSAYS	192

LIST OF TABLES

Table 2-1 Comparison of dielectrophoresis (DEP), AC-electroosmosis (ACEO), and electrothermal effect (ETE). 56

Table 3-1: Binding Constants for the simulation. George *et al.* used immobilized saporin and free IgG as the analyte. Hu *et al.* used generic immunoassay values. Huang *et al.* used immobilized C reactive protein (CRP) and free IgG as the analyte. Vijayendran *et al.* used immobilized anti – TNT antibodies with free trinitrobenzene (340 Da molecular weight) 116

LIST OF ILLUSTRATIONS

Figure 1-1: Thesis Structure & Function	2
Figure 1-2: Thesis concept diagram. (1) Shows a typical transport rate-limited surface reaction. Receptors bound on a solid surface react with analyte in solution. Slow analyte diffusion, fast surface reaction and large diffusion distances cause inordinately long reaction times. Mixing the solution can help reduce transport limitations. (2) High strength non-uniform electric fields can cause particle and fluid motion and is known as AC Electrokinetics. (3) The use of AC Electrokinetics to enhance transport rate-limited reactions by stirring the bulk solution and bringing fresh analyte to the surface for reaction.	5
Figure 1-3: Antibody structure and ELISA. (a) Shows the structure of an Immunoglobulin G. (b) shows a typical Indirect ELISA and (c) shows a Sandwich ELISA. Other types include Competitive ELISA and Reverse ELISA	12
Figure 1-4: Image of a spiral capillary etched into 2 inch dia silicon wafer to serve as a gas chromatography column made in a landmark work by Terry et al.	16
Figure 1-5: An electrokinetically-driven capillary electrophoresis chip developed by Agilent. ...	17
Figure 1-6: Diagram of a (a) uniform and (b) nonuniform electric field.	18
Figure 1-7: Charge movement at the electrode surface resulting in ACEO flow patterns.....	19
Figure 1-8: Dielectrophoresis causes particles to be attracted to or repulsed from high electric field strength. Negative DEP is when the particle is repulsed and positive DEP is when the particle is attracted to high electric fields.	20

Figure 1-9: Electrothermal effect. Left: thermal gradients formed by Joule heating. Right: resulting fluid flow [26].	22
Figure 1-10: Several popular AC electrokinetic device patterns. (a) A set of parallel straight electrodes where the electrode width is half of the pitch distance. (b) shows a similar device where the pitch is the same but the electrode is wider. (b) and (c) show different size castellated electrodes. (e) Shows a quadropole electrode (adjacent electrodes are 180° out of phase). (f) shows a potential-well pattern.....	23
Figure 1-11: Schematic of the micromixing device used by Lynn <i>et al.</i> [33].....	27
Figure 1-12: Device design for a chaotic DEP micromixer [36].	28
Figure 1-13: Device design and simulation for Fiedman <i>et al.</i> Numerical simulations show the relative concentration of streptavidin within the channels. [38]	29
Figure 1-14: (a) Fresnel annular sector actuator (FASA) transducer[39]. (b) Linear array of FASA transducers to generate bulk channel flow [40]. (c) Rotational array of FASA devices for vortex generation. [40]	31
Figure 1-15: Resonant mode hopping device. (a) & (b) show the channel geometry and cross- section respectively. (c) shows top-down images mixing two streams. Mode hopping was employed at two different frequencies for 5s each. [41]	32
Figure 1-16: SAW mixer from Sritharan <i>et al.</i> (a) A schematic and image of acoustic streaming. LiNbO ₃ with an IDT is coupled to a plastic chip which contains a microchannel. Quick and short actuation of the IDT causes a jet of dye to enter into the water layer. (b) A design using the SAW device to mix two streams in a simple Y-channel. (c) An image of distributed particles that have been mixed by the SAW device. The image was 2.5 mm downstream	

from the IDT. Without IDT actuation, mixing was incomplete even at 25 mm downstream. [42]	33
Figure 1-17: (a) Conceptual diagram of a bubble actuator. (b) Images of red dye being mixed by a bubble actuator. (c) A schematic showing an array of air pockets within a chamber. [45].	35
Figure 1-18: Two-dimensional serpentine channel and perpendicular electrodes for chaotic mixing.[46]	36
Figure 1-19: (a) Schematic of a micro stir bar contained within a channel. (b) Image of a stir bar within a Y-channel. (c) Stir bar mixing dye and water streams. [47].....	37
Figure 1-20: Example force mapping simulation result and a comparison of particle observations under the same conditions.	39
Figure 1-21: (left) ACEO mixing in a microchannel compared to (right) static binding of IgG on a functionalized surface. The colors represent the concentration of analyte (red is highest and blue is lowest).....	41
Figure 1-22: Schematic of general biosensing steps.....	42
Figure 1-23: Equivalent electrical circuit for a QCM operating in a vacuum.....	45
Figure 1-24: S ₂₁ gain and phase response of an unloaded QCM.	46
Figure 1-25: Equivalent electrical circuit of a loaded QCM. [49]	47
Figure 2-1. Predominant AC electrokinetic behaviors. (a) Dielectrophoresis (DEP), (b) AC electroosmosis (ACEO), and (c) Electrothermal effect (ETE). AC electrokinetic particle manipulation is readily achieved in a microchannel via non-uniform electric fields generated	

by microfabricated planar electrodes. High electric fields required for particle motion ($10^4 \sim 10^6$ V/m) can be easily achieved with only a few volts since the electrode gap is micro- or nanoscale. The electrolysis of water is avoided since AC power is applied. Moreover, each of the electrokinetic and electrohydrodynamic (EHD) forces has fairly distinct characteristics and as a result various types of particle motion can be achieved by simply varying operational conditions [71]. This convenience and versatility make AC electrokinetics the most suitable particle manipulation technique for microfluidic devices compared with other techniques such as optical tweezers[72-73], ultrasonic techniques[74], and magnetic techniques[75-77].

..... 49

Figure 2-2. Clausius-Mossotti factor as a function of frequency and media conductivity for (a) a solid 2 μm diameter polystyrene sphere (particle permittivity= $2.5\epsilon_0$) (b) a solid 200 nm diameter polystyrene sphere (particle permittivity= $2.5\epsilon_0$), and (c) a shell structure modeled on Chlorella sp. (surface capacitance= $12.4\text{E-}3$ S, radius= $3.29\text{E-}6$ m, inside conductivity= $8\text{E-}3$ S/m, inside permittivity= $150\epsilon_0$) 9 54

Figure 2-3. Using equation (5), AC electroosmotic velocity is plotted as a function of (a) Ω at different locations (x) from the electrode edge and (b) frequency and distance (x) from the electrode edge at 0.0002 S/m, 1 V, and 20 μm gap between electrodes..... 59

Figure 2-4. Π of ETE as a function of frequency with three different conductivities. 60

Figure 2-5. 3D simulation for (a) Parallel interdigitated, (b) Castellated, (c) Pocket well and (d) Quadrupole electrodes at $0.354 V_{\text{rms}}$. (Surface plot: $\text{Log}_{10}(\nabla|E_{\text{rms}}|^2)$ [V^2/m^3] , Arrow: Electric field [V/m]). In the castellated electrode plot, a small normalized arrow plot at the corner

- shows the electric field direction 1 μm off the surface of the substrate. Black areas are the electrodes and the white area is the inter-electrode space. 63
- Figure 2-6. (a) An image of an assembled device. Conceptual drawings of the four electrode types, (from left to right) parallel interdigitated, castellated, potential well and quadrupole are shown. (b) Geometry (cross-sectional view of the microchannel) and boundary conditions for numerical simulation. For the electrostatics simulation: Zero charge on 1 and 4; $V_0 = V_{\text{rms}}/2$ on 2; $V_0 = -V_{\text{rms}}/2$ on 3; continuity for 5. For the convection and conduction simulation: Thermal insulation on 1; zero heat flux on 4 and 5; and fixed temperature on 2 and 3. For the incompressible Navier-stokes simulation: 0 pressure on 4; No slip on 1; slip velocity (electroosmotic velocity) on 2 and 3; and symmetry conditions on 5. (c) Simulation strategy flow chart..... 66
- Figure 2-7. Parallel interdigitated electrodes with 2 μm diameter polystyrene microbeads at 1 kHz and 1 V suspended in 0.0002 S/m media with (a) low concentration of particles and (b) high concentration of particles 70
- Figure 2-8. Experimental results at selected frequencies and voltages for the parallel and castellated interdigitated electrodes using two different conductivities. 2 μm diameter polystyrene microspheres were randomly dispersed before a signal was supplied..... 73
- Figure 2-9. Experimental results at selected voltages and solution conductivities for the quadrupole and pocket well electrodes. 2 μm diameter polystyrene microspheres were randomly dispersed before a signal was supplied. 79

- Figure 2-10. Experimental results at selected frequencies and voltages for the quadruple and pocket well electrodes using two different conductivities. 200 nm diameter polystyrene microspheres were randomly dispersed before a signal was supplied. 82
- Figure 2-11. Mapping of each force isolated from the others at 1 kHz. The surface plot uses a logarithmic scale with force streamlines. 90
- Figure 2-12. Total force simulation results. Each surface plot represents the log of the force acting on a 2 μm particle at rest. Force streamlines are shown as well as normalized arrows which show the direction of the force at each location. Corresponding experimental results are showed inlaid on each simulation plot. 91
- Figure 2-13. Relationship between the strength of each phenomena and the height of the center electrode is shown for several frequencies and conductivities. Since the force varies as a function of x as well, an average was taken across all x for each given y point so that only general relationships can be understood..... 95
- Figure 2-14. The magnitude of each force is shown as a function of frequency for four distances (displayed on each graph) above the electrode surface. As before, in order to eliminate x special variations, the x component is averaged across the entire electrode so that only general relationships can be understood and exact spatial values cannot be obtained. 96
- Figure 2-15. The magnitude of velocity for particles experiencing DEP and Drag is shown as a function of particle radius for four frequency and voltage settings (displayed on each graph). The force is averaged (as before) for all x , 1 μm above the electrode surface. It must be stressed that only general relationships can be learned from such analysis. Velocity caused by DEP was found by equating drag force and DEP force and solving for velocity. The

region in grey shows the area where deterministic particle organization by AC electrokinetics is overcome by thermal motion. 97

Figure 3-1: Diagram of an immunoassay performed with AC electrokinetic enhancement on a microelectrode. The concentration is indicated both by the antigen particles (orange) and the concentration field (red: high concentration, blue: low concentration). The fluid motion caused by ACEO is shown as blue arrows as well as the streamlines in the concentration field image. Red arrows indicate the force due to DEP and the antibodies are bound both on the surface of the electrode as well as on the glass substrate. 104

Figure 3-2: Top Left and Bottom: Simulation geometry and boundary conditions. The numerical simulation consists of a cross-section of an interdigitated electrode placed on one side of a microfluidic chamber. The model takes advantage of symmetry and repeating units and only considers one half of an electrode and gap. h , a and b are the channel height, electrode width and gap width respectively. x is the cross-sectional position starting from the center of the electrode gap. Boundaries are numbered and explained in the table to the right. Note that the reaction occurs only on the bottom surface (3 and 4). The reaction simulation is therefore inactive on all other boundaries. Equation details are described in section 2.3 on page 51. Top Right: Flow chart describing simulation scheme. The input parameters shown are important but not a complete set. For example, viscosity and density of the fluid are inputs for the fluid dynamics simulation but not shown in the diagram. 108

Figure 3-3: Concentration maps of a 100 μm wide electrode and 30 μm wide gap operating at 2 V_{pp} . The scale shows the relative concentration c/c_0 . Electrode position is indicated by the gray line under each map. Flow across the surface of this half of the electrode will be from right to left. The last concentration map is for an inactive electrode. 112

Figure 3-4: Geometry optimization. Left: Contour plot showing the improvement factor as a function of electrode and gap widths for a 100 μm chamber height. Right: Optimum geometry as a function of chamber height. For each chamber height, the ideal geometry was determined by finding the shortest time to reach equilibrium. Voltage was adjusted for each geometry so that the maximum electric field was the same regardless of the gap width. 113

Figure 3-5: Left: Equilibrium binding time as a function of frequency for a 100 μm chamber height using a 70 μm electrode width and a 30 μm gap width. The electric field was 100 kV/m. Highest velocities are near the 100 Hz range with the phenomena dying out in the kHz range. After 10 kHz, binding time is purely determined by diffusion. Right: Assay enhancement for four different sets of reaction constants. Improvement factors are calculated by comparing the equilibrium times for mixed and unmixed samples with a maximum electric field of 100 kV/m. For each chamber height, ideal electrode geometry (as shown in Figure 3) was used. An improvement factor of 1 means no improvement. 115

Figure 3-6: Two fluorescent assays were developed to test proof of concept for the ACEO mixer device. (a) shows a non-specific adsorption assay with FITC-IgG. (b) shows an immunoassay with a functionalized surface. 118

Figure 3-7: First and second row: Direct adsorption assay using 0.01 mg/ml FITC-IgG. The applied signal was $2 V_{pp}$ and varied in frequency (displayed above). The top row features electrodes that were 20 μm wide with a 20 μm edge-to-edge gap. The bottom image row shows electrodes that were 100 μm wide with a 25 μm edge-to-edge gap. Third row: Increasing voltage (displayed in V_{pp}) for direct adsorption of 0.01 mg/ml IgG. Solution conductivity was 2 $\mu\text{S}/\text{cm}$ and frequency was 100 Hz. Note the increasing fluorescence till 5 V_{pp} where electrode damage occurred. Bottom: Relative Fluorescence Unit (RFU) for the

respective images. The frequency chart (left) was taken from the 20 μm and using some images not shown above. For both charts, fluorescent intensity was measured both near the electrode finger ends and towards the center of the device, each shown in separate plots. .. 121

Figure 3-8: Binding of fluorescent secondary antibodies to IDEs. Images are on top and their respective fluorescent intensity is shown in the chart below. Numbers on top of each column indicates the enhancement factor which is the ratio of sample intensity compared to the unmixed functionalized surface (C). The blocked surface has been prepared with BSA only. The functionalized surface has been prepared first with primary antibody and then blocked with BSA. The mixed samples have been supplied with a 100 kV/m, 100 Hz electric field. Non-mixed samples received no electrical signal. The lower row contains images of the fully functionalized surface with mixing on different geometry electrodes, as well as an enlarged image of the 20 μm parallel electrode. These IDEs were supplied with the same signal as those of the top row. The 10 μm castellated device was serendipitously broken in many places during fabrication, allowing only sparsely activated electrodes. Such an activated electrode is shown in the dotted line. Note the 20 μm parallel electrode has been enlarged 5 times compared to the other images. 124

Figure 3-9: Surface Concentration Profiles for George et al constants. Left: Raw data shown for several time points ranging from 1 second to 512 seconds. Each time point is twice that of the former (eg. 1, 2, 4, 8... seconds). Right: The same data as on the left, but the value of the first point has been subtracted from each plot in order to view each time point on the same baseline. 127

Figure 3-10: Nonuniformity generated by a highly transport rate-limited system with no surface diffusion. 128

- Figure 3-11: Degree of nonuniformity caused by different surface diffusion coefficient values 129
- Figure 3-12: Rate of nonuniformity generated as a function of D_s 130
- Figure 3-13: Effect of various parameters on the normalized surface concentration nonuniformity after 512 seconds. The “Toy” system is highly transport rate-limited. 131
- Figure 3-14: Comparison of 20 μm castellated electrode after a direct adsorption assay with a 3D electric field simulation. The simulation side shows ∇E^2 , which is proportional to DEP force..... 133
- Figure 4-1: Left: a conceptual diagram of ACEO motion (blue arrows) produced by parallel interdigitated electrodes and its effect on analyte concentration (color map) which is removed from the bulk solution by a reaction at the bottom surface. Right: images of a standard QCM (left) and an EKQCM. Image of (left) an unmodified QCM and (right) a QCM that has been modified with a microelectrode pattern. The QCMs used were 1 cm in diameter and 167 μm in thickness. 136
- Figure 4-2: Electrical equivalent circuit of TSM sensor. C_0 : static capacitance of quartz, C_1 , R_1 and L_1 are intrinsic capacitance, resistance and inductance of quartz respectively. R_2 , L_2 represent the liquid loading. 144
- Figure 4-3: Frequency response of the QCM and EKQCM to varying aqueous concentrations of glycerin. A prediction made by the transmission line model (TLM) is in the final column group..... 145
- Figure 4-4: Sensor, protein assay and fluorescence imaging results. The chart shows the quantity of adsorbed protein using three different approaches. Note that the fluorescence series uses the secondary axis on the right and is the only method that can measure values from the

finger end. The others are bulk measurement techniques. The images show mixed samples, unmixed samples and a blank, which was not subjected to any fluorescent IgG. (EKQCM n=4, MicroBCA assay (unmixed n=4, mixed n=2), Fluorescence n=10). 146

Figure 4-5: Fluorescent immunoassays performed on IDEs with AC electrokinetic mixing. Two variations are shown on the normal three-step assay which is as follows: (1) 2 hour primary IgG incubation, (2) overnight 1% BSA blocking, (3) 2 hour secondary IgG incubation. Left: Images from immunoassays subjected to AC electrokinetic forces during either step 1 (primary IgG mixing) or step 3 (secondary IgG mixing). Right: Fluorescent intensity measurements. Background fluorescence was removed by measuring a blank sample. Labeled arrows show an enhancement factor from the unmixed sample. (Unmixed n=4, Mixed n=4, Finger End n=3)..... 149

Figure 4-6: The same location on the device was analyzed with four different techniques: scanning electron microscop (Top left) energy-dispersive X-ray analysis (Top right), light microscopy (Bottom left) and fluorescent microscopy (Bottom right). 150

Figure 5-1: Different configurations for enhancing QCM binding with AC electrokinetics. (a) Depicts a standard QCM made from a piece of quartz with circular gold electrodes on either side. (b) Shows the first prototype which consisted of an IDE built on a glass substrate and placed in close proximity to the QCM surface. (c) Consists of a QCM onto which a dielectric material (glass) was deposited. IDEs were then fabricated on the glass surface. (d) This is the final prototype and consists of a piece of quartz with an IDE on top and a circular electrode on bottom 172

Figure 5-2: Schematic of the techniques used to fabricated EKQCMs. The left side shows the lift-off technique while the right shows the wet etch technique..... 174

Figure 5-3: The fluorescent image analysis technique relies on measuring regions on the electrodes for intensity. ImageJ was used for this purpose and the left and right figures show measurement boxes for a parallel straight and castellated pattern respectively.	176
Figure 5-4: Images taken from sample 1	178
Figure 5-5: Images taken from sample 2 under the same conditions.....	179
Figure 5-6: Comparison of particle collection and fluorescent antibody binding.....	180
Figure 5-7: Relative binding capacity of a cleaned gold and glass surface	182
Figure 5-8: Scaling analysis of particle velocity separated by forces. Forces within the grey region are non-deterministic due to thermal randomization.....	184
Figure 5-9: Frequency dependence of ACEO and DEP according to Theoretical prediction (top) and experimental frequency dependence of antibody capture enhancement via fluorescent imaging analysis.	185
Figure 5-10: Spatial distribution of deposited IgG. Top: Simulated surface concentration as a function of position on an electrode surface. Bottom: Image of accumulated IgG on the surface of interdigitated electrodes under the presence of AC Electrokinetics.	187
Figure 5-11: Comparison of a simulated gradient of electric field squared with fluorescent imaging of IgG on a castellated electrode that was incubated in the presence of AC electrokinetic forces.	188
Figure 5-12: Image of electrode damage due to 10 mV DC offset to 100 Hz, 1 V _{pp} AC signal..	189

ABSTRACT

Enhancement of Protein Binding on Immunosensors Using AC Electrokinetics

Robert Weisbein Hart

Hongseok (Moses) Noh, Ph. D. & Ryszard M. Lec, Ph.D

The goal of this research was to investigate AC Electrokinetic forces with the purpose of using them to improve protein binding onto the surfaces of biosensors. Biomolecules typically diffuse slowly and react quickly to biosensor surfaces. This leads to transport limitations of analyte to the transducer surface and results in long detection times. Microscale electrodes supplied with an AC field can generate forces, known as AC electrokinetics, that act on particles submerged within a liquid or that operates on the fluid itself. Using these phenomena, the transport limitations can be alleviated by advective mixing or by concentrating local particles. Though there are several important phenomena that contribute to the overall behavior of particles and fluids, current predictive techniques consider special conditions where only a single phenomenon may be considered. A finite element model was therefore developed to predict more general conditions where the various AC electrokinetic forces coexist and to understand how these forces affect protein binding onto a surface. The simulation predictions were corroborated with experimental observations of collected microparticles as well as fluorescent protein adsorption assays. Design and operational parameters that affect protein binding were investigated using these means. The simulations indicated that binding times can be reduced by up to a factor of 6. Fluorescent intensity of the protein assays indicated an enhancement of about 1.9 times at the center of the device and 6.7 times at the edges of the best device type. Finally, the development of a hybrid

sensor-actuator was constructed by fabricating interdigitated electrodes capable of generating AC Electrokinetics onto the surface of a quartz crystal microbalance. Directly adsorbed antibodies were bound to the surface of this new device using AC electrokinetics and the signal was consequently enhanced by a factor of about 5.6 for a 15 minute reaction. Modification of the QCM resulted in little reduction of quality factor and an increased sensitivity to viscosity changes. This research is expected to help translate biosensors and microfluidic devices that have applications in point-of-care diagnostics, environmental monitoring and counterterrorism.

CHAPTER 1: INTRODUCTION & BACKGROUND

1.1 Thesis Organization

1.1.1 Article-based Thesis

The structure of this document follows that of the article-based thesis. Following an introduction in this chapter (1) are three chapters (2, 3 and 4) which are organized as free-standing peer review journal articles. The final chapter (5) provides a conclusion to the thesis work. Chapter descriptions are described briefly in Figure 1-1 and in more detail in the following text.

Chapter 1: Introduction	<ul style="list-style-type: none"> • Motivation and Approach • Specific Aims • Background & Literature Review
Chapter 2: Analysis of AC Electrokinetic Forces	<ul style="list-style-type: none"> • Overview & Theory of AC Electrokinetics • Experimental: Microsphere Behaviors in a Microchannel • Modeling: FEM of Involved Forces
Chapter 3: Investigation of ACEO Effect on Immunoassays	<ul style="list-style-type: none"> • Overview & Theory of Transport-Limited Systems & AC Electroosmosis (ACEO) • Modeling: FEM of immunoassays in presence of ACEO • Experimental: Use of ACEO to Improve Fluorescent Immunoassay
Chapter 4: Application of ACEO to Novel Biosensor	<ul style="list-style-type: none"> • Overview & Theory of ACEO, transport-limited system and the QCM sensor • Modification of QCM With AC Electrokinetic Device • Experimental: Use of ACEO to Improve Biosensor Signal
Chapter 5: Conclusion & Future Work	<ul style="list-style-type: none"> • Overview of Work Towards Specific Aims • Contributions to the Scientific Community • Future Work

Figure 1-1: Thesis Structure & Function

(1) Chapter 1

Chapter 1 serves as an introduction to this thesis which includes the central motivation, problem statement and general approach. This is followed by the specific aims and a background and literature review. There are three specific aims, each of which is individually addressed with a subsequent chapter.

(2) Chapter 2

Chapter 2: “Comprehensive Analysis of Particle Motion in Non-Uniform AC Electric Fields in a Microchannel” covers Specific Aim 1. In this section, the theory behind the three different AC electrokinetic forces is discussed in detail. This is followed by an experimental section which describes the many different behaviors microparticles exhibit under the influence of AC electrokinetics. Next, the development and results of a novel finite element model, which was used to determine the forces acting on a submerged microparticle from AC electrokinetics, are described. The experimental conditions were replicated in the simulation and the results of both were used to explain the observed particle motion.

(3) Chapter 3

Chapter 3: “Enhancement of Heterogeneous Immunoassays Using AC Electroosmosis” covers Specific Aim 2. This chapter is focused on understanding how AC Electroosmosis can affect a heterogeneous immunoassay. The transport-rate limited nature of many immunoassays is described in the introduction to Chapter 3. Additionally, the proposed use of ACEO to reduce transport limitations is described here as well. This is followed by a simulation section and an experimental section. The simulation section describes the development of a finite element

simulation which was used to model a heterogeneous immunoassay in a microchannel under the influence of ACEO. The experimental section describes the use of ACEO to enhance fluorescent immunoassays on microfabricated devices capable of generate such forces. Both the simulation and fluorescent immunoassays were used to find efficient conditions under which the best enhancement of binding could be achieved.

(4) Chapter 4

Chapter 4: “Improved Protein Detection on an AC Electrokinetic Quartz Crystal Microbalance” covers Specific Aim 3. This chapter is focused on the development and testing of a novel sensor capable of performing dual mass sensing and AC electrokinetic actuation. The fabrication of this sensor is described, and tested both electrically and with liquid loading in order to ensure the sensor function was not significantly diminished. Finally, an experimental section is included which describes the fluorescent antibody binding experiments carried out on the novel sensor.

(5) Chapter 5

Chapter 5 concludes the main body of the thesis and consists of a conclusion broken down by Specific Aim. This is followed by a discussion of the advancement of scientific knowledge contributed by the work in this Thesis. Finally, some promising and relevant future work is discussed.

1.2 Motivation and Approach

Immunoassays are a mainstay of clinical research and diagnosis, counter bioterrorism and environmental monitoring [1-2]. In a wide variety of common conditions, the time it takes to detect an analyte with an immunoassay is inordinately long, often taking hours [1-3] because of the transport limited nature of the system. This can be a critical barrier to the creation of many types of biosensors which would require rapid detection of analyte on the order of minutes. The

primary focus of this dissertation is to investigate the possibility of using AC electrokinetics to improve the binding rate of these transport-limited systems by stirring the reaction volume. AC electrokinetics are a suite of phenomena that arise when high strength, non-uniform AC electric fields are generated within a fluid environment. This causes the motion of the fluids themselves as well as submerged particles which can move independently of the fluid.

Three main approaches were taken during this study (See Figure 1-2).

1. First, an investigation of AC electrokinetic forces was undertaken with the use of finite element modeling.
2. Second, the ability of AC electrokinetics to effectively enhance immunoassays was studied with the use of fluorescent immunoassays and microscopy.
3. Third, a test sensor was modified to incorporate AC electrokinetics and the device was used to quantitatively observe the effects of AC electrokinetics on protein adsorption.

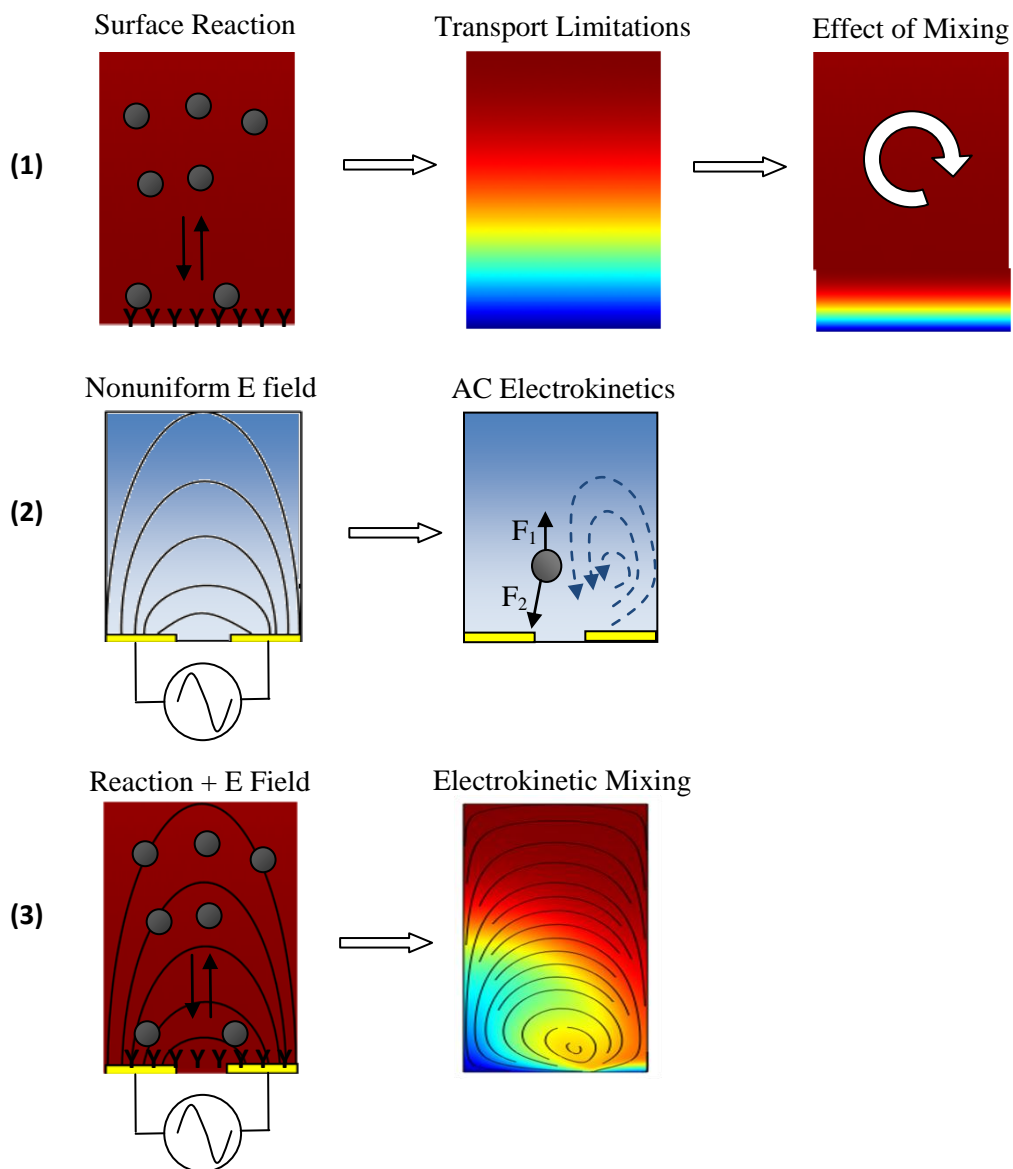


Figure 1-2: Thesis concept diagram. (1) Shows a typical transport rate-limited surface reaction. Receptors bound on a solid surface react with analyte in solution. Slow analyte diffusion, fast surface reaction and large diffusion distances cause inordinately long reaction times. Mixing the solution can help reduce transport limitations. (2) High strength non-uniform electric fields can

cause particle and fluid motion and is known as AC Electrokinetics. (3) The use of AC Electrokinetics to enhance transport rate-limited reactions by stirring the bulk solution and bringing fresh analyte to the surface for reaction.

The primary contributions of this thesis are focused within the broad fields of biosensors and microfluidics. These technologies both suffer from a general failure to meet industry expectations although they are valuable and common tools within academic research [4-5]. The realization of a versatile lab-on-a-chip system or otherwise portable and rapid biosensing platform for use in healthcare, environmental monitoring or biological weapon detection has not yet been realized despite active efforts of scientists and engineers as well as investment from entrepreneurs during the last several decades [6]. It is hoped that the results of this research will help to overcome two of the many technical barriers, slow detection time and insufficient detection limit, in a cost-effective way.

1.3 Specific Aims

1.3.1 Aim 1: Characterize AC electrokinetic forces in a microchannel

Although much attention has been paid to AC electrokinetics in the last few years, there was no comprehensive analysis of the major AC electrokinetics forces acting in concert prior to this thesis work. Efforts to study the forces generated by nonuniform AC electric fields in microchannels have focused mainly on single forces and neglected the effects of others. Furthermore, there was a scarcity of information pertaining to the effects of operational and system parameters on the strength and distribution of these forces.

The primary objectives of Aim 1 were (1) to gain an understanding of the interactions between the different AC electrokinetic forces, (2) to determine how the operational and system parameters affect the forces and (3) to develop a versatile model that could be applied to other problems, such as mixing.

The general approach to completing Aim 1 was to develop a finite element model of a microelectrode within a microfluidic chamber and include the effects of three major AC electrokinetic forces on the motion of small spherical particles. Simulation results were then compared to experimental observations of micro and nano-particles under a wide variety of conditions. The work towards accomplishing Aim 1 is described in CHAPTER 2:

COMPREHENSIVE ANALYSIS OF PARTICLE MOTION UNDER NON-UNIFORM AC ELECTRIC FIELDS IN A MICROCHANNEL

1.3.2 Aim 2: Evaluate the effect of AC electrokinetics on transport-limited heterogeneous immunoassays

A heterogeneous immunoassay is one where the immunological complexes are bound to a solid surface. These reactions generally suffer from mass transport limitations which can be somewhat alleviated by advective mixing. The hypothesis is that mixing can be accomplished through the use of AC electrokinetics – specifically with AC Electroosmosis.

The primary objectives of Aim 2 were (1) to determine under what conditions, if any, AC electroosmosis can aid the transport of protein to the assay surface and (2) to attempt to optimize these conditions.

The general approach to completing Aim 2 was to build upon the finite element model from Aim 1 to simulate a heterogeneous assay by accounting for convection, diffusion and a surface reaction. The understanding gained from these simulations was corroborated and bolstered by observations of fluorescent immunoassays performed under the influence of AC electroosmosis under a wide variety of conditions. The work towards accomplishing Aim 2 is described in CHAPTER 3: ENHANCEMENT OF HETEROGENEOUS IMMUNOASSAYS USING AC ELECTROOSMOSIS.

1.3.3 Aim 3: Quantify the effect of AC electrokinetics on a biosensor system

The use of AC electrokinetics to enhance protein detection on a biosensor has not yet been studied. (Two occurrences of enhanced particle (not protein) detection on biosensors have been reported so far [7-8]). Alleviating the transport limitations imposed by reaction chemistry with the

use of AC electrokinetics can help to reduce detection times and decrease the detection limit of a biosensor.

The primary objectives of Aim 3 were (1) to construct a biosensor equipped with the capability to perform AC electrokinetics, (2) to characterize the sensor performance after modification, (3) to measure protein binding under AC electrokinetic enhancement and (4) to corroborate sensor response with independent means.

The general approach to accomplishing Aim 3 was to modify a quartz crystal microbalance by fabricating microelectrodes, capable of generating AC electrokinetics, onto its surface.

Calibration of sensor function was carried out through electrical and experimental means.

Verification of sensor results was carried out with fluorescent imaging and protein quantification assays. The work towards accomplishing Aim 3 is described in CHAPTER 4: IMPROVED PROTEIN DETECTION ON AN AC ELECTROKINETIC QUARTZ CRYSTAL MICROBALANCE.

1.4 Background & Literature Review

1.4.1 The transport-limited system – a major source of long detection times in biosensor systems

When biological receptors are placed on a solid support and reacted with biomolecules in a contacting solution, the system is generally transport rate-limited. These limitations occur because the reaction rate constants can be very high ($10^8 \text{ M}^{-1}\text{s}^{-1}$ for antibody-antigen reaction) [9], the distances large (hundreds of microns to millimeters) and the diffusion rates of biological molecules is also large (10^{-11} to $10^{-10} \text{ m}^2 \text{ s}^{-1}$ which can be found using the Einstein-stokes equation). The end result is that reactants close to the active surface are quickly bound (or used

up) and a diffusion gradient is formed such that the concentration near the reactive surface is much lower than in the bulk solution. In cases devoid of fluid convection, the transport of reactants to the surface is solely dependent on diffusion. The supply of fresh reactants therefore arrives slowly with respect to the reaction rate. A useful way to represent whether a reaction is transport-limited or reaction-rate limited is with a dimensionless number known as the Damköhler number (Da). This is a ratio of the reaction velocity ($k_{\text{ads}}\theta_0$) to the rate of transport (D/h) where k_{ads} is the forward rate constant, θ_0 is the number of receptor sites, D is the diffusion coefficient and h is the characteristic length scale – for example a reaction chamber height. $Da \gg 1$ indicates a transport limited system while $Da \ll 1$ indicates a reaction-rate limited system. Even in microchannels where the diffusion distance is not great (typically 100 μm or less), the Da of immunoassays can be on the order of 100 or higher [10]

These transport limitations in a biological setting have been extensively studied [11-13] and many researchers have applied these theories to detection of analyte using biosensors – usually with the optical BIACORE system [12, 14-15] which uses the principle of surface plasmon resonance.

When transport limitations occur, a popular solution is to apply flow to the system, but this requires pumping equipment and much more reagent, which may be expensive or in short supply. If the reaction volume is large enough (for example, in a 96-well microtiter plate) advective mixing may be used.

In smaller systems, such as microfluidic devices, where characteristic length scales are on the order of 100 μm or less, turbulent mixing is not possible due to the extremely low Reynolds numbers.

1.4.2 Background on antibodies – the essential component in immunoassays

Immunoassays rely on the specificity and sensitivity of the antibody-antigen reaction to detect the presence of an analyte. Antibodies are blood proteins of vertebrates that are part of the immune response to foreign agents. They are produced, and released into the blood by plasma B cells which have become activated after internalizing an antigen (the foreign agent). There are many different species of antibodies, but the most common is the Immunoglobulin G (IgG). Others include IgM, IgA, IgD and IgE. Both IgG and IgA have several subclasses as well [16]. The molecular weight of IgG is about 150 kDa and the diffusion coefficient is around $10^{-11} \text{ m}^2 \text{ s}^{-1}$ [10]. The antibody-antigen reaction is very strong, with a K_a (forward rate constant) of around 10^{12} - 10^{14} [17].

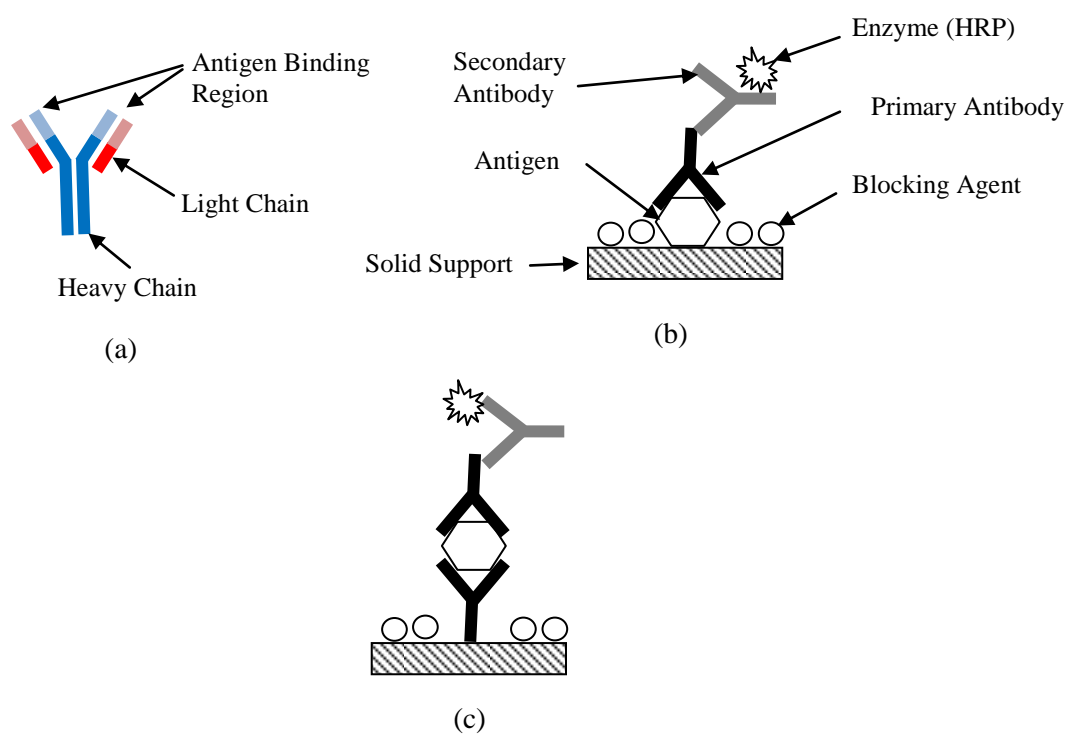


Figure 1-3: Antibody structure and ELISA. (a) Shows the structure of an Immunoglobulin G. (b) shows a typical Indirect ELISA and (c) shows a Sandwich ELISA. Other types include Competitive ELISA and Reverse ELISA

The first immunoassays were performed using radioactively labeled antibodies and were known as radioactive immunoassays (RIA) [18]. Though the sensitivity is slightly less, they have been largely replaced with fluorescent immunoassays (FIA) which are non-hazardous and less expensive. The most widely used immunoassay is the enzyme-linked immunosorbent assay (ELISA) [19] (PubMed search term: 'immunoassay' returns ~360,000 hits and 'ELISA' returns ~150,000 hits).

1.4.3 Enzyme Linked Immunosorbent Assay (ELISA) – the current gold standard

An ELISA is a heterogeneous immunoassay (where a reaction takes place at the interface between two phases, for example, a solid and liquid) and consists of selectively binding an analyte to a surface followed by subsequent reactions from immunological counterparts contained within a liquid phase. The enzyme, usually horse radish peroxidase (HRP), which is linked to one of the bound antibodies, reacts with substrate molecules (as in an enzyme-substrate interaction) contained within the final solution. This reaction is what generates the measurable signal, which can be colorimetric, fluorescent or other quantifiable change. ELISAs come in several varieties – the Indirect ELISA, the Sandwich ELISA, the Competitive ELISAs and the Reverse ELISAs. The first two are the most common and are shown in Figure 1-3. The indirect ELISA binds a known quantity of antigen to a solid surface (for example, a microwell plate) followed by a blocking step, which is used to prevent any non-specific binding of subsequent proteins. This prepared surface is then reacted with an unknown quantity of antibodies, the

measurand. After washing away unbound antibodies a solution of enzyme-linked antibodies (known as secondary antibodies) is reacted with the surface. These secondary antibodies are selectively bound to the measurand antibodies and cause the signal to appear in the solution, which is proportional to the quantity of labeled measurand.

1.4.4 Fluorescent Immunoassays

Though much less sensitive, a heterogeneous fluorescent immunoassay can be completed in much the same way as an ELISA. In this case, an enzyme-linked secondary antibody is replaced with a fluorescently labeled secondary antibody. Measurement can be made using a fluorescent microscope. There are two main advantages to the fluorescent immunoassay described here compared to a traditional colorimetric ELISA as it pertains to this dissertation work. First, it may be carried out on opaque surfaces. Colorimetric assays by comparison, must be performed on clear surfaces so that absorbance measurements may be made through the liquid and solid support. Second, ELISAs release signal-causing agents into the contacting fluid, while fluorescently labeled antibodies are surface-bound. This means that information about antibody location on the surface, for example, local regions of high concentration, can be ascertained. In other words, the ability to concentrate proteins to a specific region on a substrate cannot be learned from an ELISA which integrates signals originating from across the surface.

1.4.5 Background on Florescein, the fluorophore used

The fluorophore used throughout this research was fluorescein. With a high fluorescence, fluorescein-labeled antibodies are commercially available and inexpensive. Fluorescein has a peak absorbance at 494 nm and a peak emission of 521 nm (in water). Though fluorescein has many benefits, it suffers from photobleaching (exposure to light degrades the signal). This makes quantitative measurements difficult. Using a fluorescent microscope, quantitative measurements

may be made inaccurate by the variability introduced during the time it takes to focus, translate to a specific location and obtain a photomicrograph. Throughout this time, sample signal is reduced. To alleviate these problems, the following technique can be used:

- Focus on a region that will not be imaged.
- Quickly move to the region of interest and close the microscope shutter (this blocks the light and prevents photobleaching).
- Open the shutter and immediately take an image on the microscope computer software.
- Background fluorescence is also present in many sample types – glass, for example. To eliminate this effect, a blank sample should be imaged and the fluorescent intensity should be subtracted from the unknown samples.

1.4.6 Microfluidics history and background

Microfluidics is the science and technology of accurately manipulating and controlling tiny volumes of liquid, ranging from a few microliters to volumes as low as femtoliters. The advantages of microfluidics can include portability, performance enhancement, disposability, cost effectiveness, small sample requirements and the ability to more closely mimic biological systems on the cellular level. Typically the fabrication process involves steps similar to those developed to manufacture integrated circuits on silicon wafers – namely photolithography, deposition and etching. Microfluidic devices are now made on a variety of additional materials including glass, metals and polymers. One of the central goals of microfluidics is to develop analytical systems that perform, in one device, a complete analysis of a sample, including sample handling, preconcentration, reaction & incubation steps, separation, and measurement. These systems are known as Lab-on-a-chips, microTAS (total analytical systems) or biochips.

The field of microfluidics began in the early 1950s when ink-jet technology was being developed to dispense nano- and pico-liter drops of liquid [20]. It was not till over two decades later, in 1979 when the first analytical microfluidics device was produced. This was the landmark gas chromatographic air analyzer fabricated on a silicon wafer by Terry et al [21]. This was soon followed by micro-valves, and micro-pumps [20]. Today even though microfluidics has not yet reached maturity, it is a rich area of research and is the focus of several worldwide academic conferences (MEMS, Transducers, microTAS).

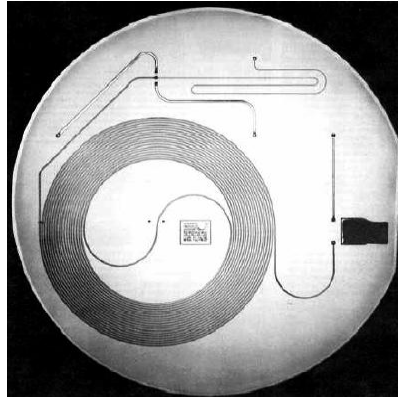


Figure 1-4: Image of a spiral capillary etched into 2 inch dia silicon wafer to serve as a gas chromatography column made in a landmark work by Terry et al.

However, microfluidics has, in many ways, failed to meet the expectations of scientists, engineers and technology investors who attempted to commercialize this technology in the 1990s. It is speculated that the technological ‘toolbox’ was, and is, perhaps, still not complete and that attempts to commercialize were premature [6]. Today, there is a scarcity of commercialized microfluidic devices, though recently, a new wave of more cautious investment is underway.

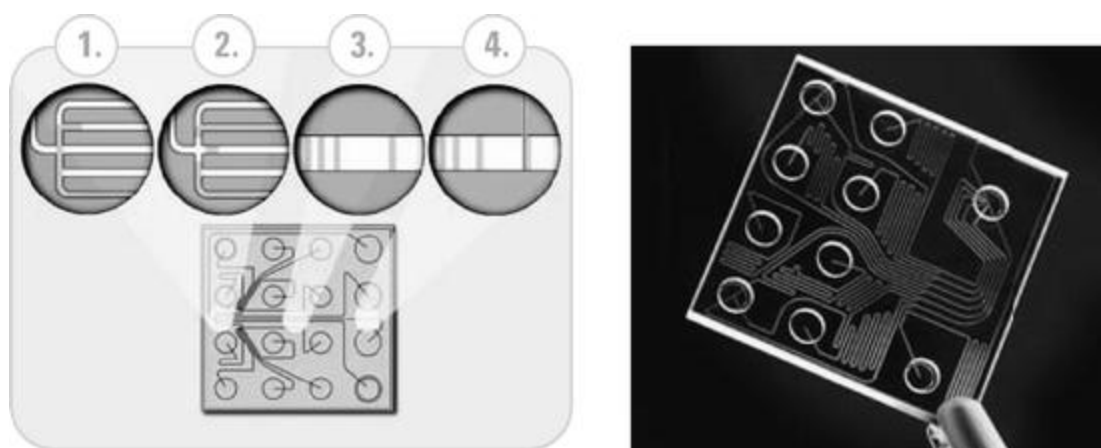


Figure 1-5: An electrokinetically-driven capillary electrophoresis chip developed by Agilent.

One of the goals of this thesis is to contribute an important tool to the growing microfluidic toolbox. By helping analytical detection occur faster or with greater sensitivity, at least one part of the total analytical system may be improved to the extent that it is no longer the limiting feature.

1.4.7 AC Electrokinetics background

AC electrokinetics is the movement of fluids and particles using AC electric fields. In general, the electric fields must have non-uniform components to them, since a uniform AC electric field will elicit no time-averaged movement. For example, a charged particle suspended in a solution between two infinitely wide parallel plates will move towards one plate due to Columbic forces if a potential is applied, and towards the alternate plate if the potential is switched. An AC signal will average zero net movement because the field is uniform (Figure 1-6(a)). If one of the plates is replaced with a pin electrode, for example, the electric field becomes non-uniform (Figure

1-6(b)), and the strong gradients that exist near the pin electrode can cause even particles to move regardless of their charge or dipole moment. This movement is caused by AC electrokinetics.

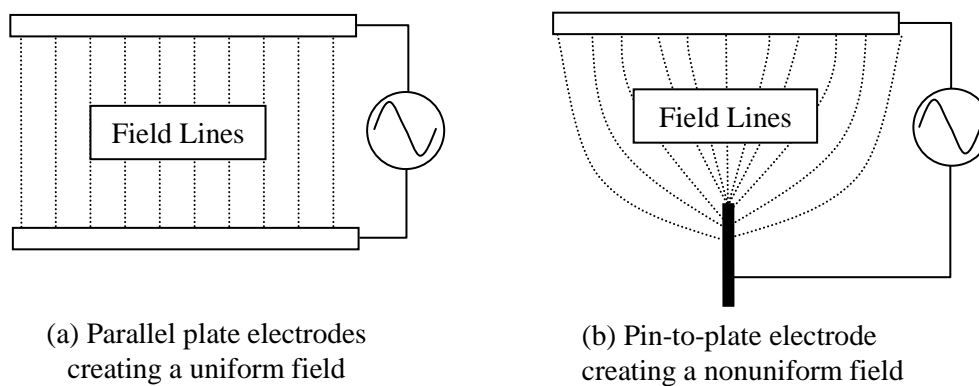


Figure 1-6: Diagram of a (a) uniform and (b) nonuniform electric field.

A brief primer on AC electrokinetics will be described in this section with more detailed explanations found in section 2.3 on page 52.

(1) *AC Electroosmosis*

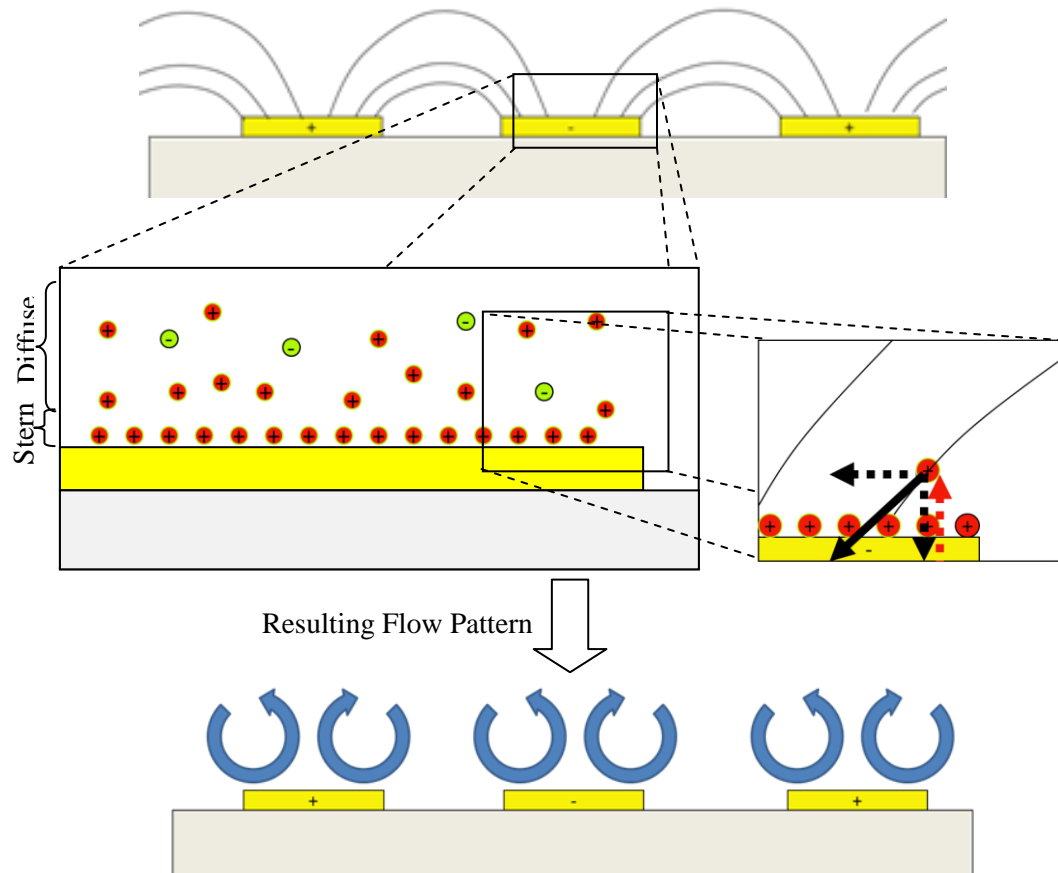


Figure 1-7: Charge movement at the electrode surface resulting in ACEO flow patterns.

When a potential is placed on a submerged electrode an electric double layer is established (Figure 1-7). AC Electroosmosis (ACEO) arises due to the movement of free charges within the diffuse double layer. In a set of interdigitated electrodes, these charges move from the edges of the electrode towards the center. The bulk movement of these charges induces fluid flow due to viscous drag effects.

ACEO can only exist in low conductivity media such as DI water. High conductivity media such as buffer results in a tightly bound and immovable electric double layer. ACEO is also highly dependent on frequency and voltage of the applied electrical signal. A frequency range of 0.1 kHz to 5 kHz usually results in the strongest ACEO velocity, although the peak velocity depends, to an extent on solution conductivity. ACEO velocity is also proportional to the square of the applied voltage. Doubling the voltage results in a quadrupling of the ACEO velocity.

(2) *Dielectrophoresis*

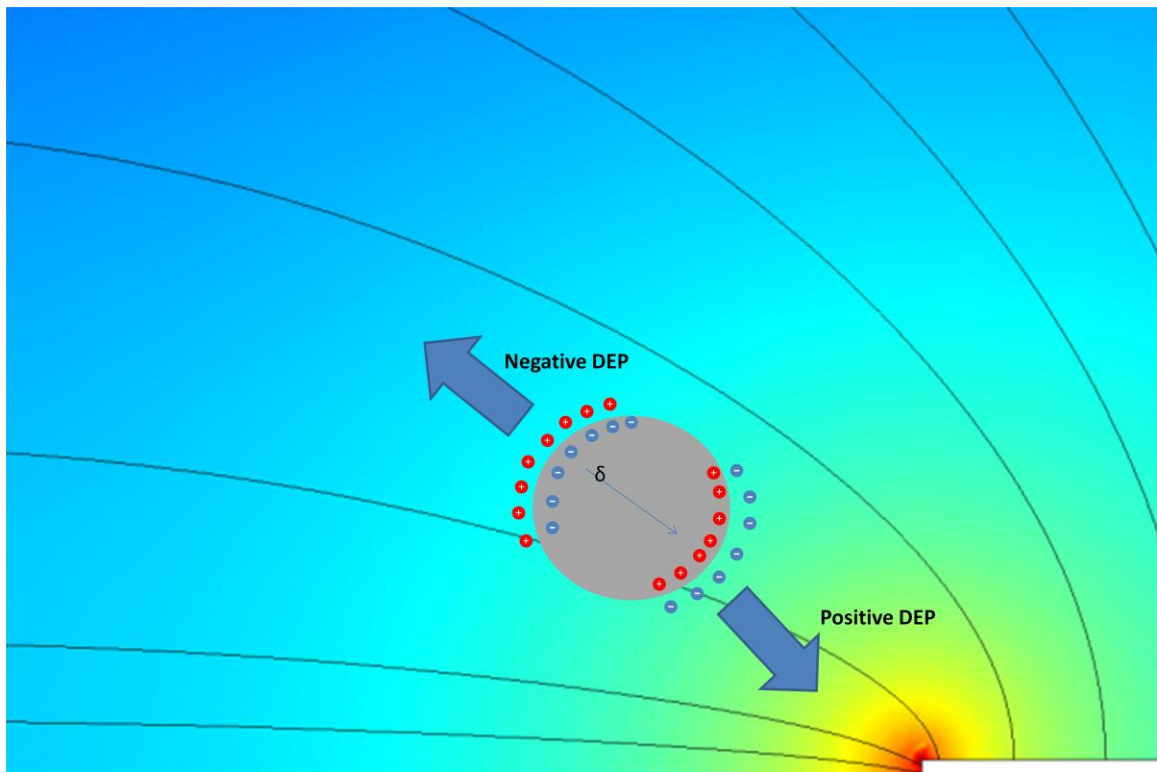


Figure 1-8: Dielectrophoresis causes particles to be attracted to or repulsed from high electric field strength. Negative DEP is when the particle is repulsed and positive DEP is when the particle is attracted to high electric fields.

Dielectrophoresis was introduced by Pohl et al [22-23] in the 1950s. He discovered that in the presence of highly divergent electric fields, colloidal particles would move in a fashion similar to that of electrophoresis. Unlike electrophoresis, however, the direction of travel did not reverse with a reversal in potential. Further, field strengths required to move particles with DEP, were much higher, and coarse suspensions were required (2 μm particles). Pohl used extremely high voltages (10 to 100 kV) in order to achieve DEP effects. Currently, the use of microfabrication allows researchers to develop sharp, closely spaced electrodes that exhibit the same or greater field strengths than Pohl and can achieve much better precision and manipulation of smaller particles – even DNA molecules have been accurately controlled with DEP [24-25].

An electric field will cause a particle with a dipole (induced or permanent) to become oriented. In a nonuniform electric field, one side of the particle will be in a higher field strength than the other. This results in a net force in the direction of greater field intensity. Reversal of the field results in the same motion as before, hence, unidirectional motion occurs in DC or AC fields.

This is an example of positive DEP and does not consider the ability of the surrounding fluid to become polarized as well. If the fluid is more polarizable than the particle, the stronger force will be for the fluid to move to the region of high field strength. This forces the particle away from high field regions in an effect known as negative DEP. Polarizability depends on many factors - most notably the frequency of the applied field. It is well known that solid microspheres are more polarizable than DI water at low frequencies but this relationship reverses at higher frequencies. This characteristic allows for many interesting particle behaviors which are frequency dependent.

(3) *Electrothermal Effect*

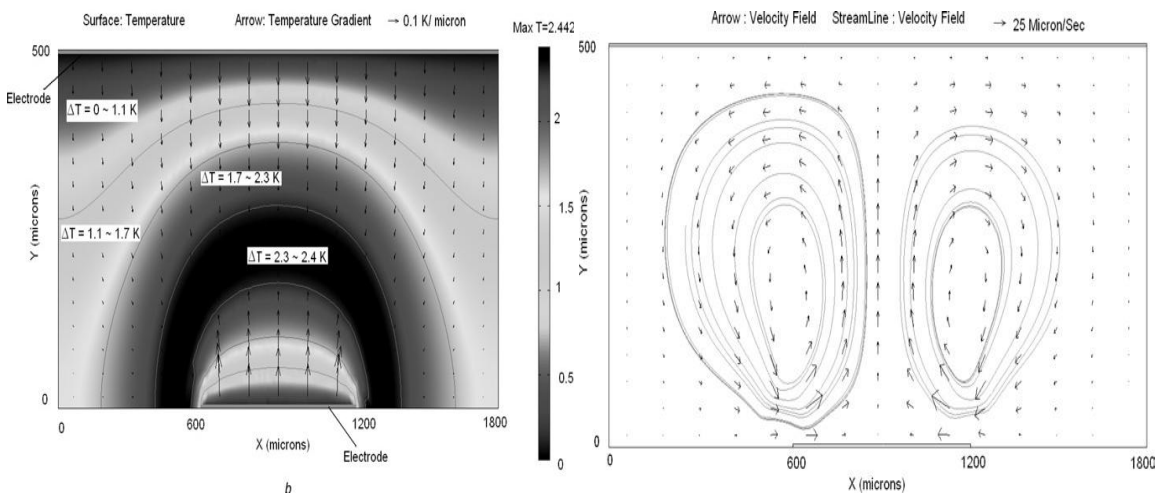


Figure 1-9: Electrothermal effect. Left: thermal gradients formed by Joule heating. Right: resulting fluid flow [26].

When an electric field is passed through a liquid, some of the energy is lost to Joule heating. As the temperature of the water changes, so too do the electrical properties of water (which are dependent on temperature). In particular, permittivity and conductivity both change as a result of Joule heating. In micro-scale volumes, surface effects are very strong due to the high surface-to-volume ratio. Electrodes, which are normally made of metal, serve as heat sinks. This, together with the non-uniform electric field, causes there to be strong temperature gradients. Gradients in temperature cause gradients in electrical properties of water, which generate free charges. These charges are moved by the electric field and, like in the case of ACEO, the movement of the charges induces fluid flow through viscous interaction.

Electrothermal effect is usually used for higher conductivity media because the decreased fluid impedance causes more of the energy to go through the liquid, causing stronger Joule heating effects. The electrothermal effect requires higher field strengths than ACEO to generate useful flow velocities. However, velocity increases much more dramatically with an increase in voltage. The relationship is a fourth power one, so that doubling the voltage results in a 16 times increase in fluid velocity.

(4) AC Electrokinetic devices

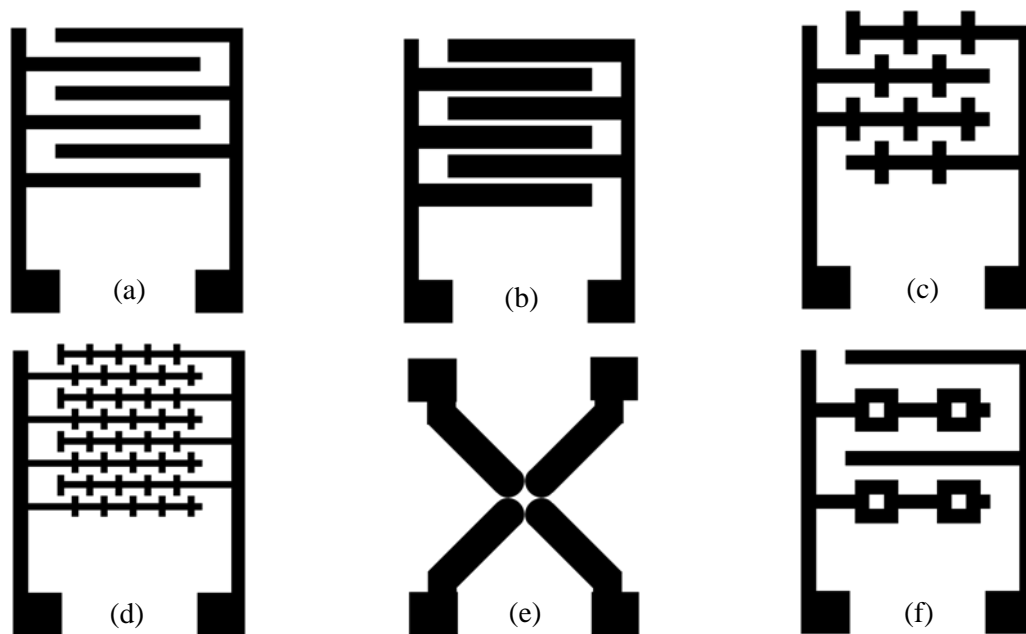


Figure 1-10: Several popular AC electrokinetic device patterns. (a) A set of parallel straight electrodes where the electrode width is half of the pitch distance. (b) shows a similar device where the pitch is the same but the electrode is wider. (b) and (c) show different size castellated

electrodes. (e) Shows a quadropole electrode (adjacent electrodes are 180° out of phase). (f) shows a potential-well pattern.

AC electrokinetic devices used in microfluidics typically consist of planar interdigitated electrodes of various designs and scale. Several of these designs are shown in Figure 1-10. Other designs, consisting of top and bottom electrodes (where one of the electrodes is on the top of the channel and the other is on the bottom) have also been considered [27-28] and 3D electrode designs. Other designs consist of 3D electrodes with an appreciable height compared to the channel – often where electrode pairs will have asymmetrical heights [29-30]. There are many other designs in the literature each with a specific purpose, whether to trap cells, perform particle separation, manipulate droplets of fluid etc...

Using simple planar electrodes allows for easy fabrication (described in APPENDIX II) and a direct means of creating high strength nonuniform electric fields. A simple function generator operating with low voltages ($1-10 V_{pp}$) can be sufficient to drive these devices. Many of the devices shown in Figure 1-10 were tested under various conditions and detailed in Section 2.4 on page 61.

1.4.8 Alternative Mixing Techniques

One of the fundamental processing steps for processing biological or chemical samples is the mixing of two different solutions to make a homogeneous result. For larger sample sizes (length scales greater than 1 mm) and faster flows, Reynolds numbers are large enough to allow turbulent flow, which greatly enhances mixing. For microfluidic devices, the Reynolds numbers are generally much lower (<100) and the laminar nature of the fluid flows means that mixing is accomplished only by molecular diffusion. A simple microfluidic device which combines two

different solutions at a y-intersection with no other features might require several centimeters length in order to become completely mixed. For high throughput processes this can become a rate-limiting step. A large body of research exists, therefore, for the improvement of this process. This research can be divided up into two categories – passive micromixers, which require no external energy other than the mechanism for driving the fluid, and active micromixers, which utilize alternative sources of energy (eg. Electric fields, piezoelectric transducers, etc...).

Most of this work, however, is not relevant to the improvement of heterogeneous immunoassays (or other assays). The typical objective of most mixing research is to start with two different streams of liquid and combine the two to make a single homogeneous mixture within a short distance. Immunoassays, however, start with a homogeneous liquid containing an analyte and, in the course of removing this analyte, create concentration gradients near the reactive surface. The goal here is to alleviate these concentration gradients by stirring, which would greatly improve assay kinetics. As such, many of the reported designs for both passive and active mixing techniques cannot be used for reducing the mass-transport limitations of surface-based reactions. (For background on mixing streams of liquids into a single stream excellent reviews have been written by Chang *et al* and Hessel *et al* [31-32].)

Alleviating the reactant shortage at the functionalized surface of a microchannel or device requires active localized stirring. Not all of the technologies included in this overview were used to enhance heterogeneous assays but instead were used to mix streams of fluids. However, they were still relevant and may be applied as assay improvement techniques. There are four main categories: (1) electrokinetic, (2) acoustic, (3) magnetic, and (4) miscellaneous.

(1) Electrokinetic Mixing

Electrokinetic: Electrokinetic mixers can be further broken down by the specific forces employed

- DC electroosmosis (DC EO), electrothermal effect (ETE) and dielectrophoresis (DEP).

DC EO: DC EO is typically used to induce fluid flow within a microchannel and takes advantage of the large surface to volume ratio which typifies the microfluidic regime. Electrodes are placed at either end of a channel and a DC electric field is created along the length of the channel. This field induces the movement of free charges within in the electric double layer on the surface of the channel. These charges, in turn, cause bulk movement of fluid within the channel due to viscous interaction.

Recently, some authors have introduced a method of mixing using EO flows that ran transverse to the microchannel [33-34]. In this setup, electrodes run along the length of the channel and are separated by a gap (Figure 1-11). Transverse flows are caused by applying a potential across the channel. Although these papers discuss the application of this technology towards mixing two streams of liquids, EO flows could potentially be used to stir a heterogeneous assay. The velocity across the surface was reported to be on the order of 1 mm/s which would be sufficient for stirring. Unfortunately, due to the DC nature of the electric field, electrolysis of water occurred. In order to use DC EO, sufficient axial flow must be induced to remove the bubbles.

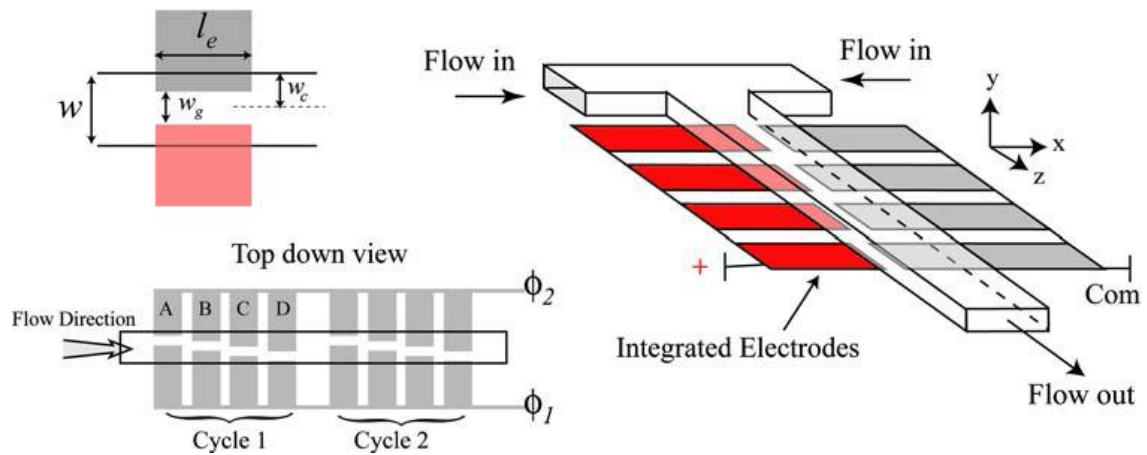


Figure 1-11: Schematic of the micromixing device used by Lynn *et al.* [33]

DEP: Unlike the other electrokinetic phenomena, DEP is not usually a hydrodynamic force but acts on particles suspended within the fluid. Yi-Kuen[35] and Deval [36] have used DEP as a means of mixing two streams of fluids by applying time varying fields to suspended particles within the streams of fluids. The channel design includes square recesses equipped with electrodes (Figure 1-12). This design utilizes the frequency dependence of DEP – lower frequencies cause particles to be attracted to the electrodes (positive DEP) while a higher frequency causes electrodes to be repelled (negative DEP). In Deval’s method, electrodes first use positive DEP to pull the particles into the recesses and then switch to negative DEP to eject the particles back into the channels. The chaotic movement of particles caused the fluids to mix by introducing folds and stretching into the streams.

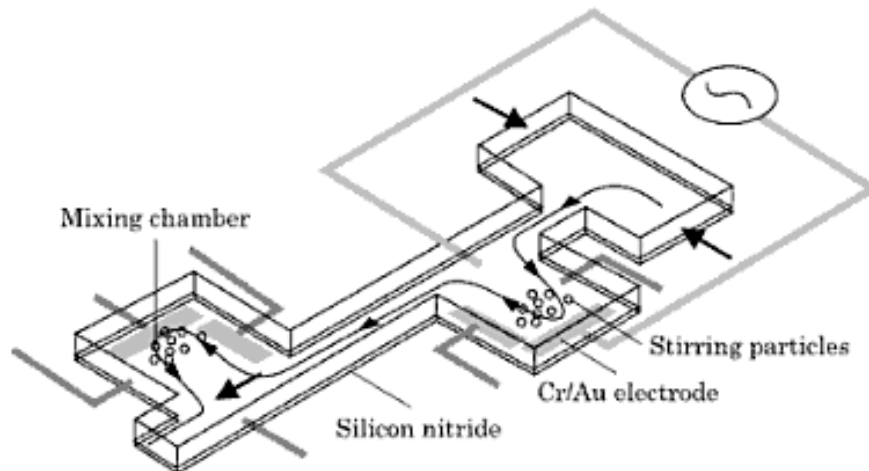


Figure 1-12: Device design for a chaotic DEP micromixer [36].

ETE: ETE causes fluid motion due to the interaction of the electric field with free charges within a fluid. The phenomenon has its roots in a temperature change in the fluid caused by the Joule heating effect of current passing through the liquid. Strong temperature gradients are formed within the liquid. Since the electrical properties (specifically conductivity and permittivity) of water are temperature dependant, gradients of these properties form within the liquid generating free charges. The movement of these charges within the electrical field causes rotational velocity patterns to occur near the electrodes. Meinhart's group et al was the first to suggest and use ETE to enhance heterogeneous immunoassays[37-38]. The mixing velocities were about $22 \mu\text{m/s}$, which was about 50 times less than predicted by numerical simulations. However, the fluid velocity obeyed a fourth power dependence on voltage. They report almost an order of magnitude improvement in bound material for a 5 minute assay. Later simulations carried out by

Huang et al using a C-reactive protein (CRP) – IgG binding reaction predict an enhancement factor of about 4-5 for binding rate using an optimally positioned electrode pair [27]. Although ETE requires relatively high voltages ($\sim 10 V_{\text{rms}}$) it can operate in high conductivity (and therefore physiologically relevant) fluids. Temperature changes are quite small and amount to only a few degrees Celsius.

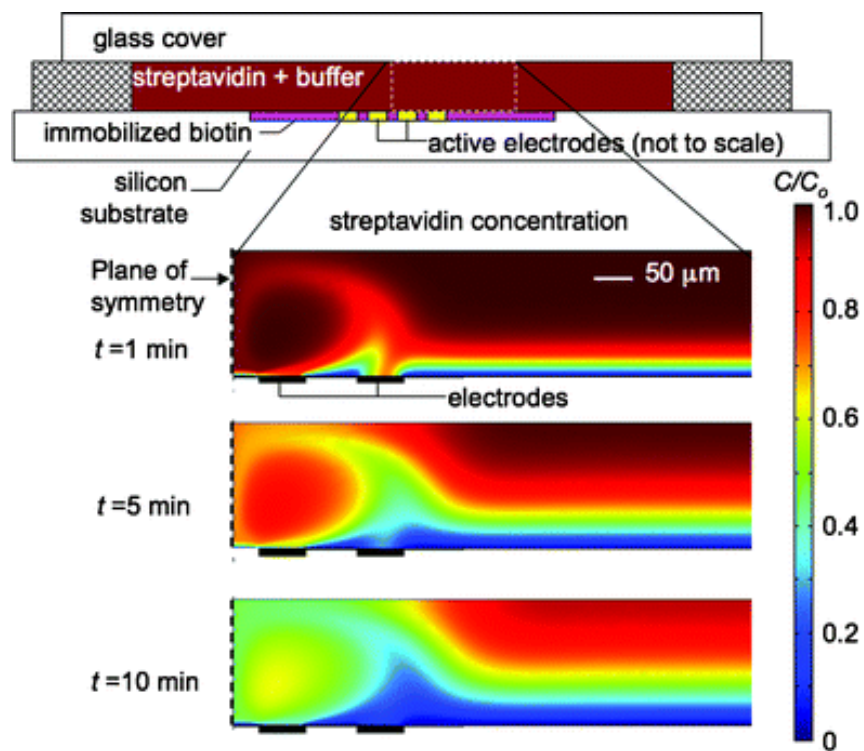


Figure 1-13: Device design and simulation for Fiedman *et al.* Numerical simulations show the relative concentration of streptavidin within the channels. [38]

(2) Acoustic Mixers

There are three main types of acoustic mixers – Bulk acoustic wave mixers (BAW), surface acoustic wave (SAW) mixers and bubble mixers.

BAW mixers: One of the first acoustic-wave micromixers was developed by Vivek *et al* (later used by Hongyu *et al*) who used a fresnel annular sector actuator (FASA) shown in Figure 1-14(a)[39-40]. In general, acoustic devices rely on acoustic streaming – the generation of unidirectional fluid flow due to the absorption of acoustic waves. The FASA device consists of a piece of piezoelectric material, usually lead zirconate titanate (PZT) sandwiched between a set of interdigital electrodes. The concentric fingers of these electrodes are spaced at multiple integers of the resonance wavelength so that the generated waves constructively interfere and are focused at the tip. So far, the FASA devices are relatively large by microfluidic standards, being about 7 mm in the case of Vivek *et al* and 10 mm for Hongyu *et al*. However, they can generate fluid velocities that are quite large by microfluidic standards even reaching 12 cm/s for a linear array of FASA devices (Figure 1-14(b)). For mixing applications, the transducers may be placed in a ring such as the one shown in Figure 1-14(c). The devices do not necessarily have to be placed in direct contact with the fluid but may be coupled to a channel wall.

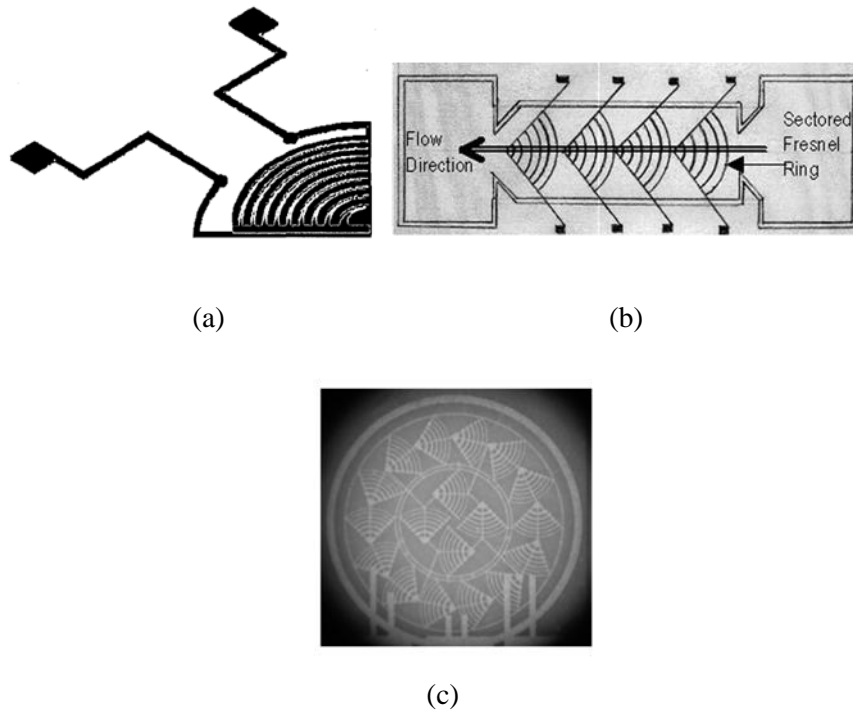


Figure 1-14: (a) Fresnel annular sector actuator (FASA) transducer[39]. (b) Linear array of FASA transducers to generate bulk channel flow [40]. (c) Rotational array of FASA devices for vortex generation. [40]

Another type of BAW mixer introduced by Jang *et al* uses a single circular diaphragm made from of PZT and varies the applied frequency in a so called ‘mode-hopping’ technique.[41] As the frequency of the applied signal increases, different modes of vibration appear and increase in complexity the higher the frequency. If the diaphragm is coupled to a circular microfluidic reaction chamber, acoustic streaming will cause the fluid to mix (

Figure 1-15). Mixing efficiency increases when cycling between two different modes (

Figure 1-15(c)). Jang *et al* showed that for a 6 mm diameter and 30 μm deep chamber, almost complete mixing occurred within 30 seconds.

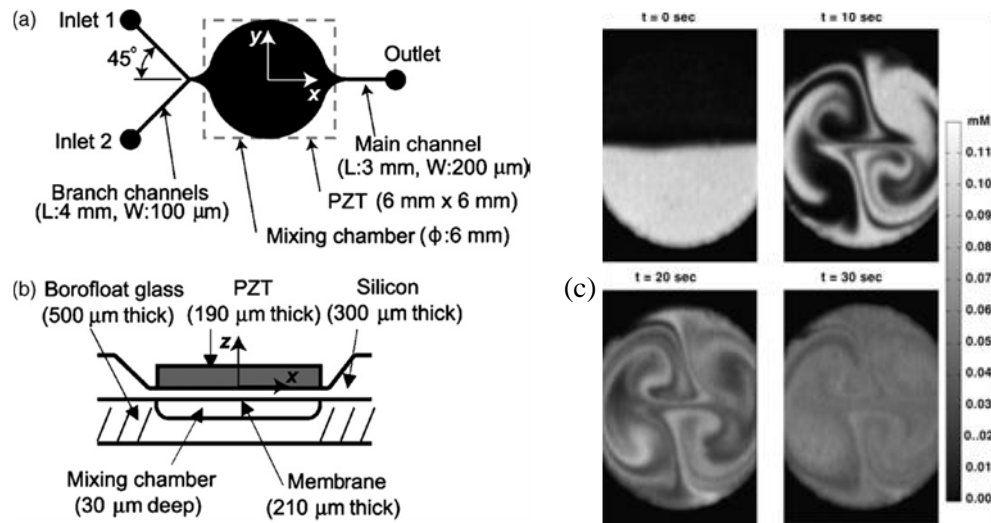


Figure 1-15: Resonant mode hopping device. (a) & (b) show the channel geometry and cross-section respectively. (c) shows top-down images mixing two streams. Mode hopping was employed at two different frequencies for 5s each. [41]

SAW micromixer: Like BAW devices, SAW devices rely on acoustic streaming to induce fluid flow and mixing. SAW waves, however, attenuate rapidly in liquid and causes smaller fluid velocities than BAW devices. Streaming velocities of up to 1 cm/s can be achieved using these devices. Actuation of the SAW device can cause jets of liquid to leave the surface of a channel at a particular angle as shown in Figure 1-16 (a). Placing the SAW device at the start of a channel causes fluid vortices to appear along the channel which dramatically improves mixing. Sritharan

et al applied this technique using a steady flow rate of $250 \mu\text{m/s}$ in a $75 \mu\text{m}$ by $100 \mu\text{m}$ channel and introducing $1 \mu\text{m}$ polystyrene microspheres into inlet of a Y-channel Figure 1-16 (b)).[42] Almost complete mixing occurred at 2.5 mm from the IDT (Figure 1-16 (c)), whereas without actuation of the IDT, the particles were not completely dispersed after 25 mm .

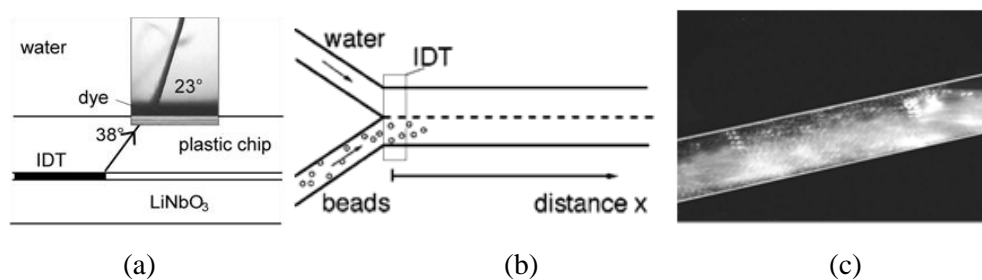


Figure 1-16: SAW mixer from Sritharan *et al.* (a) A schematic and image of acoustic streaming. LiNbO_3 with an IDT is coupled to a plastic chip which contains a microchannel. Quick and short actuation of the IDT causes a jet of dye to enter into the water layer. (b) A design using the SAW device to mix two streams in a simple Y-channel. (c) An image of distributed particles that have been mixed by the SAW device. The image was 2.5 mm downstream from the IDT. Without IDT actuation, mixing was incomplete even at 25 mm downstream. [42]

Bubble mixers: Bubble-induced acoustic micromixing was introduced by Liu *et al.*[43-45] The

devices consist of a piezoelectric disk attached to a microchamber. When the transducer is

actuated, trapped bubbles of a well defined size within the microchamber resonate and cause fluid

motion (

Figure 1-17 (a & b)). The fluid motion is rotational in nature and can reach speeds up to ~5 mm/s. Liu *et al* showed complete mixing within a large microfluidic chamber (12 x 15 x 0.125 mm) made of machined polycarbonate after less than 2 minutes (compared to 6 hours with no mixing). This device had an array of 2 mm pockets housing air bubble actuators. Using this same device, the authors were able to improve the capture efficiency of bacteria [45] on immobilized antibodies within the chamber. Capture efficiencies employing mixing were near 90% compared to about 2% without mixing. DNA hybridization assays also showed marked improvement with a similar device[43].

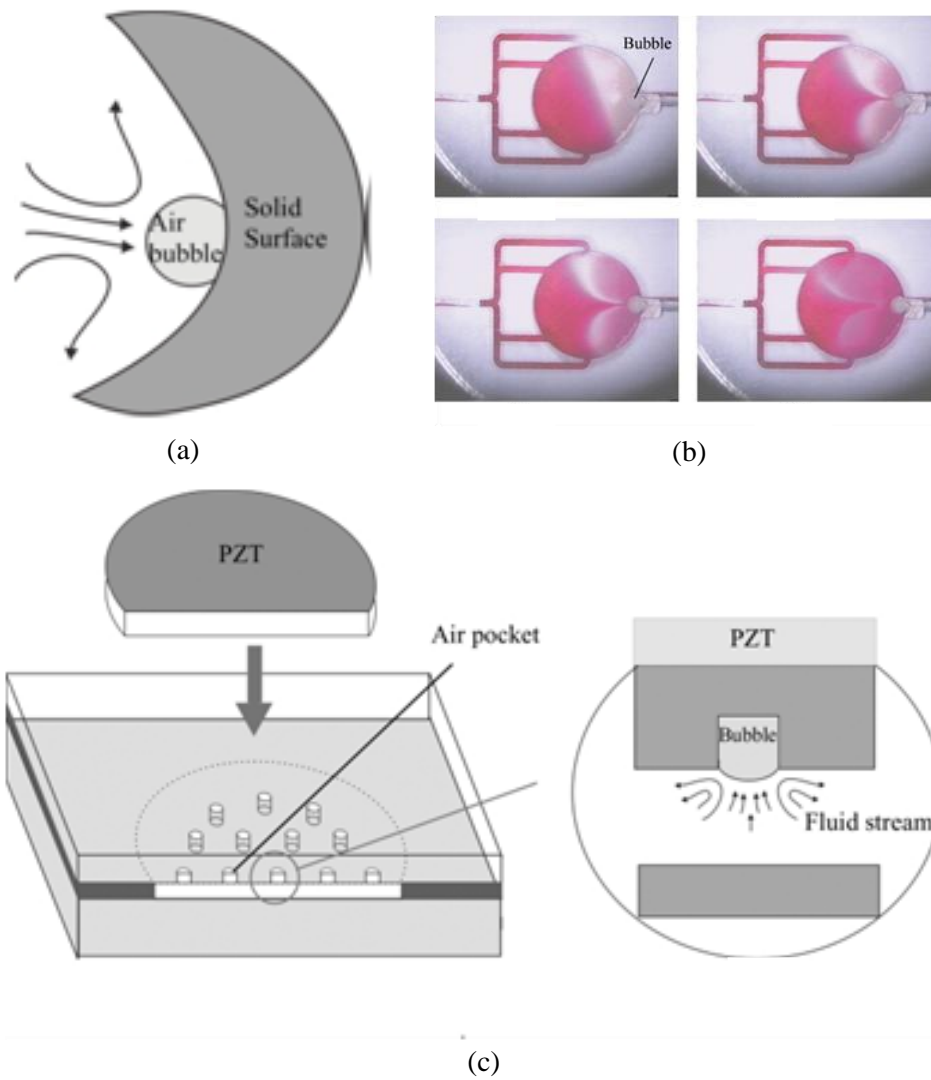


Figure 1-17: (a) Conceptual diagram of a bubble actuator. (b) Images of red dye being mixed by a bubble actuator. (c) A schematic showing an array of air pockets within a chamber. [45]

(3) *Magnetic Mixers*

There are two types of magnetic mixers found in the literature. The first type uses magnetic fields to act on magnetic beads suspended within a fluid. The second type uses magnetic fields to drive a mechanical stir-bar.

Magnetic Beads: Magnetic particles are commonly used in conventional biological assays. Receptors may be bound to the magnetic beads and allowed to capture ligands within the solution. Once the reaction has taken place the magnetic beads can be concentrated onto a surface for washing or measurement. Suzuki *et al* [46] describes a design for a chaotic micro-mixer that uses electrodes to generate a magnetic field which acts on suspended magnetic particles. They found the best arrangement was for the electrodes to be placed perpendicular to the general flow direction (Figure 1-18 (a)). In this way a chaotic particle motion would be generated (Figure 1-18 (b)).

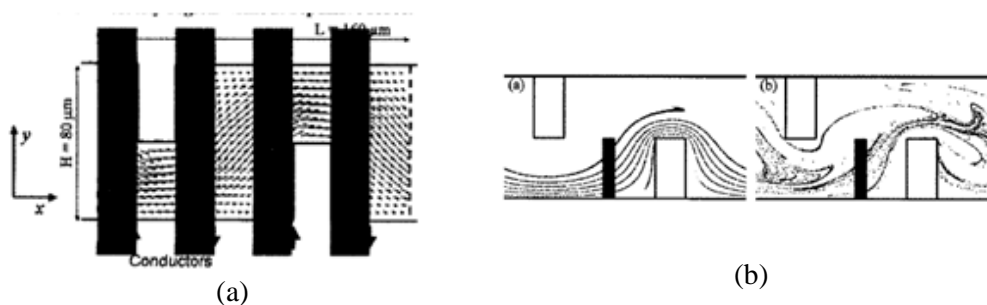


Figure 1-18: Two-dimensional serpentine channel and perpendicular electrodes for chaotic mixing.[46]

Magnetic stir bar: Through careful and complicated microfabrication, a magnetic micro-stir bar was created to mix two streams of liquids by Ryu *et al* [47]. The stir bar was created monolithically using electroplating within a parylene (and later, PDMS) microchannel (Figure 1-19(a)). The stir bar was made of 16 μm thick Permalloy, a ferromagnetic material. It was shown that in order to be useful, the stir-bar needed to be carefully sized such that the gap between the stir-bar end and the channel wall should be as small as possible (Figure 1-19(b)). Mixing improved dramatically as shown in Figure 1-19(c) and nearly complete mixing was obtained after 3 mm of length, compared to only 75% mixing using their previous design. The improvement over simple diffusion was not mentioned.

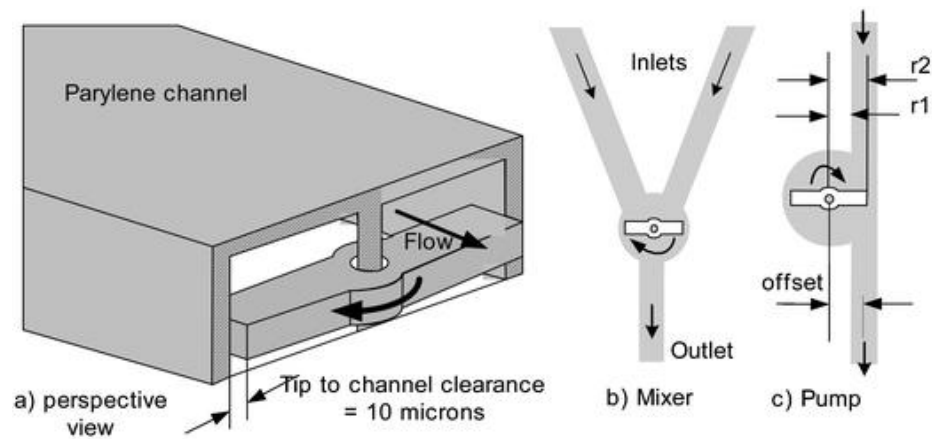


Figure 1-19: (a) Schematic of a micro stir bar contained within a channel. (b) Image of a stir bar within a Y-channel. (c) Stir bar mixing dye and water streams. [47]

1.4.9 Finite Element Models of AC Electrokinetics

The work in this thesis relied heavily on two related finite element models of AC electrokinetic effects in a microchannel. The goal of the first model was to describe the forces that act on a microparticle due to a combination of the three AC electrokinetic effects (ACEO, DEP and ETE). The goal of the second model was to understand how ACEO would affect transport limited binding kinetics of a heterogeneous immunoassay. This section will serve as a brief introductory primer on these models. More detailed discussions of the exact methods used (including equations and boundary conditions) as well as results and discussion may be found in following sections as follows:

Combined AC Electrokinetic Force model: Methods - Section 2.5 on page 83; Results – Section 2.5.2 on page 88.

ACEO Enhanced Immunoassay Model: Methods - Section 3.3 on page 109; Results – Section 3.3.2 on page 112.

(1) AC Electrokinetic forces model

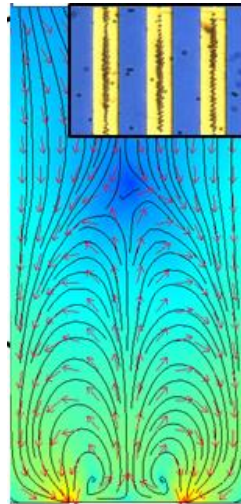


Figure 1-20: Example force mapping simulation result and a comparison of particle observations under the same conditions.

The three AC electrokinetic forces each required their own method of modeling.

DEP force is modeled by solving the electric field simulation and extracting the gradient of electric field. This is combined with electrical constants and the Clausius-Mossotti factor, which determines the direction of the DEP force and is a function of frequency, particle geometry, and particle and fluid electrical properties.

The ETE is modeled by first solving the electric field simulation. Next, a conduction heat transfer simulation is used to determine the temperature field caused by the electric field via Joule

heating. Finally, a fluid dynamics simulation is used to determine how the combination of electric field and temperature gradients cause fluid flow through the electrothermal effect.

ACEO can be modeled directly as a boundary condition in a fluid dynamics simulation since the source of the bulk motion is the movement of the electric double layer which is very thin compared to the channel height. An equation for ACEO slip velocity was placed on a boundary which represents the electrode surface.

Each of those effects causes a discrete force on a particle, either directly through the DEP force, or through viscous drag as the fluid is moved around the particle due to the hydrodynamic effects - ACEO or ETE. A force summation strategy was used to determine the magnitude and direction of force for a given particle type at each location in the microchannel. An example force mapping is shown in Figure 1-20.

(2) *AC Electroosmosis-aided heterogeneous assay*

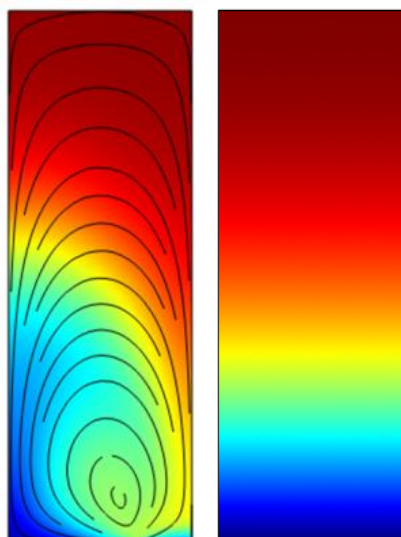


Figure 1-21: (left) ACEO mixing in a microchannel compared to (right) static binding of IgG on a functionalized surface. The colors represent the concentration of analyte (red is highest and blue is lowest).

The simulation to determine the effects of ACEO on heterogeneous immunoassays consisted of three linked simulations. First, in a method similar to that described in the previous section, ACEO was modeled using a function for ACEO velocity as a slip boundary condition on the bottom electrode. Next, a convection diffusion model was used to determine the movement of matter in the reaction chamber. Finally, a reaction was simulated on a boundary which removed mass from the bulk solution and accumulated at the boundary. An example of a concentration map simulated for a mixed sample compared to an unmixed sample is shown in Figure 1-21.

1.4.10 Fundamentals of Biosensors

The process of biosensing, starting with sample collection and ending in notification of results is depicted schematically in Figure 1-22. The process starts with sample collection. There are numerous methods for sample collection but since the focus of this thesis work is in immunoassays, we may consider blood sample analysis, since this is where the relevant immunological entities are often located.

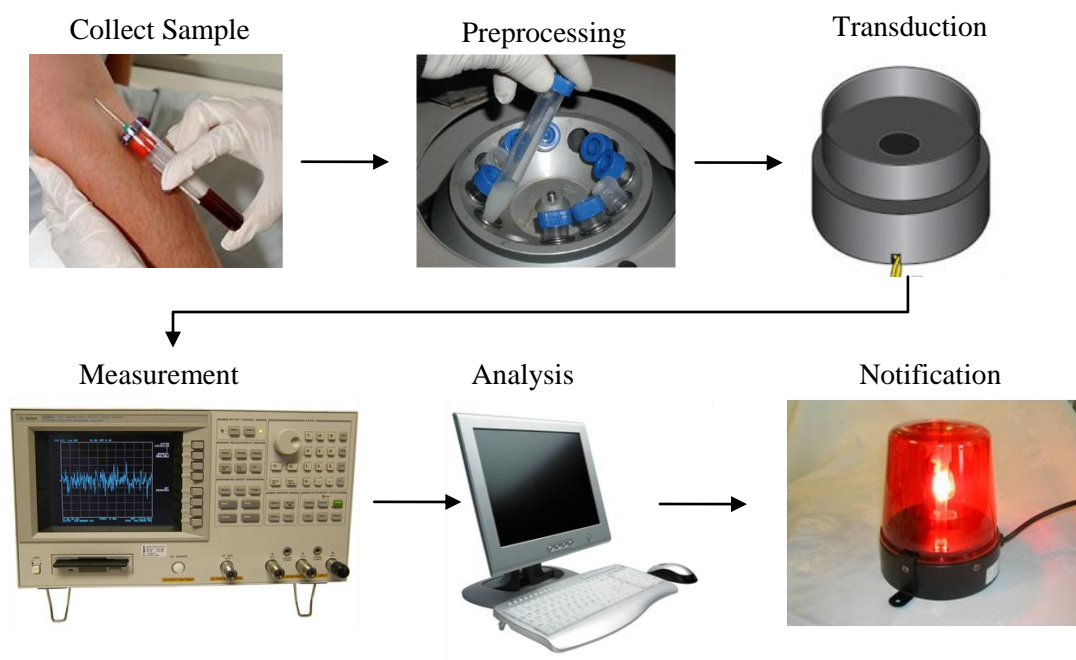


Figure 1-22: Schematic of general biosensing steps.¹

¹ Image Credits:

Biological samples are usually very complex, consisting of many types of materials of various sizes. After the sample has been collected, there is usually a pre-processing step. For example, blood chemical analysis usually is preceded by separation of particulates (e.g. red and white blood cells) followed by a reaction or incubation step; nucleic acid analysis often involves cell lysis and PCR; and many different tests may require the addition of anti-coagulation factors to prevent the formation of thrombi.

Next, the sample is passed onto the heart of the system, the biosensor. The role of the biosensor is to selectively convert some physical property of the measurand into an electrical signal that can be measured electronically. In order to accomplish this, two components are necessary. (1) a biological capture or reaction region, which provides the selectivity, is coupled to (2) a transducer, which provides the transformation of the relevant properties to an electrical signal. Broad categories of transducers include optical, piezoelectric, electrochemical and thermal. A good biosensor system will provide sufficient sampling rate, good selectivity and sensitivity, low

http://www.pharmaceutical-technology.com/contractor_images/cepha/new3.jpg

http://biology.clc.uc.edu/fankhauser/Labs/Genetics/DNA_Isolation/DNA_Isolation_jpg/05_centri_fuge_P2060005.jpg

<http://spreggo.com/blog/wp-content/uploads/2008/03/transducer.jpg>

<http://www.svliquidate.com/graphics/imagesupload/25514-2.jpg>

<http://www.hudsonlibrary.org/Hudson%20Website/Computer%20Lab/MPj04100840000%5B1%5D.jpg>

http://www.partyhireauckland.co.nz/Products/Photos%5CLighting%20&%20Effects%5Cred%20siren%20light_lg.jpg

detection limit, high dynamic range and a host of other important characteristics. The most common biosensor capable of performing direct detection of an analyte is the surface plasmon resonance (SPR) optical biosensor [5] which measures the resonance behavior of electrons at a metal surface. Scientific literature is replete with cases of the others. A focus of this research was on quartz crystal microbalances (QCM) which fall into the class of piezoelectric acoustical transducers.

The sensor measurement system, data acquisition system and analysis steps are electrical components and, in an academic environment, are often accomplished with separate instruments. The raw electrical signal is sent from the measurement system to the data acquisition system where it undergoes signal processing (e.g. Fourier transforms, filtering, etc...). The analysis phase is usually accomplished with a computer and will determine what form of notification to give to an operator. Ultimately, engineers envision replacement of most of the electrical systems with CMOS versions.

(1) Quartz Crystal Microbalance

The quartz crystal microbalance (QCM), also known as a thickness shear mode resonator (TSM), is generally used as a mass sensor. It consists of a thin disk of AT cut quartz sandwiched between two gold electrodes. Application of a potential causes the deformation of the crystal in shear mode (the top of the disk moves in a direction normal to the thickness). Supplying an AC signal causes the crystal to vibrate, and, at a certain frequency will attain resonance. In a vacuum or gas phase, a change in mass on the surface of the sensor results in a proportional change in resonance frequency. This relationship was first described by Sauerbrey [48] in his now famous equation.

$$\Delta f = -\frac{2f_0^2}{A\sqrt{\rho_q\mu_q}}\Delta m = k \cdot \Delta m \quad 1.1$$

where Δf is the frequency shift, f_0 is the resonance frequency, A is the active area of the sensor, ρ_q is the density of the quartz, μ_q is the shear modulus of quartz and Δm is the change in surface-bound mass. For a given QCM, the constants on the right hand side may be lumped together to form a sensitivity factor, k . For a 10 MHz crystal, k is about 2.89 Hz/ng. The Sauerbrey equation only applies to QCM operation in vacuum or air. An equivalent electrical circuit for the QCM operating in vacuum is shown in Figure 1-23. Here, “ L_s , is dynamic inductance (oscillating mass of the quartz), R_s , is dynamic resistance (frictional damping of the quartz slice), C_s is the dynamic capacitance (elasticity of the oscillating body) and C_0 is static capacitance (capacitance between the metal electrode contacts on the crystal).” [49]

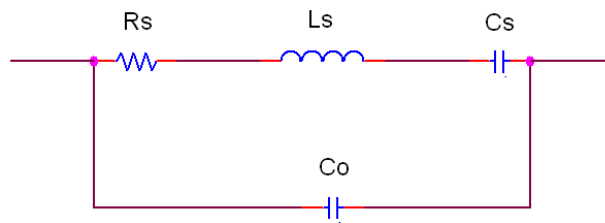


Figure 1-23: Equivalent electrical circuit for a QCM operating in a vacuum

Tracking of resonance frequency in this state may be accomplished by measuring the S21 response for a frequency range near the resonance frequency (see Figure 1-24). At resonance frequency, the system experiences the lowest electrical impedance since the series inductance and

capacitance are canceled. We may therefore track the position of maximum amplitude of the S21 parameter. Also, the spectrum shows that the system experiences a phase shift from $+90^\circ$ to -90° at resonance when the quartz changes from capacitive to inductive. Resonance frequency measurement using the 0 phase angle crossing point is also possible, and in many cases, is more accurate.

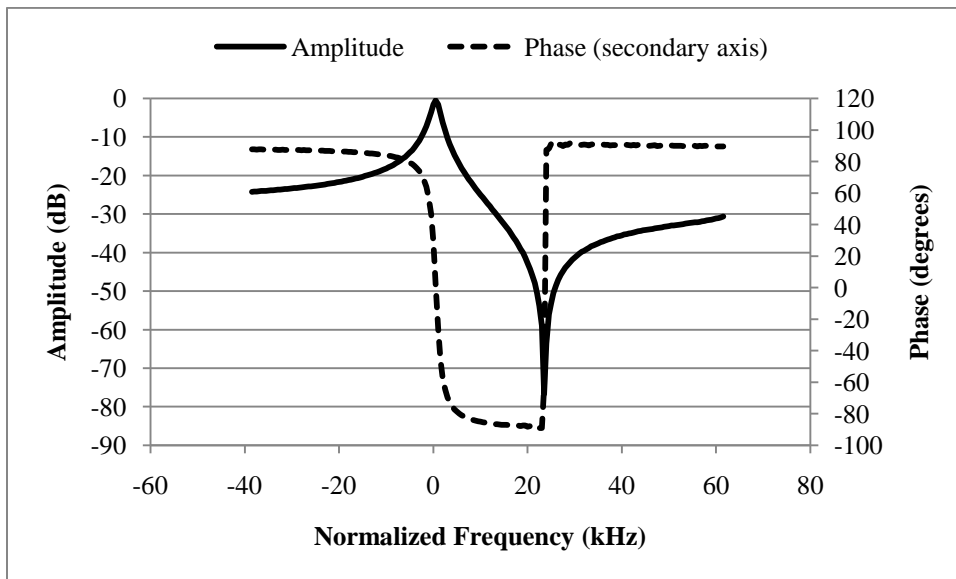


Figure 1-24: S21 gain and phase response of an unloaded QCM.

Operation of the QCM in a liquid environment also affects the resonance properties. An equivalent electrical circuit for a loaded QCM is shown in Figure 1-25. The basic components of the QCM (R_S , L_S , C_S and C_0) are accompanied in this loaded state by (R_L and L_L). R_L represents the energy losses in the liquid and L_L the mass of the vibrating liquid. [50]

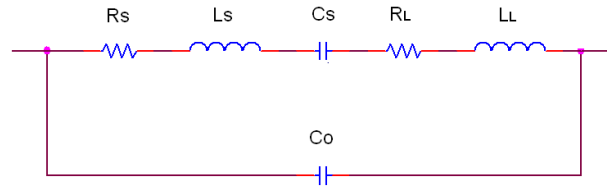


Figure 1-25: Equivalent electrical circuit of a loaded QCM. [49]

The application of a liquid to one surface of a QCM results in viscous loading. The shift in resonance frequency due to this loading was described by Kanazawa et al in a landmark paper [51].

$$\Delta f = -f_0^{2/3} \sqrt{\frac{\rho_L \mu_L}{\pi \rho_q \mu_q}} \quad 1.2$$

where ρ_L is the density of the liquid and μ_L is the viscosity of the fluid. One of the side effects of operating in liquid is a reduction in Q or quality factor, as measured by $\frac{f_0}{\text{bandwidth}_{-3dB}}$. Q represents the “sharpness” of the resonance peak, and will be related to the noise of the system. A consequence of lower Q is higher noise levels and therefore a smaller signal to noise ratio.

CHAPTER 2: COMPREHENSIVE ANALYSIS OF PARTICLE MOTION UNDER NON-UNIFORM AC ELECTRIC FIELDS IN A MICROCHANNEL

2.1 Problem Statement

There is currently an unmet need for a comprehensive analysis of the forces generated by AC Electrokinetics. Currently, no method exists to predict the behavior of particles and fluids under a wide variety of conditions where multiple phenomena are involved. Nor is there a way to understand what contribution each force provides to the overall system, how those forces are distributed throughout the chamber space and how their contributions change with a wide variety of operational and system parameters. A tool for accomplishing this is essential for the application of these forces to solve problems (namely, in this thesis, the problem of how to stir a heterogeneous immunoassay). The main approach to solving this problem was to develop a finite element model capable of predicting the forces acting on submerged particles by simulating all three of the main AC Electrokinetic forces in a microchamber. The simulation was accompanied by experiments using polystyrene microspheres which were observed under a wide variety of conditions and device types. The experimental observations were compared with the simulation results for corroboration purposes.

2.2 Introduction to AC Electrokinetics

AC electrokinetic phenomena such as dielectrophoresis (DEP), AC electroosmosis (ACEO), and electrothermal effect (ETE) are rapidly becoming an indispensable technology for microfluidic devices and lab-on-a-chip systems. Since Pohl discovered the phenomena in 1970's[52], DEP

has been explored for the manipulation of micro- and nanoscale particles such as polymer micro/nanospheres[53-55], cells[56-60], bacteria[61], viruses[62], DNA[63], and carbon nanotubes[64]. ACEO is a relatively newly discovered phenomenon[65-67] and it has been applied mainly for fluid and chemical species mixing applications in low Reynolds number flows in microchannels [68-70]. ETE has also been applied for mixing applications in a microfluidic device [70].

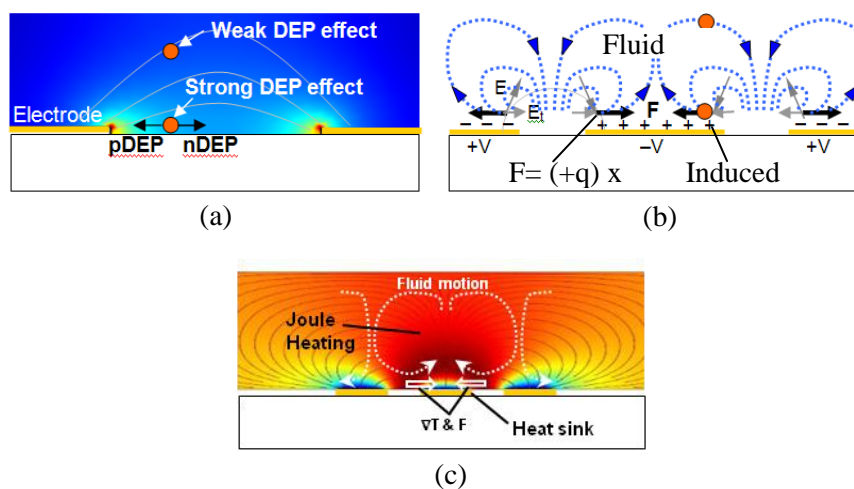


Figure 2-1. Predominant AC electrokinetic behaviors. (a) Dielectrophoresis (DEP), (b) AC electroosmosis (ACEO), and (c) Electrothermal effect (ETE). AC electrokinetic particle manipulation is readily achieved in a microchannel via non-uniform electric fields generated by microfabricated planar electrodes. High electric fields required for particle motion ($10^4 \sim 10^6$ V/m) can be easily achieved with only a few volts since the electrode gap is micro- or nanoscale. The

electrolysis of water is avoided since AC power is applied. Moreover, each of the electrokinetic and electrohydrodynamic (EHD) forces has fairly distinct characteristics and as a result various types of particle motion can be achieved by simply varying operational conditions [71]. This convenience and versatility make AC electrokinetics the most suitable particle manipulation technique for microfluidic devices compared with other techniques such as optical tweezers[72-73], ultrasonic techniques[74], and magnetic techniques[75-77].

In order to fully leverage the capabilities of devices which use AC electrokinetics a comprehensive understanding of the varied and competing forces is required. So far, most studies have only analyzed and simulated a single phenomenon alone. However, it is only under certain circumstances that one phenomenon predominates and all others may be ignored. It is therefore necessary to consider several of the AC electrokinetic phenomena together since they often compete with each other under a wide range of conditions. This paper presents numerical studies that consider all major relevant forces and compares the simulation results with experimental data. The experimental study includes the use of several different device designs and considers the major operational parameters to show the numerous particle behaviors possible. In this way, a comprehensive analysis of particle motion under non-uniform electric fields in a microchannel has been performed. The analysis reported in this article will help further the efforts of scientists and engineers who wish to control the behavior of micro- and nanoparticles in microfluidic environments using AC electrokinetics. It is our hope that this presentation may provide insight and design guidelines to the lab-on-a-chip community.

2.2.1 Brief Overview of AC Electrokinetic Phenomena

The wide range of particle behavior under non-uniform AC electric fields is a result of the numerous physical processes (interfacial polarization, electric double layer formation, fluid

heating, etc.) that occur at both the electrode and particle surface. The three predominant AC electrokinetic phenomena that result are DEP, ACEO and ETE. This section provides a brief introduction to these forces.

DEP occurs when a particle is subject to a non-uniform electric field. The particle will experience a net force either in the direction of higher electric field strength (positive DEP) or lower electric field strength (negative DEP) due to the relative polarizability between the particle and the surrounding media. Both the magnitude and direction of the force is determined by factors such as the electrical conductivities and permittivities of media and particle, particle size, and both the frequency and strength of the electric field. In the case of microfabricated planar electrodes, particles will accumulate at the edges of the electrode under positive DEP, or they will be repelled from this region and travel towards low electric field strength under negative DEP (Figure 2-1 (a)).

Unlike DEP, both ACEO and ETE are hydrodynamic phenomena and cause fluid motion, which brings suspended particles along with it. ACEO is the motion of fluid due to an interaction between an electric field and the electrical double layer (EDL) induced at the electrode surface. If the electric field at this surface contains a tangential component (E_t), the ions in EDL will traverse laterally and drag the fluid along (Figure 2-1(b)). In the case of planar electrodes, a continuous and easily recognizable rotational fluid pattern emerges. This pattern, which can be described as a set of counter rotating vortexes, may cause particles to orbit out of plane near the electrodes or cause them to collect on the electrode itself.

ETE is caused by temperature gradients induced by Joule heating. These temperature gradients create fluctuations in the electrical conductivity and permittivity of the fluid. These fluctuations,

in turn, induce fluid motion through their interaction with the electric field (Figure 2-1 (c)). Like ACEO, electrothermally driven fluid flow can be rotational in nature.

Each of the AC electrokinetic phenomena causes dramatic, organized and often rapid particle motion. With larger particles (greater than 1 μm), collection may occur within seconds and particles may move at hundreds of microns per second. Typically, DEP and ACEO are both used for particle collection and active mixing applications can be performed using ACEO and ETE. An important factor that has great control over the application and the possible AC electrokinetic phenomena that may be used is media conductivity. High conductivity media that is physiologically relevant prohibits positive DEP and ACEO. (This will be further discussed in the Theory section.)

Besides AC electrokinetics, there are several other well studied phenomena that are known to act upon particles suspended in microfluidic environment. Brownian motion, buoyancy, gravity, and natural convection all play roles to some extent.

2.3 Theoretical description of AC Electrokinetic Forces

2.3.1 Dielectrophoresis

The dielectrophoretic force acting on a particle is caused by the interfacial polarization between the particle and the media in a non-uniform electric field. For the case of a solid sphere, the effective dipole moment (p) is expressed as

$$p = 4\pi\epsilon_m \left(\frac{\tilde{\epsilon}_p - \tilde{\epsilon}_m}{\tilde{\epsilon}_p + \tilde{\epsilon}_m} \right) r^3 E \quad 2.1$$

$$\tilde{\epsilon} = \epsilon - j \frac{\sigma}{\omega} \quad 2.2$$

where r is the particle radius, E is the electric field, ϵ_p is the permittivity of the particle and ϵ_m is the permittivity of the media, σ_m is the electrical conductivity of the media, σ_p is the electrical conductivity of the particle, ω is angular frequency, j is the imaginary unit ($j^2 = -1$) [56]. Here the term in the parenthesis is defined as Clausius-Mossotti (CM) factor and is often used as an indicator that describes how the effective dipole moment of the particle varies with the material properties and the frequency of the applied voltage. The time-averaged dielectrophoretic force (F_{DEP}) exerted on a solid sphere is then expressed as

$$F_{DEP} = (p \cdot \nabla)E = 2\pi r^3 \epsilon_m \text{Re}[CM] \nabla |E_{RMS}|^2 \quad 2.3$$

where $\text{Re}[CM]$ is the real part of the Clausius-Mossotti factor.

(1) Clausius-Mossotti Factor

This factor is a function of the complex permittivity of the particle and the media and is bounded by 1 and -0.5 [57-58, 78]. Therefore, not only does this factor partially determine the magnitude of the force, but also its direction. In conditions where a particle is more polarizable than the media, the factor is positive, the particle is said to experience positive DEP and moves towards regions of higher electric fields. If the particle is less polarizable than the media, the opposite is true and the particle moves towards regions of lower electric field as it experiences negative DEP [56, 79].

The CM factor is determined by the three dimensional particle geometry (interior as well as exterior) and by the properties of its constituent materials. In many cases it is difficult to determine an exact expression for an object (for example a Eukaryotic cell, which is composed of many layers of different materials of varying thickness) and the function must be ascertained experimentally.

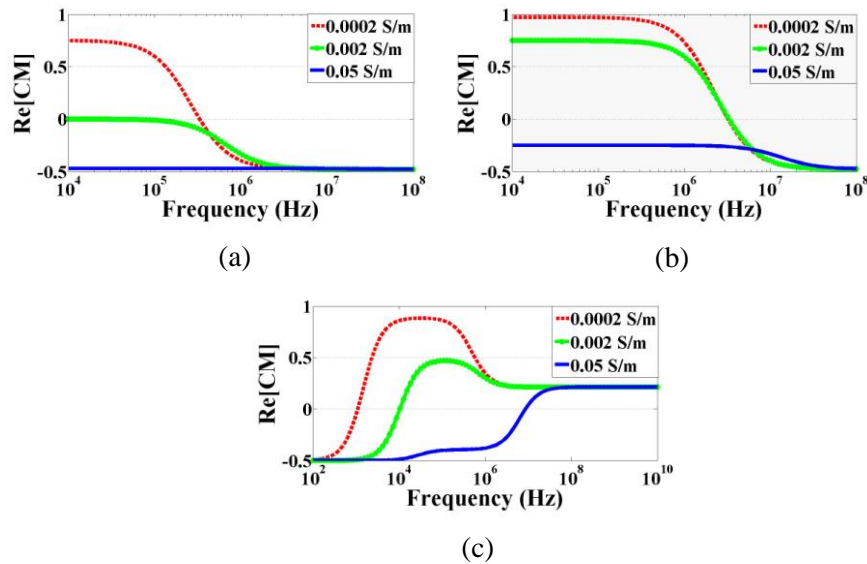


Figure 2-2. Clausius-Mossotti factor as a function of frequency and media conductivity for (a) a solid 2 μm diameter polystyrene sphere (particle permittivity= $2.5\epsilon_0$) (b) a solid 200 nm diameter polystyrene sphere (particle permittivity= $2.5\epsilon_0$), and (c) a shell structure modeled on Chlorella sp. (surface capacitance= $12.4\text{E-}3$ S, radius= $3.29\text{E-}6$ m, inside conductivity= $8\text{E-}3$ S/m, inside permittivity= $150\epsilon_0$) 9

Figure 2-2 shows how the CM factor varies as a function of frequency and media conductivity for both a solid sphere and for a shell structure. For a given particle, the Clausius-Mossotti factor is a function of frequency of the applied electrical signal and the conductivity of the media in which the particle is suspended. For a solid polystyrene sphere with a diameter of 2 μm (Figure 2-2 (a)), the three different media conductivities shown dramatically change the shape of the CM factor. At low conductivity, it is possible to induce positive DEP ($\text{Re}[CM]$ values greater than 0), where particles are attracted to an electrode edge or other high density electric field areas. This occurs

at low frequencies and transitions to negative DEP at high frequencies, where particles will be forced into regions of low electric field strength. For example, particles may accumulate where electric field minima exist, such as on the center of the electrode, between electrodes or may even levitate above the electrodes. As the conductivity is raised, the strength of positive DEP becomes diminished and will eventually disappear completely, to be replaced with negative DEP for any applied frequency.

Since the conductivity of a solid particle is the sum of the bulk and surface conductivities, changing the size of a particle changes its overall conductivity. A solid polystyrene sphere with a diameter of 200 nm (Figure 2-2(b)) therefore has a different CM factor. The surface conductivity is as follows:

$$\sigma_{surface} = \frac{2K_s}{r} \quad 2.4$$

where K_s is the surface conductance and r is the particle radius. The conductivity of a particle with a diameter of 200nm is ten times as large as that of a particle with a diameter of 2 μm . The change in size results in an increase in the value of the CM factor and a shift in transition frequency.

The CM factor for a shell structure (Figure 2-2 (c)) is more complicated. All three conductivities shown exhibit negative DEP at low frequencies and transition into positive DEP as the frequency increases. A peak DEP plateau is seen at mid-range frequencies for lower media conductivities compared to the shell conductivity. For higher media conductivities a transition to positive DEP occurs at high frequencies. CM factor at low frequency goes to -0.5 depending on the

conductivities of shell and media, but this factor at high frequency depends on the surface capacitance, the permittivities of shell and media, as well as the shell radius.

It should be noted that particle separation, one of the most promising applications of DEP, can be easily accomplished by comparing the CM factors of two different particles and choosing an appropriate frequency and conductivity. The solid spheres and shell particles, for example, may be separated with high frequency at any conductivity. The solid particles will experience negative DEP and be repulsed from the electrode edges while the shell particles will experience positive DEP and be attracted to the electrode edges. Furthermore, since the CM factor is a function of particle conductivity, which, in turn is a function of the particle size, two particles of different sizes will have different CM plots. They may then be separated in the same way, by choosing an appropriate media conductivity and frequency of electric signal.

Table 2-1 Comparison of dielectrophoresis (DEP), AC-electroosmosis (ACEO), and electrothermal effect (ETE).

DEP	ACEO	ETE
<ul style="list-style-type: none"> ◆ Electrokinetic force; positive or negative ◆ High dependency on particle size and property (Selective) 	<ul style="list-style-type: none"> ◆ Electrohydrodynamic force ◆ Does not depend on particle size and property (Non-selective manipulation) ◆ Long-range flow (circular motion) 	

manipulation)	◆ Constant flow direction from edge to center of electrode:	◆ Flow direction varies depending on medium conductivity and frequency
◆ Has strong effects near electrode with exponential decrease in force with increasing distance	◆ Frequency-dependence from surface charge and E_t	◆ Frequency-dependence from coulomb and dielectric body force
◆ Frequency-dependence from relative polarizability of the particle and the medium	◆ Conductivity increase leads to lesser ACEO	◆ Conductivity increase leads to greater ETE

(2) *Other DEP Factors*

Besides the CM factor, it is important to note that the DEP force is highly dependent on both the radius of the particle, a cubic relationship, and the gradient of electric field squared. The spatial dependence of the DEP force comes from the gradient of electric field squared. Since the electric field decays exponentially with the distance from the electrodes, the DEP force remains strong only near the electrodes. Also, the DEP force is proportional to the square of the amplitude of the applied voltage and inversely proportional to the cube of electrode gap. For example, if the electrode gap is reduced 10 times, the DEP force is increased 1000 times. Table 1 summarizes the characteristics of the DEP force in comparison with ACEO and ETE.

2.3.2 AC Electroosmosis

ACEO occurs when mobile counter ions in the diffuse electric layer, which is induced by electrode polarization, interact with the electric field. In the case of parallel planar electrodes, the field contains a tangential component that induces counter ion movement towards the center of the electrode (Figure 2-1(b)). The direction of the movement does not change with a potential switch because the counter ions are switched as well. The motion of the ions drags the bulk fluid along the surface, generating a rotational motion of bulk the fluid in the microchannel.

The time-averaged AC electroosmotic velocity on two parallel electrodes is derived by Ramos *et al* assuming a linear relationship between the surface charge and the potential and neglecting the stern layer. The ACEO velocity expression is as follows:

$$V_{ACEO} = \left(\frac{\varepsilon \varphi_0^2 \Omega^2}{8\eta x (1 + \Omega^2)^2} \right) \quad 2.5$$

$$\Omega = \frac{1}{2} \pi \kappa x \left(\frac{\varepsilon_m}{\sigma_m} \right) \omega \quad 2.6$$

where φ_0 is the initial potential, Ω is a non-dimensional frequency defined as above, η is the dynamic viscosity, x is cross-sectional position and starts from the center of the gap between the electrodes and κ is the reciprocal of the Debye length. This equation is generic and may be applied to electrodes of varying geometries. It is important to note that only the values of the function that lie within the range of the electrode are used. The function cannot be applied to regions which are over the electrode gap since there are no induced counter ions in this region [56, 79].

Figure 2-3 shows the AC electroosmotic velocity as a function of frequency and position on an electrode. The velocity is always greatest at the edge and decreases as the center is approached. The velocity also is zero at low and high frequencies and reaches a maximum at mid-range frequencies.

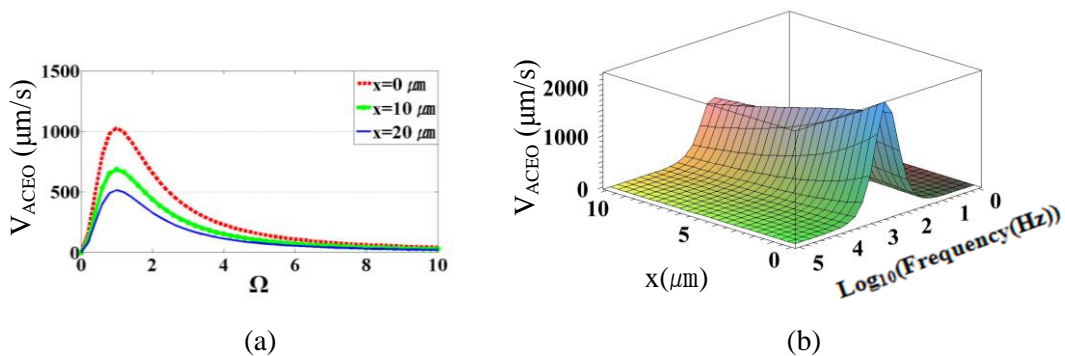


Figure 2-3. Using equation (5), AC electroosmotic velocity is plotted as a function of (a) Ω at different locations (x) from the electrode edge and (b) frequency and distance (x) from the electrode edge at 0.0002 S/m, 1 V, and 20 μm gap between electrodes.

2.3.3 Electrothermal Effects

Like ACEO, ETE is a hydrodynamic phenomena and acts on a suspended particle only through fluid drag. The passage of current through the bulk fluid causes Joule heating according to the expression:

$$k\nabla^2 T + \sigma E^2 = 0 \quad 2.7$$

where k is thermal conductivity, T is temperature in Kelvin, σ is electrical conductivity and E is the magnitude of the electric field. In this equation, the unsteady and convection terms are neglected. In order to determine the effect of the thermal gradients on the fluid motion, the conductivity and permittivity gradients must be determined. This is done using following relationships that show the dependence of the electrical permittivity and conductivity on the temperature for water [80]:

$$\alpha = \left(\frac{1}{\varepsilon}\right) \left(\frac{\nabla \varepsilon}{\nabla T}\right) = -0.4 \% \text{ K}^{-1} \quad 2.8$$

$$\beta = \left(\frac{1}{\sigma}\right) \left(\frac{\nabla \sigma}{\nabla T}\right) = 2 \% \text{ K}^{-1} \quad 2.9$$

Next, the electrohydrodynamic force (F_{ETE}) caused by the conductivity and permittivity gradients is calculated according to the time-averaged electrothermal force equation per unit volume.² This neglects the resulting fluid convection, which is slower than the charge organization. This force is as follows:

$$\begin{aligned} \vec{F}_{ETE} &= -0.5 \left[\left(\frac{\nabla \sigma}{\sigma} - \frac{\nabla \varepsilon}{\varepsilon} \right) \vec{E} \frac{\varepsilon \vec{E}}{1 + \omega \tau} + 0.5 |\vec{E}|^2 \nabla \varepsilon \right] \\ &= 0.5 \varepsilon \nabla T \vec{E}^2 \Pi(\omega) \end{aligned} \quad 2.10$$

where Π is a unit-less function of frequency:

$$\Pi(\omega) = \left(\frac{\alpha - \beta}{1 + \omega \tau} - \frac{\alpha}{2} \right) \quad 2.11$$

where τ is the charge relaxation time (ε/σ). Π (shown in Figure 2-4) determines the direction of the force and also plays a role in determining its magnitude. When the left term is greater than the right, Π is positive and the fluid flows from the electrode edge to the center (the same as for ACEO). For negative values of Π , the flow pattern is in the opposite direction.

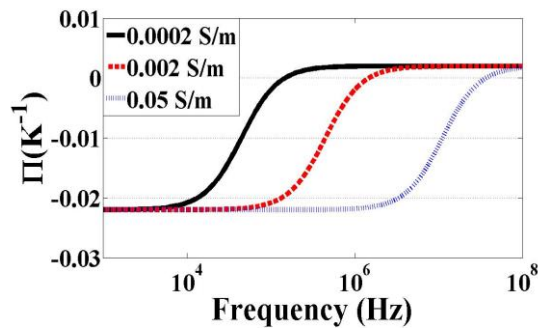


Figure 2-4. Π of ETE as a function of frequency with three different conductivities.

The fluid velocity can be calculated using F_{ETE} as a body force on the liquid once the temperature gradient and electric field are known. It is important to note that both gradient of temperature and

electric field are functions of amplitude. Though temperature gradient depends on the geometry of the system, analytical approximations for similar geometries estimate this temperature gradient to be proportional to voltage squared.² Together, gradient of temperature and electric field squared makes the total force proportional to voltage to the fourth power. Generally, when frequency or conductivity are high and ACEO ceases to play an important role, ETE can predominate, especially if the applied voltage is large.

Another source of temperature gradient in the media can be due to external heating of electrodes such as from a microscope light. The presence of this heat source causes fluid motion in much the same way as from Joule heating except that the direction is reversed. This is due to the reversal of the temperature gradient. For ETE, the fluid is heated from the electric fields and the electrodes (nearly) maintain their temperature and act as heat sinks. In the case of external heating, the electrodes become the heat source as they are heated by the light which passes through the transparent electrode gaps. This effect has been reported before but did not seem to play a significant role in experiments. With no applied electrical signal, particles were not observed to move (except by Brownian motion) under the presence of microscope lights. These temperature gradients also give rise to natural convection. However, these effects were also eliminated from the simulations because its effect is known to be much less than ETE as considered above.²

2.4 Experimental Observations of Microparticles in Nonuniform

Electric Fields

2.4.1 Experimental Method For Observation of Microparticles In The Presence of

AC Electrokinetics

(1) *Microfabricated devices and materials*

Each device used for experimental studies consists of a glass substrate (Pyrex 7740) containing planar gold electrodes of various designs. A PDMS membrane, containing a recessed chamber was then placed on top of the glass to form a completed channel.

All of the thin-film electrodes were fabricated using the well known lift-off process.

Photolithography was performed on 3-inch Pyrex glass wafers. Negative photoresist (Futurrex NR-7 1500PY) was spincoated onto the substrate followed by exposure and development to create a negative mask pattern prior to metal deposition. Next, 30 nm of titanium and 200 nm of gold were evaporated on top using an electron beam evaporator, followed by lift-off using acetone.

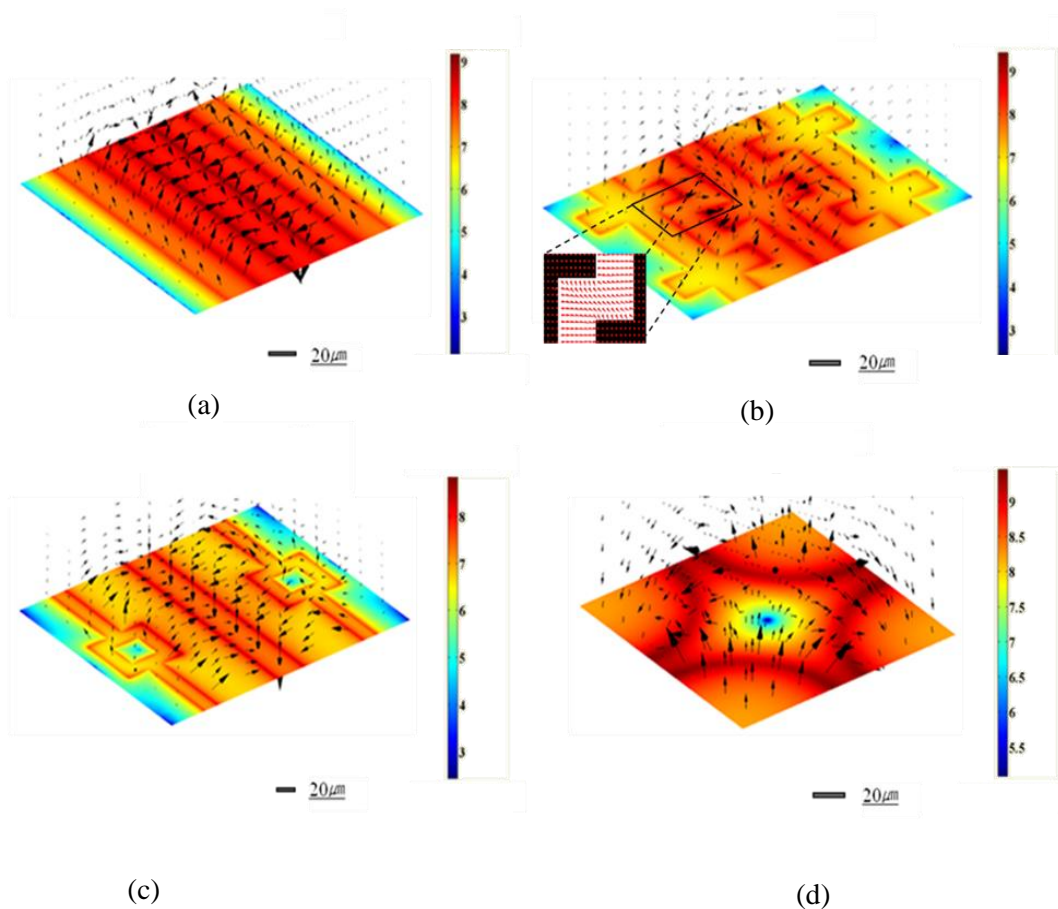


Figure 2-5. 3D simulation for (a) Parallel interdigitated, (b) Castellated, (c) Pocket well and (d) Quadrupole electrodes at $0.354 \text{ V}_{\text{rms}}$. (Surface plot: $\text{Log}_{10}(|\nabla|E_{\text{rms}}|^2) [\text{V}^2/\text{m}^3]$, Arrow: Electric field [V/m]). In the castellated electrode plot, a small normalized arrow plot at the corner shows the electric field direction $1 \mu\text{m}$ off the surface of the substrate. Black areas are the electrodes and the white area is the inter-electrode space.

The microchannels were fabricated using PDMS replica molding. The microchannel molds were created on a $2 \times 2 \text{ in}^2$ Pyrex glass plate using negative photoresist (SU-8 2035). A PDMS mixture

(10:1 of Sylgard 184 base resin to curing agent) was then poured onto the negative mold pattern. A 30 minute degassing step in a vacuum desiccator, followed by baking at 80°C for 2 hours took place. After baking, the fully cured PDMS was peeled off and cut into individual devices. Holes with approximately 1 mm in diameter were punched into either side of the channel to form an inlet and outlet. The completed microchannels were 100 μm high, 1 mm wide and 1.1 cm long.

Assembly of the device consists of placing a PDMS channel on top of the electrode pattern and applying gentle pressure to ensure adhesion. Electrical connections were made by attaching wires to the planar electrodes with an electrically conductive adhesive. Figure 2-6(a) shows an assembled device and electrodes with different patterns used in the experiments. The four electrode types used are the parallel interdigitated, castellated interdigitated, quadropole and pocket well designs (also shown in Figure 2-6(a)). To understand the distribution of the electric field and the locations of the minima and maxima of the $\nabla|E|^2$, Figure 2-5 shows 3D simulation results for each electrode geometry.

(2) Particles and solution preparation

Polystyrene microbeads (Polysciences, Inc.) were added to aqueous solutions to make a colloidal mixture for the experiments (0.05 g/ml). Microbeads with diameters of 2 μm and 200 nm were used. KCl was added to deionized water to control the media conductivity. Two different colloidal mixtures were prepared for the experiments: a low conductivity mixture (0.0002 S/m) and a high conductivity (0.05 S/m) mixture. The conductivity of each solution was measured by a conductivity meter (Orion Model 105A+).

(3) Experiment Procedure

The experimental setup consists of a microscope (Nikon Eclipse ME600) equipped with a CCD camera and a function generator (HP 33120A 15MHz), which connects to an assembled device

placed on the microscope stage. In order to better visualize particles on electrodes, an external, through-objective light source was used.

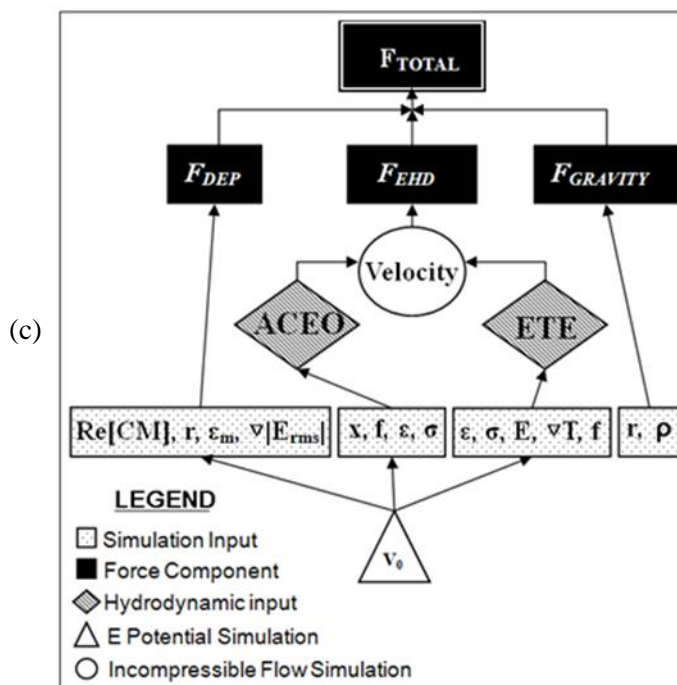
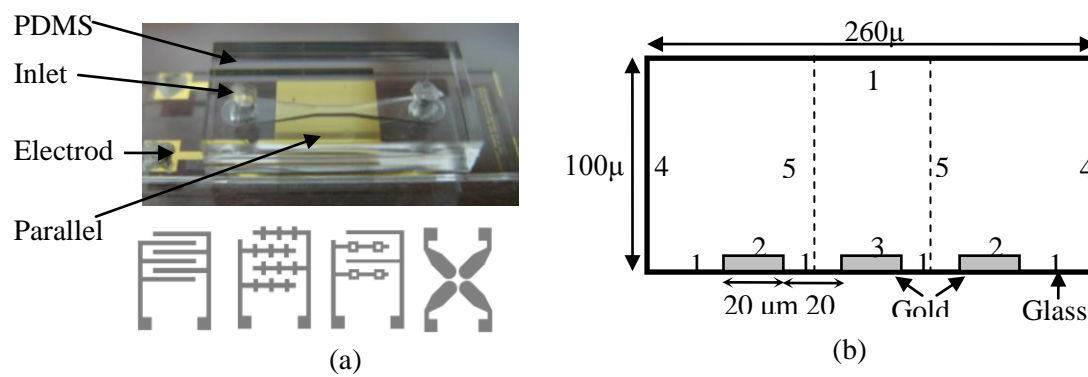


Figure 2-6. (a) An image of an assembled device. Conceptual drawings of the four electrode types, (from left to right) parallel interdigitated, castellated, potential well and quadrupole are shown. (b) Geometry (cross-sectional view of the microchannel) and boundary conditions for

numerical simulation. For the electrostatics simulation: Zero charge on 1 and 4; $V_0 = V_{\text{rms}}/2$ on 2; $V_0 = -V_{\text{rms}}/2$ on 3; continuity for 5. For the convection and conduction simulation: Thermal insulation on 1; zero heat flux on 4 and 5; and fixed temperature on 2 and 3. For the incompressible Navier-stokes simulation: 0 pressure on 4; No slip on 1; slip velocity (electroosmotic velocity) on 2 and 3; and symmetry conditions on 5. (c) Simulation strategy flow chart

There were four electrode types and two conductivities used for each experiment. This makes for a total of 8 experimental conditions. For each condition, the selected electrode device was assembled and the appropriate solution (high or low conductivity) was injected into the chamber. Then, a time course of different frequency and voltage settings was supplied by the function generator while the CCD camera recorded the behavior of the particles.

Parallel and Castellated: For the parallel and castellated electrode types, two different voltage settings were used ($1 V_{\text{pp}}$ and $2 V_{\text{pp}}$). For each voltage setting, a time-course of frequency settings was applied, whereby the frequency was incrementally increased from 1 kHz to 1 MHz.

Quadropole and pocket well: The quadropole and pocket well electrode types are designed to be used as particle traps using negative DEP. For this reason, a high frequency setting was used (15 MHz) where negative DEP is dominant. For these experiments, the frequency remained constant while the voltage was increased incrementally from 0 to 10 V in steps of 2 V.

2.4.2 Characterization and Analysis of Particle Behaviors

Using a microscope to observe the motion of particles under non-uniform AC electric fields shows the versatility and dramatic capabilities of AC electrokinetics. By simply adjusting the frequency, a wide range of distinct, directed and highly organized particle behaviors can be perceived. The immediate and rapid nature of this movement is striking, as particles become assembled or repelled within a few seconds to a few minutes, though this depends highly on the size of the particles and other experimental conditions. In general, higher voltages increase the magnitude of each phenomenon but sometimes different effects are observed at different voltages even while maintaining the same frequency. Different conductivities can adjust the prevalence or strength of some phenomena, restrict them completely or bring about entirely new phenomena altogether. In general, five distinct behaviors can be identified and will be discussed in brief.

(1) Particle collection on the electrode center – Assembly-lining (ACEO dominant)

In low frequency ranges (1-30 kHz) and in low media conductivity (0.0002 S/m), particles experience strong ACEO (Figure 2-3) and are rapidly dragged towards the center of each electrode. A small number of particles are initially in rotational motion but soon come to rest and collect on the center of the electrode as well. Positive DEP is also present in these conditions (Figure 2-2 (a)) and causes particles to be attracted to the electrode edges. Particles in the middle of an electrode will experience a net downward force due to DEP. The result is that the combination of DEP and ACEO forces causes particles to be trapped along the center of an electrode. Examples of this behavior for parallel electrodes can be seen in

Figure 2-7.

In the parallel electrode case, the aligned particles are sometimes referred to as an “assembly line.” If the particle concentration is low (

Figure 2-7(a)), the particles are collected in the center of the electrode as a linear pattern with a constant interval. The interesting nature of this constant interval may be explained by the

repulsion of two similar particles when they are aligned perpendicularly to the direction of the electric field. In this low frequency and low conductivity case, where particles are more polarizable than the media, a region of low electric field strength exists between the particles and is intensified when such particles approach. Since the particles experience positive DEP, they will move away from this region and thus be repulsed. The EHD flow keeps the particles from forming the particle chains that this phenomenon would otherwise create.

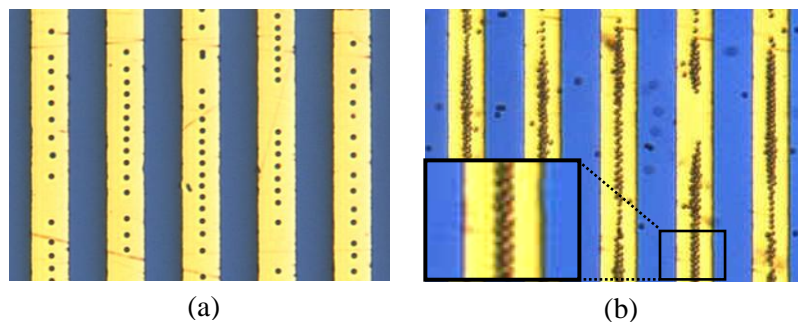


Figure 2-7. Parallel interdigitated electrodes with 2 μm diameter polystyrene microbeads at 1 kHz and 1 V suspended in 0.0002 S/m media with (a) low concentration of particles and (b) high concentration of particles

When the particle concentration is high (

Figure 2-7(b), the collected particles form a zig-zag or close-packed assembly. As will be discussed in the particle chains section, depending on their orientation within the electric field,

two nearby particles may experience either repulsive DEP forces or attractive DEP forces. It is hypothesized that the particles form such organized patterns in order to find a stable arrangement where the repulsive forces of DEP are minimized and the attractive forces of DEP forces are maximized as they are forced towards the center of the electrode due to the EHD forces. In the castellated electrode case, this behavior results in particles collecting at each electrode intersection in a remarkably clear “diamond” shape (Figure 2-8 E1, E2, F1, F2).

Figure 2-8 shows the changes in particle motion as a function of frequency. As the frequency is increased, the balance between the two major competing phenomena starts to shift. Particles spread out on the electrodes as the effect of ACEO is diminished and thus positive DEP begins to play a stronger role (Figure 2-8 A2, B2, and E2).

(2) Particle collection on the electrode edge (positive DEP dominant)

In Figure 2-8 (A3 and B3) particles are seen to be collected along the edge of the electrodes. This is indicative of positive DEP and the particles move towards areas of high electric field strength. This occurs in mid-range frequency settings (100kHz – 500kHz) at lower conductivity. At slightly lower frequencies than this, particles migrate to the edge of the electrode from the center but they spin right on the edge, indicating the remaining effect of ACEO. These particles are then fixed at the electrode edge at ~100 kHz. For the castellated electrode case, the areas of strongest electric field are the outside electrode corners and particles congregate there readily (Figure 2-8 E3).

(3) Levitation or repulsion of particles from electrode edge (negative DEP dominant)

At high frequencies (>500 kHz) particles experience strong negative DEP forces, which propel particles towards regions of low electric field and levitate up into the media as seen in Figure 2-8 (A5, B5, C5, D5, E5 and F5).

(4) Particle behaviors on the parallel and castellated electrode types

Electric field minima can occur in-between electrodes and at the center of the electrode (Figure 2-5 (a and b)). If the particles have been previously collected at the edge of the electrode and formed particle chains due to positive DEP, they will move to the gap between electrodes. However, if the initial condition was random distribution of the particles, they may either be pushed towards the gap between electrodes or the center of the electrodes, depending on their starting position. At the frequency of approximately 1 MHz and above, most of the particles levitate up into the media to the point where the negative DEP force is balanced with the gravitational force.

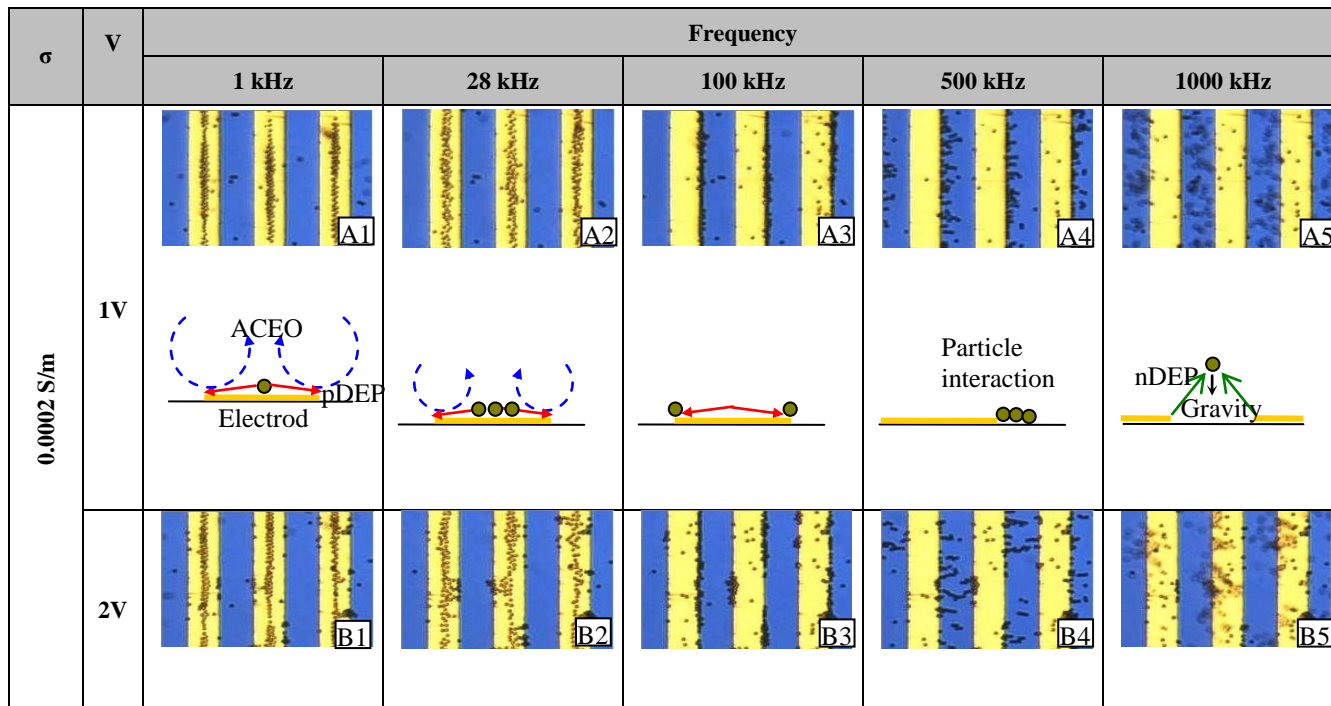


Figure 2-8. Experimental results at selected frequencies and voltages for the parallel and castellated interdigitated electrodes using two different conductivities. 2 μm diameter polystyrene microspheres were randomly dispersed before a signal was supplied.

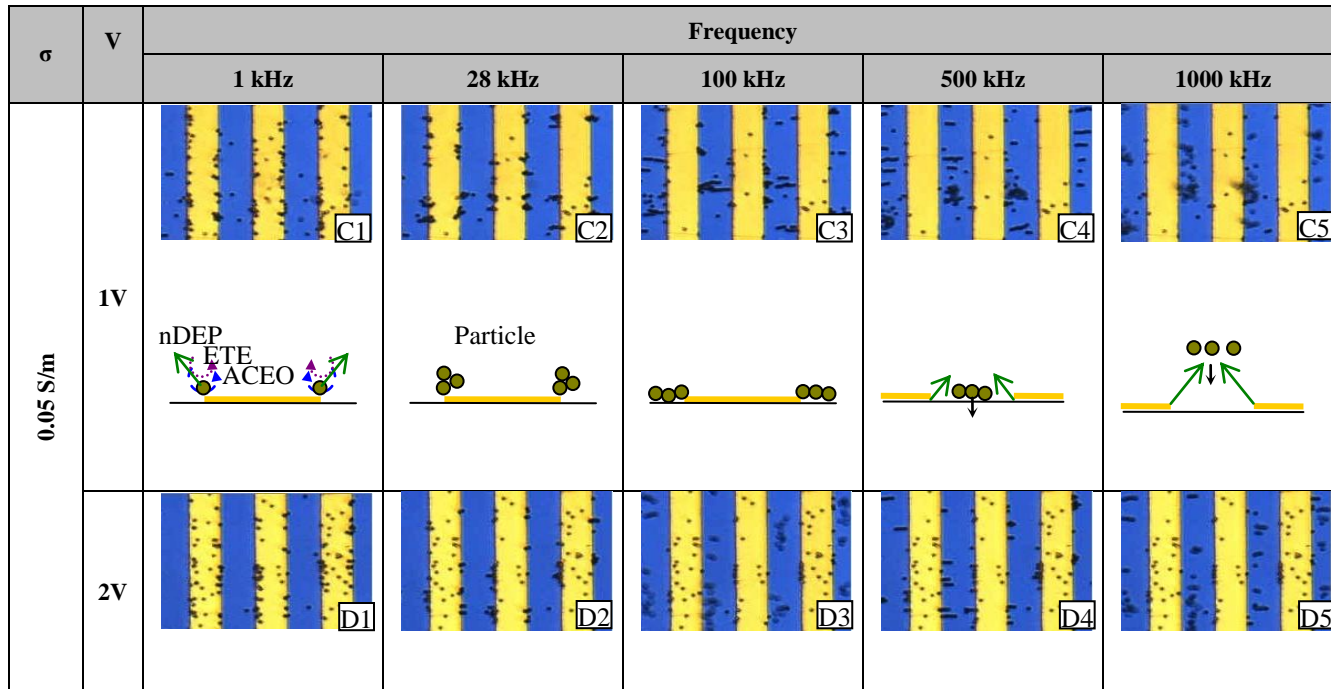


Figure 2-8 (continued).

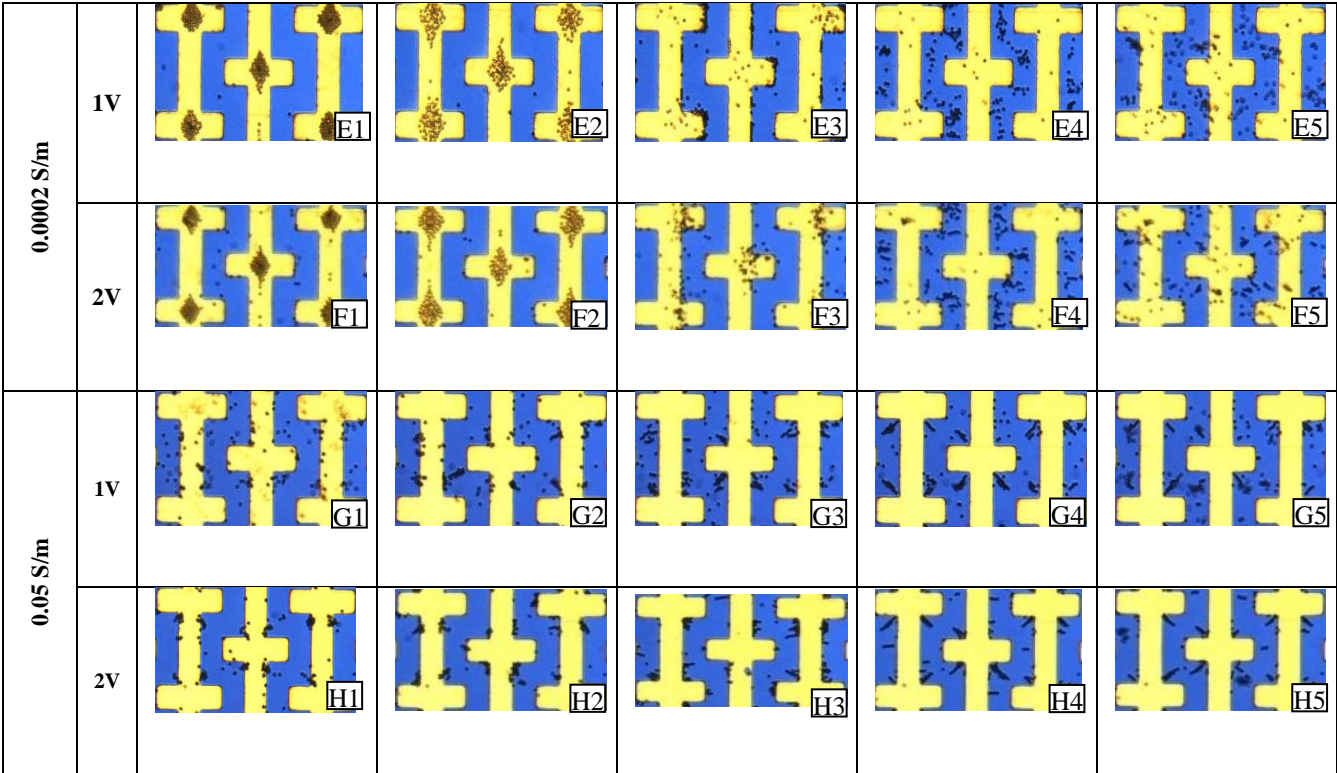


Figure 2-8(continued)

1 Potential well and quadrupole

The quadrupole electrode type and potential well electrode type are designed to be particle traps through negative DEP. With the use of high frequency in either low or high conductivity, the particles are repelled from the edges of the electrodes and move either in between the four electrodes in the quadrupole case or congregate within the geometrical pocket within the potential well electrode (see the electric field minima shown in 3D Figure 2-5(c and d). They have been used as such and the images may be seen in Figure 2-9. Note that the higher the voltage, the more tightly focused the particles become. Furthermore, not only are the particles collected within the gap between the electrodes, but in the quadrupole case, they are also moved toward the center of the electrode itself, where another electric field minimum exists.

2 Particle chains (particle-particle interaction)

At certain frequencies, suspended particles begin to form “pearl chains” where they stretch away from electrodes, with the centerline parallel to the electric field. Sometimes the particles may bridge the entire gap between electrodes. This interesting behavior is caused by attraction between particles due to either positive or negative DEP. As mentioned previously, particles aligned perpendicular to the direction of electric field will repel each other. A more stable arrangement is with particles aligned with the electric field. Under conditions where the CM factor is positive, a region of high electric field will exist between the particles, causing the particles to attract under positive DEP. In conditions of negative CM factors, there will be regions of low electric field strength between the particles and they will also attract, this time due to negative DEP [79].

In some cases, positive DEP between particles and the electrode is still present with enough strength to keep the pearl chains rooted at the electrode edge. However, the strength of the

particle-particle attraction is greater than that of the DEP between particles and the electrode and so particles align. This behavior may be clearly seen in the parallel electrode case in Figure 2-8 (A4 and B4). A similar case may be seen at high conductivity in Figure 2-8(C3). However, unlike the low conductivity cases, the particles are not as stable and stationary as they are not firmly “rooted” to the electrode by positive DEP. Instead, a close inspection of a video reveals that in most cases, the root particles are undergoing slight orbital movement, which indicates ACEO or ETE is in effect. (The simulation study shows that the ACEO effect is much stronger than ETE for the given conditions.) It is likely that these situations show a force balance between ACEO and negative DEP and the particles are free to form pearl chains in this equilibrium. When the frequency is raised, negative DEP overcomes the ACEO and the pearl chains become uprooted, as shown in Figure 2-8(C4). The particles are then levitated as the frequency further increases and the chains are decomposed into individual particles as they move away from the electrode and the DEP forces decrease.

For the castellated electrodes, an interesting particle organization occurs. Pearl chains form with particles stretching from the inside corner of one electrode towards the outside corner of an adjacent electrode as can be seen in Figure 2-8(G4, H4). In the case of the castellated electrode type, the direction of the electric field lines can be determined from a 3D simulation (see Figure 2-5). From this Figure, it is apparent that a pearl chain starting from the inside corner of a castellated electrode will extend along the field lines in the manner demonstrated in the experiment.

(5) Particle orbiting behavior (ACEO and ETE)

In Figure 2-8(C1, C2, D1 and D2) particles appear to be collected along the electrode edge but are not, in fact, experiencing positive DEP. Instead, they are actually in orbital movement due to ACEO (ETE is not a strong contributor here, as will be discussed later) as can be seen under the

microscope or by watching a video. Particles in these conditions do not collect in the center of the electrode because (1) there is no positive DEP to keep the particles rooted in the center and (2) the fluid vortex is relatively slow moving so that the particle orbital radius is small and localized to the electrode edge.

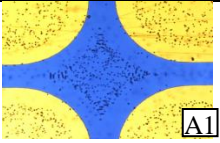
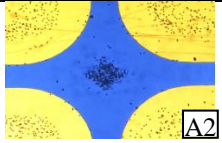
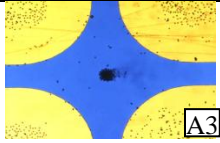
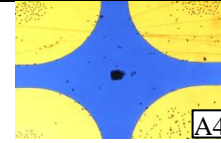
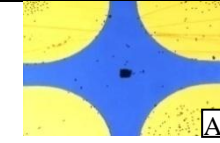
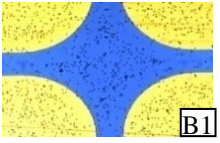
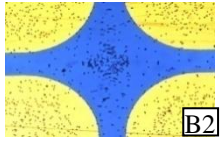
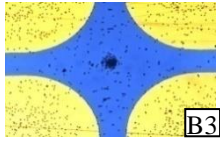
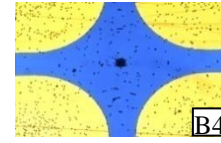
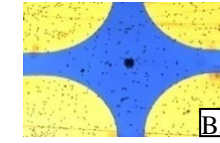
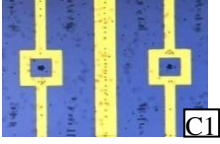
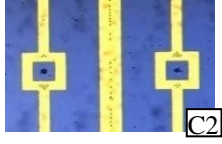
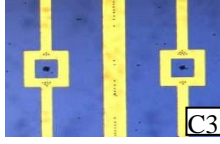
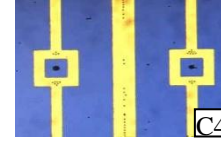
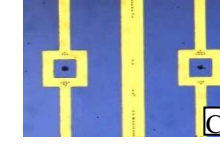

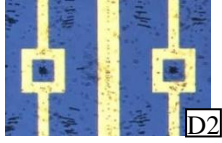
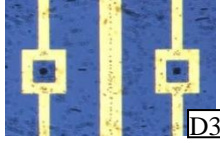
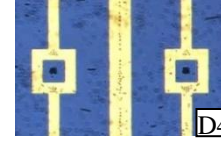
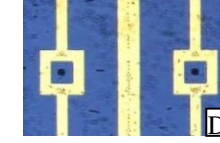
σ	Voltage				
	2V	4V	6V	8V	10V
0.0002 S/m	 A1	 A2	 A3	 A4	 A5
0.05 S/m	 B1	 B2	 B3	 B4	 B5
0.0002 S/m	 C1	 C2	 C3	 C4	 C5
0.05 S/m	 D1	 D2	 D3	 D4	 D5

Figure 2-9. Experimental results at selected voltages and solution conductivities for the quadrupole and pocket well electrodes. 2 μ m diameter polystyrene microspheres were randomly dispersed before a signal was supplied.

(6) Observations of fluorescent 200 nm particle behavior

Figure 2-10 shows the experimental results for 200 nm fluorescent polystyrene spheres with a castellated electrode. Because Brownian motion becomes much more dominant with a decrease in particle size (approximately proportional to $r^{-1/2}$), collection is much more challenging for these particles. For 2 μm particles, positive DEP collection occurs readily at 1 V. Under the same conditions, 200 nm particles show no DEP collection. When the signal amplitude is increased to 2 V, however, 200 nm particles collect readily at the electrode edges. Furthermore, the particles remain collected at the edges for the entire frequency range. As can be seen in Figure 2-2(b), the transition from positive to negative DEP occurs much later than for 2 μm particles (~ 8 MHz for 200 nm particles).

At lower frequencies and conductivities, particles are seen to be collected in the center of the electrode. Interestingly, the greatest particle collection at 1 V occurs near or below 1 kHz where there is no corresponding collection at 2 V. The greatest particle collection for 2 V instead occurs at 4 kHz, where the collection for 1 V appears to be waning. It is hypothesized that the greatest particle concentration does not necessarily occur when the ACEO velocity is maximum. An increase in ACEO velocity may, in fact, have a dispersing effect on already collected particles as they are swept up in the flow stream and are mixed with the bulk solution. This might explain how 2 V particle collection has become more effective with an increase in frequency from 1 kHz to 4 kHz – the velocity at 1 kHz may be too fast for particle collection.

For the high conductivity case, there is less apparent organized particle behavior. Clearly, at 1 V (Figure 2-10, Row C) there is no particle concentration either due to DEP or ACEO. Since the particles will not sediment except over very long time scales, and the CM factor indicates that the particles are in the negative DEP regime, this is expected. Particles may simply be levitating

above the electrodes or are slowly moving within in the fluid field which is not strong enough to cause particle concentration.

At high conductivity and 2 V, ACEO and negative DEP become more significant and particles at 1kHz and 4kHz (Figure 2-10 D1 and D2) are being concentrated at the concave corners of the electrodes synonymous to the 2 μm particle case (Figure 2-8 G2-4, H2-4). It seems that the particles become trapped in the counter vortexes generated by ACEO. The presence of negative DEP will keep particles from reaching the center of the electrode or from getting too close to the actual electrode edge.

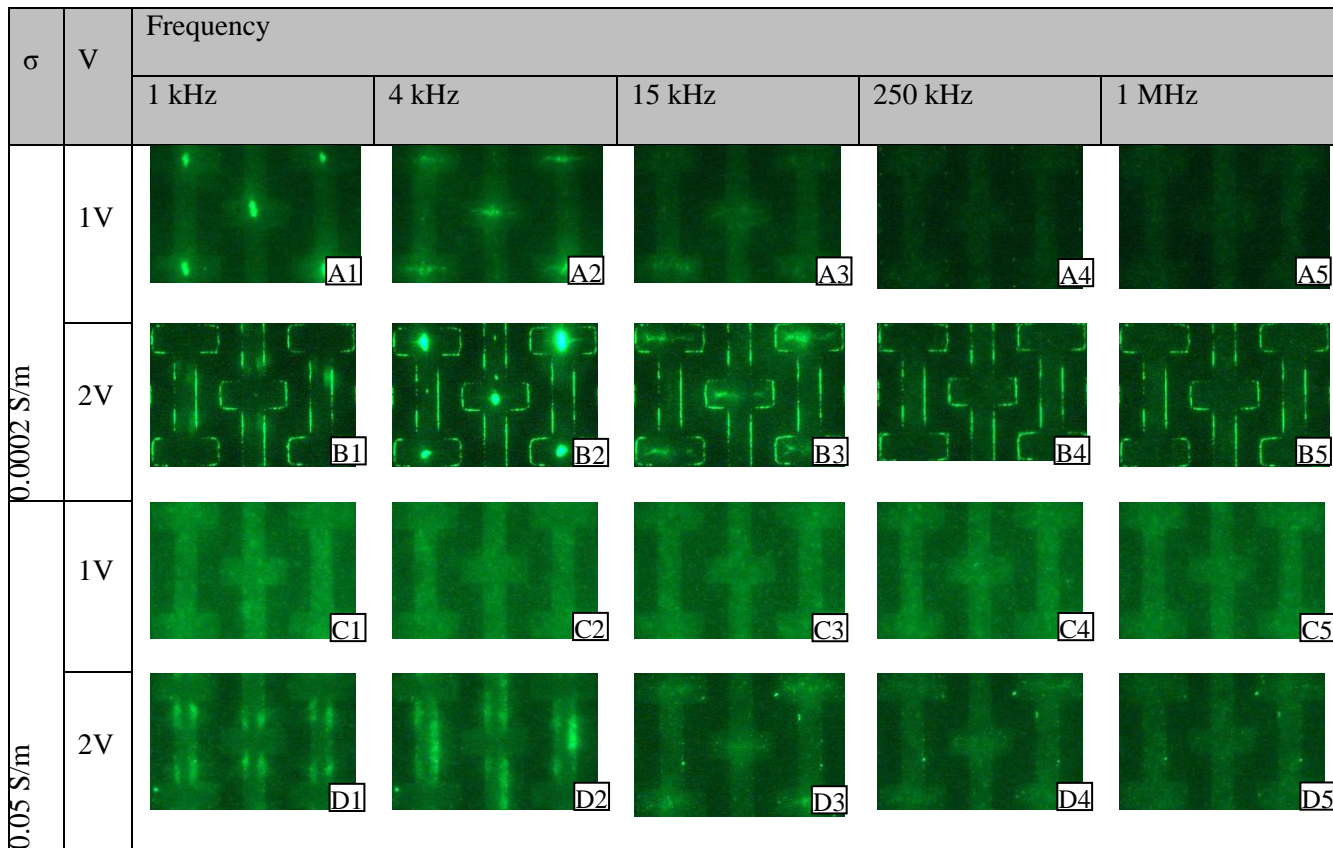


Figure 2-10. Experimental results at selected frequencies and voltages for the quadruple and pocket well electrodes using two different conductivities. 200 nm diameter polystyrene microspheres were randomly dispersed before a signal was supplied.

2.5 Finite Element Model of AC Electrokinetic Forces

2.5.1 Description of the Finite Element Simulation

The overall aim of the simulation is to predict the behavior of particles under non-uniform AC electric fields. The simulation, therefore, should be able to produce a force vector field for each given experimental condition. This is done by calculating the total force (F_{tot}) at each position as:

$$F_{tot} = F_{DEP} + F_{EHD} + F_{grav} \quad 2.12$$

where F_{DEP} is the dielectrophoretic force, F_{EHD} is the EHD force due to the combination of the ETE and ACEO, and F_{grav} is the force due to gravity. The 2D simulation study focused on parallel interdigitated electrodes. Brownian motion has been excluded from the simulations since large particle sizes ($>1 \mu\text{m}$) are assumed, which means that migration due to Brownian motion under the time scales considered is small. 200 nm particles are, in fact used in the experimental section but, like the more complicated electrode geometries, remain outside the scope of the simulation. Lastly, particle-particle interaction was not taken into account because of the extreme difficulties that it brings to the simulation. However, as will be discussed later, the particle-particle interaction does play a significant role in the particle behavior under certain conditions.

(1) Overall Simulation Process

The simulation strategy is diagrammed in Figure 2-6(c). Using COMSOL's multiphysics capabilities, three simulations were used to generate the final solution: An electrostatic simulation, a conduction heat transfer simulation and an incompressible Navier-Stokes simulation. The geometry and details of each simulation are described below.

(2) Geometry and Boundary Conditions

The 2D numerical simulation was carried out using COMSOL Multiphysics 3.3a. A 160 μm wide, 100 μm high chamber was designed with three electrodes on the bottom surface. Each electrode was 200 nm thick and 20 μm wide. The gap between each of the three electrodes was 20 μm . This geometry along with the simulation boundary conditions is shown in Figure 2-6(b). Typically, fabricated devices consist of many more electrodes. In simulating only three electrodes, there would normally be some distortion effects arising from the absence of many more electrodes on either side. A pair of boundaries has therefore been placed on either side of the center electrode to correct for this problem. These boundaries are invisible to the electric field simulation, but are symmetry walls for the heat and fluidic simulations. The application of the interior boundaries around the center electrode creates a more realistic situation for a single electrode surrounded by many more identical such electrodes.

(3) Module 1: Electrostatics Simulation

A quasi-static potential field is calculated first from the Laplace equation: $\nabla^2 V = 0$ where V is voltage. The boundary conditions are zero charge everywhere except on the electrodes, where a voltage is applied. The outside electrodes receive a $0.5 V_{\text{rms}}$ potential and the center electrode has a $-0.5 V_{\text{rms}}$ potential. The solved electric field is $\vec{E} = -\nabla V$. The maximum norm value of the electric field is 2.24×10^5 V/m at both edges of the middle electrode.

The time-averaged dielectrophoretic force is calculated according to equation (2.3) and uses the CM function for that of a sphere. The CM factor is simulated externally with Matlab using the material properties of the media and a polystyrene sphere (See Figure 2-2(a)). The imported function describes the CM factor for both media conductivities as a function of frequency.

(4) Module 2: Conduction Heat Transfer Simulation

The electric field is taken from the electrostatics simulation and is introduced as an input to the conduction heat transfer simulation to solve the Joule heating equation (2.7). The boundary conditions for the latter simulation consist of zero heat flux at the inlet and outlet, thermal insulation on the top and bottom walls (they are made of glass or PDMS and have very high thermal resistance) and isothermal electrodes. The interior walls have zero heat flux since in a system of repeating electrodes, there will be no net lateral flux. These thermal gradients then cause a hydrodynamic force which is used in the fluid dynamics simulation as described in the following section.

(5) Module 3: Incompressible Navier-Stokes Simulation

The incompressible Navier-Stokes simulation combines the effects of ETE and ACEO. The boundary conditions used for this simulation are no slip on the channel walls and zero pressure at the inlet and outlet. The interior walls have a symmetry boundary condition so that there is no normal component to the fluid flow. The final boundary condition, that of the electrodes, is a slip condition determined by the ACEO analysis.

The thin layer of liquid that experiences the ACEO force extends less than a few nanometers away from the surface [56]. Since this is much smaller than the channel height, ACEO may be modeled as a slip velocity boundary condition. To determine the velocity at the electrode, the time-averaged equation for electroosmotic velocity is used (equation (2.5)). This function is used as the slip velocity boundary condition for the surface of each electrode. Since the equation is intended to be centered on an electrode gap, it may easily be applied to a pair of electrodes. However, since three electrodes are used in this simulation, equation (5) must be used twice - once centered on the right gap and once centered on the left gap.

The ETE force is calculated using the thermal field as an input and using equation (2.10) to act as a body force for the incompressible Navier-Stokes simulation.

The drag force acting on the particle due to both EHD effects is calculated in the postprocessing mode of COMSOL. The drag force for a sphere, F_{EHD} is

$$F_{EHD} = 6\pi\eta r (\mathbf{v}_f - \mathbf{v}_p) \quad 2.13$$

where r is the radius of the particle, \mathbf{v}_f is the velocity of the fluid and \mathbf{v}_p is the velocity of the particle [54]. The force mapping that is produced from the simulation is calculated assuming that the particle is at rest ($\mathbf{v}_p=0$) and the electric field has just been applied. After the particle begins to move, \mathbf{v}_p is no longer zero and the force mapping will change due to altered drag forces acting on the particle. To elaborate, one may imagine a particle placed in a straight, fluid-filled channel experiencing laminar flow. Initially, the particle is at rest and experiences a strong drag force in the direction of the fluid velocity. Once the particle reaches the same velocity of the fluid and there is no acceleration the total net force acting on the particle will be equal to zero. In this way, the force mapping at the starting time point and at the end point is different due to the change in the particle's motion.

(6) **Total Force Calculations**

Calculating Graviational Force

The force due to gravity is calculated as:

$$F_{grav} = \frac{4}{3}\pi r^3 (\rho_p - \rho_m) \vec{g} \quad 2.14$$

where ρ_p and ρ_m are the densities of the particle and media respectively and g is the acceleration due to gravity. Since the material of the spherical particles used is polystyrene, which is denser than the media, particles under no other forces will tend to sediment.

Calculating the Total Force Acting on a Particle

Finally, the total force acting on a particle is calculated by the summation of DEP force, EHD force and gravity, and plotted in the postprocessing mode of COMSOL.

2.5.2 Discussion of the Simulation Results

(1) Isolation of the forces contributed by each AC Electrokinetic Phenomenon

Though all three AC electrokinetic forces act together on suspended particles, it is beneficial to show each force isolated so that the relative contribution of each may be understood. This has been done and is shown at 1 kHz in Figure 2-11. Note the similarity in the ACEO and ETE streamlines, which both show counter vortexes. At the frequency shown, all counter vortex patterns rotate in the same direction – counter-clockwise on the left and clockwise on the right. Note the difference in the location of the vortex node, which is different for each phenomenon. Even within the same phenomenon, the position will change with frequency, conductivity and voltage. The DEP forces for low and high conductivity look identical but the direction of the force towards the electrode edge in the former and away from the electrode edge in the latter. A look at the CM factor (Figure 2-2 (a)) will show that such a change in conductivity will cause a transition from positive DEP to negative DEP. The strength of the DEP force is also affected by this change in conductivity but is of the same order of magnitude and so is difficult to distinguish in the logarithmic color scale. A detailed analysis of the effects of several important experimental variables will be discussed in the following sections.

(2) Total force exerted on particles and comparison with experimental results

The total force mapping for several frequency and conductivity settings is shown in

Figure 2-12. Images from the experiments at the corresponding conditions are overlaid to show qualitative experimental agreement.

Figure 2-12(a) and (d), which show 1 kHz for low and high conductivity respectively both show counter vortex patterns. The major difference between the two is the contribution due to ACEO, which has been decreased and the contribution of DEP, which causes particles to be trapped in

the center in the case of positive DEP (a) or caught in the vortex pattern above the electrode edges in the case of negative DEP (d). In

Figure 2-12(b), the transition has been made from ACEO dominated particle motion to positive DEP dominated particle motion. The experimental image for this setting shows particles trapped on the edge of the electrode as the simulation predicts.

Figure 2-12(e) shows a transition period between ACEO motion and negative DEP. At this frequency, particles may be trapped in the vortex but may also become subjected to other forces such as particle-particle interaction. This is the case shown in the overlaid experimental image where many particles are at the edge of the electrode and form the base for particle chains.

Finally, in (c) and (f), the high frequency brings the force plot into the negative DEP-dominated range. Unlike in

Figure 2-12(b), the DEP force opposes that of gravity and overcomes that force until a certain height is reached where a balance between the two forces exists (indicated in the Figure as the *levitation point*). Particles above this point will fall to this position and those below will be pushed upwards. This is seen experimentally as particles are forced away from the electrode edge and rapidly rise above the focal plane of the microscope. In a still frame image, this action results in out-of-focus particles near the electrode, as shown by the overlaid images for those conditions.

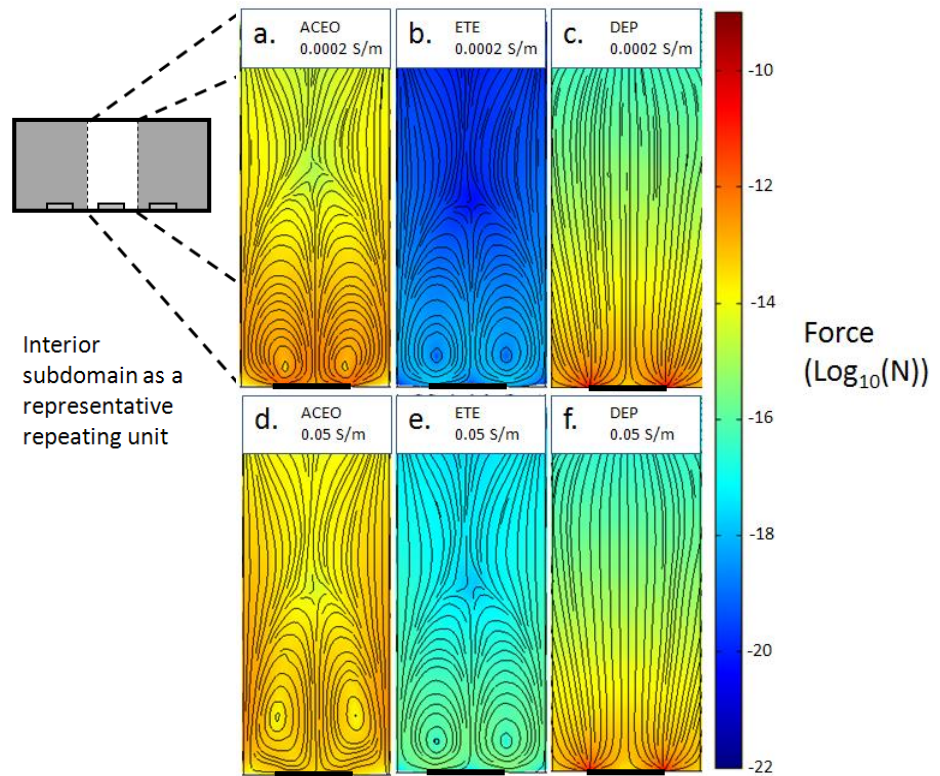


Figure 2-11. Mapping of each force isolated from the others at 1 kHz. The surface plot uses a logarithmic scale with force streamlines.

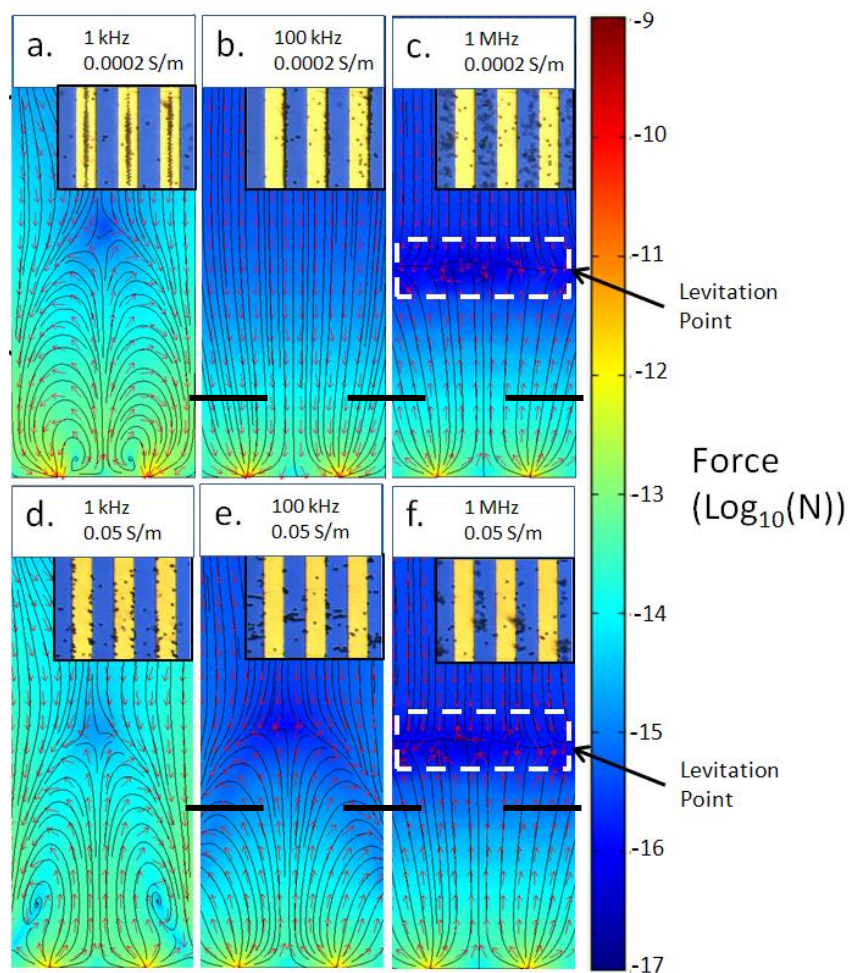


Figure 2-12. Total force simulation results. Each surface plot represents the log of the force acting on a $2\ \mu\text{m}$ particle at rest. Force streamlines are shown as well as normalized arrows which show the direction of the force at each location. Corresponding experimental results are showed inlaid on each simulation plot.

(3) Analysis of the effects of operational and system parameters

3 Effect of Distance from the Electrode

The relationship between the magnitude of each force and distance to the electrode is shown in Figure 2-13. With DEP, the force is known to die off exponentially with distance from the electrode. However, AC-EO and ETE forces are hydrodynamic and will depend on the properties of the liquid as well as the geometry of the chamber. Furthermore, since these phenomena generate non-trivial flow patterns which are spatially dependant in x and y positions (z as well for more complicated geometry electrodes) the force distance relationship is most easily shown graphically. In order to remove the dependence on the x coordinate, the average force for each distance above the center electrode is computed.

The DEP force does not vary greatly with frequency except during the transition between positive and negative DEP. This transition starts around 100 kHz, crosses zero at ~300 kHz and reaches a steady negative value near 1MHz (see Figure 2-2(a)). The frequencies shown in Figure 2-13 are outside the transition phase, and therefore look identical in all images. Note that the hydrodynamic forces are much more penetrating than the DEP forces which die off far more rapidly with distance.

4 Effect of Changing the Frequency of the Excitation Signal

The ascendance and subsidence of different phenomena as the frequency of the applied signal changes are one of the most important and compelling aspects of AC electrokinetics. This relationship was investigated and is shown in Figure 2-14, which shows the relationship between force and frequency for several different heights above the electrode and for two conductivities.

One important feature shown in the Figure is the way in which conductivity affects the hydrodynamic and DEP forces. Since the hydrodynamic forces are predominantly caused by

ACEO (rather than ETE) at these conductivities and voltages, increasing the conductivity will result in a frequency shift in the peak hydrodynamic force. In ETE dominated conditions, an increase in conductivity will result in an increase in hydrodynamic force and the dependence on frequency is much less exaggerated.

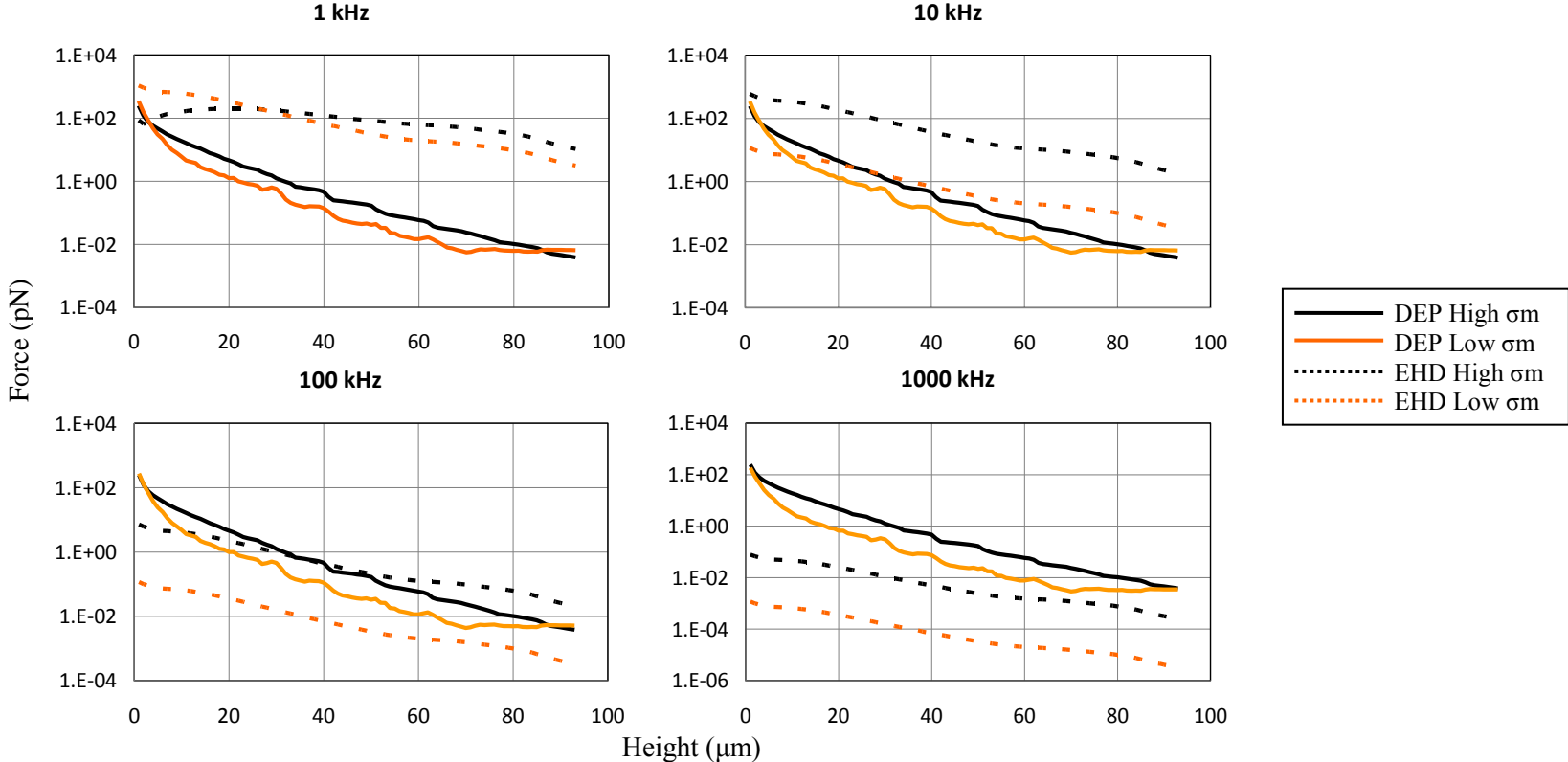


Figure 2-13. Relationship between the strength of each phenomena and the height of the center electrode is shown for several frequencies and conductivities. Since the force varies as a function of x as well, an average was taken across all x for each given y point so that only general relationships can be understood.

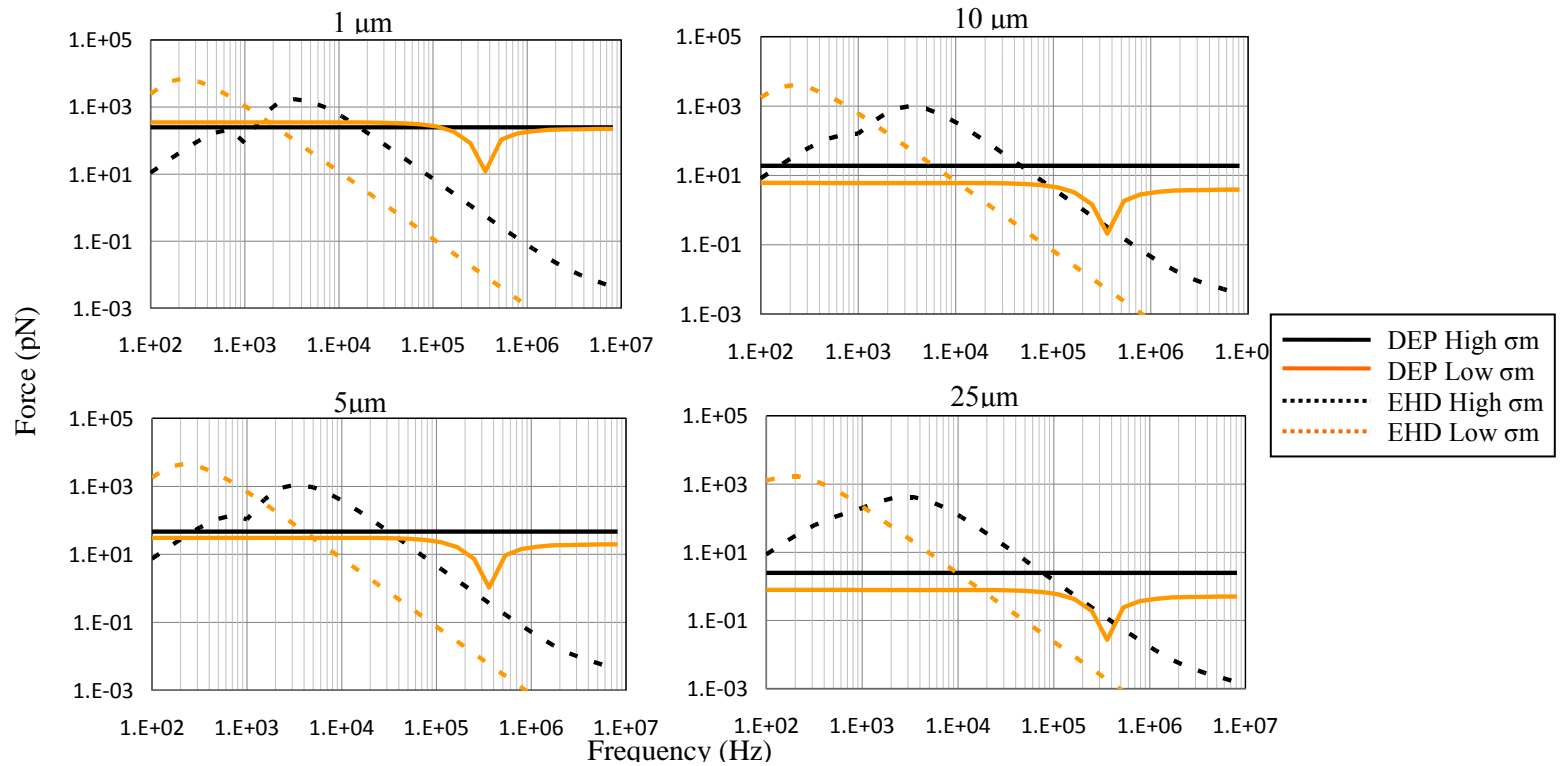


Figure 2-14. The magnitude of each force is shown as a function of frequency for four distances (displayed on each graph) above the electrode surface. As before, in order to eliminate special variations, the x component is averaged across the entire electrode so that only general relationships can be understood and exact spatial values cannot be obtained.

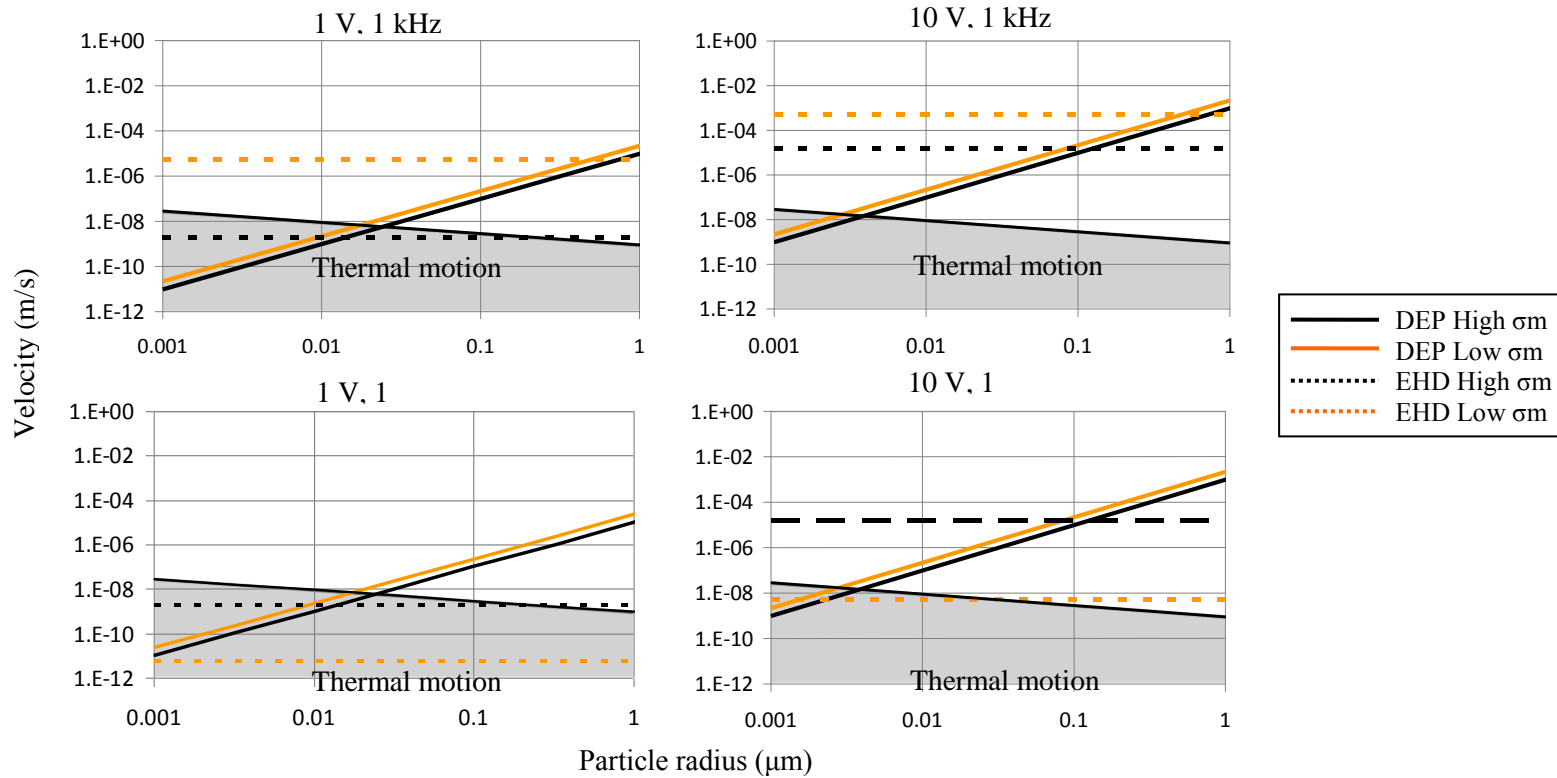


Figure 2-15. The magnitude of velocity for particles experiencing DEP and Drag is shown as a function of particle radius for four frequency and voltage settings (displayed on each graph). The force is averaged (as before) for all x , $1\mu\text{m}$ above the electrode surface. It must be stressed that only general relationships can be learned from such analysis. Velocity caused by DEP was found by equating drag force and DEP force and

solving for velocity. The region in grey shows the area where deterministic particle organization by AC electrokinetics is overcome by thermal motion.

The transition point between positive DEP and negative DEP at low conductivities can be clearly seen in the Figure. DEP, which remains at a constant value for most frequencies undergoes a transition and reaches a minimum magnitude at ~300kHz (at which the actual value changes from positive to negative). At high conductivities, only negative DEP is present and does not undergo a transition.

5 Effect of Changing the Particle Radius

A reduction in particle radius greatly increases the difficulty of manipulation due to an increase in the randomization effects of thermal motion. Reliable manipulation of submicron particles requires careful device design and control of environmental conditions as well as a valid method for predicting behavior. Figure 2-15 shows the relationship between particle velocity and radius and considers several voltage and frequency settings for two conductivities. The values in the y-axis indicate instantaneous velocity one micron off the surface of the electrode, since the forces acting on particles are highly spatially dependant. This analysis also assumes that DEP force is in constant equilibrium with drag forces (a valid assumption since initial acceleration of such small particles will be quite large - hundreds to thousands of m/s²). The instantaneous velocity of the particles due solely to DEP can therefore be estimated by balancing drag force with DEP force and solving for v :

$$v = \frac{r^2 \epsilon_m \text{Re}[CM] \cdot \nabla |E_{rms}|^2}{3\eta} \quad 2-15$$

It is also important to note that even though the conductivity and frequency have little effect on the magnitude of the DEP (except during the transition from positive to negative DEP), the direction can change according to the CM factor as mentioned previously.

An inspection of Figure 2-15 shows that at low conductivity (shown in grey), an increase in voltage does not greatly change the point at which DEP force overcomes the EHD force. This

is because at this conductivity, ACEO is the predominant EHD force and both DEP and ACEO forces have the same relationship with amplitude of the applied signal (proportional to V^2). In fact, the relationship between DEP and ACEO can change slightly since the fluid pattern caused by ACEO is not perfectly constant with voltage. At higher conductivities, however, the balance of forces can change since ETE, which is proportional to V^4 , becomes more important to the hydrodynamic force.

6 Effect of Changing the Media Conductivity

Media Conductivity plays an important role in all three of the AC electrokinetic forces (as can be seen in each of the equations describing them) and its effects may be seen in all three of the Figures (2-13, 2-14 and 2-15) previously mentioned. Since the Figures display the magnitude of the force, and not its direction, it is difficult to be understood from these Figures alone. A much better understanding can be gained from CM (Figure 2-2) and Π (Figure 2-4) Figures. For low frequencies, an increase in conductivity will change the direction of DEP force. Like DEP, the direction of the ETE force can be switched by changing the conductivity. Also, an increase in conductivity will increase the magnitude of ETE force but this is also not clear from the Figures since the conductivity and voltage ranges used in the simulations cause ACEO to be predominant. The effects of the conductivity change on ACEO is most dramatically seen in Figure 2-14. The low conductivity EHD force has a peak around 200 Hz. The higher conductivity peak is around 3 kHz and has a lower peak magnitude.

7 Effect of the AC Signal Amplitude

The relationship between the force of each phenomena and amplitude of applied signal is straightforward. DEP and ACEO are increased according to the square of amplitude (equations 3 and 5) and ETE according to amplitude to the fourth power (equation 10 – note that both E^2 and gradient of T depend on voltage). Figure 2-15 shows some of the ramifications of the fourth

power dependence on conductivity for ETE. For both frequency cases at low conductivity, an increase in voltage does not significantly change the point at which DEP overcomes the EHD force and the DEP force. This is because ACEO is the dominant EHD force at low conductivity and both ACEO and DEP have a similar amplitude relationship. At high conductivity, this changes due to the increased influence of ETE. An increase of the voltage by 10 times has increased the ETE force by ~4 orders of magnitude and has increased its relative importance compared to the other two forces. For example, at 50 nm particles at high conductivity are predominantly under the influence of DEP at 1 V but at 10 V, EHD flow predominates.

2.6 Conclusions

A new method for simulating the three major AC electrokinetic forces has been demonstrated and this numerical simulation shows good qualitative agreement with the experimental part. The wide range of additional experiments using varied device designs and operational conditions along with this simulation should provide scientists and engineers with an invaluable tool for future lab-on-a-chip designs.

Future improvements to the numerical simulation will include incorporation of particle-particle interactions as well as making the ACEO boundary conditions more generic so as to apply to more complicated electrode geometries.

This, and future numerical simulations will continue to play a critical role in the design of AC electrokinetic components of lab-on-a-chip devices. Specifically, this simulation will be used to improve micro-mixer, particle separation and cell manipulation devices in the authors' laboratory.

CHAPTER 3: ENHANCEMENT OF HETEROGENEOUS IMMUNOASSAYS USING AC ELECTROOSMOSIS

3.1 Problem Statement

Surface-based assays often sufferer from long incubation times due to mass-transport limitations. Essentially the large analyte molecules common to many biological tests react quickly with the surface receptors but diffuse slowly, causing the overall reaction to become bottlenecked by transport of new reagents to the surface. This is a critical barrier that must be overcome to enable the translation of many microfluidics and biosensors technologies. The approach to solving this problem was to use AC electroosmosis as a means of stirring the reaction volume, thereby reducing the transport limitations. First finite element simulations were employed to model the binding kinetics under AC electroosmotic flow. Second, fluorescent immunoassays were employed to explore the effect of parameters and to demonstrate proof of concept. Both steps were used to determine effective conditions for to produce binding enhancement.

3.2 Introduction to the use of ACEO to alleviate transport limitations

The current trend towards assay miniaturization on microfluidic devices creates unique challenges for rapid detection of biomolecules. Specifically, detection times for heterogeneous immunoassays can be inordinately long (several hours [3, 81-82]) because of the time it takes for analytes to travel to the device surface or transducer, where they then must bind or react with surface-bound receptors. This detection time limitation is a critical barrier that needs to be overcome for a wide variety of important biosensor applications, such as rapid bedside diagnostics, environmental testing, counterterrorism, etc...[83-86] Common conditions such as low diffusion coefficients and fast surface reactions cause the system to be mass-transport limited

(the reaction rate is much faster than the transport of reactants to the surface) [87-88]. In order to alleviate this condition, AC electroosmosis (ACEO) as a method for creating advective mixing is investigated. ACEO is commonly generated using simple planar interdigitated electrodes (IDEs). The fluid motion caused by such devices is the result of movement of induced charges at the surface of the electrodes and creates a rotational velocity pattern that can be envisioned as a set of vortices that exist on either side of each electrode finger. These flow patterns will bring reactants to the surface, thus helping to overcome the slow diffusional transport that would otherwise dominate.

The very low Reynolds numbers in microscale flows prevent turbulent mixing and designs typically utilize channel flow to improve mass transport instead [89]. In this case, the reaction rate can be improved, but at the cost of much larger sample volumes and through the use of bulky pumping equipment or high voltage power supplies. By contrast, ACEO can be generated using simple planar microelectrodes with low voltage and power requirements and can be microfabricated cheaply with established techniques.

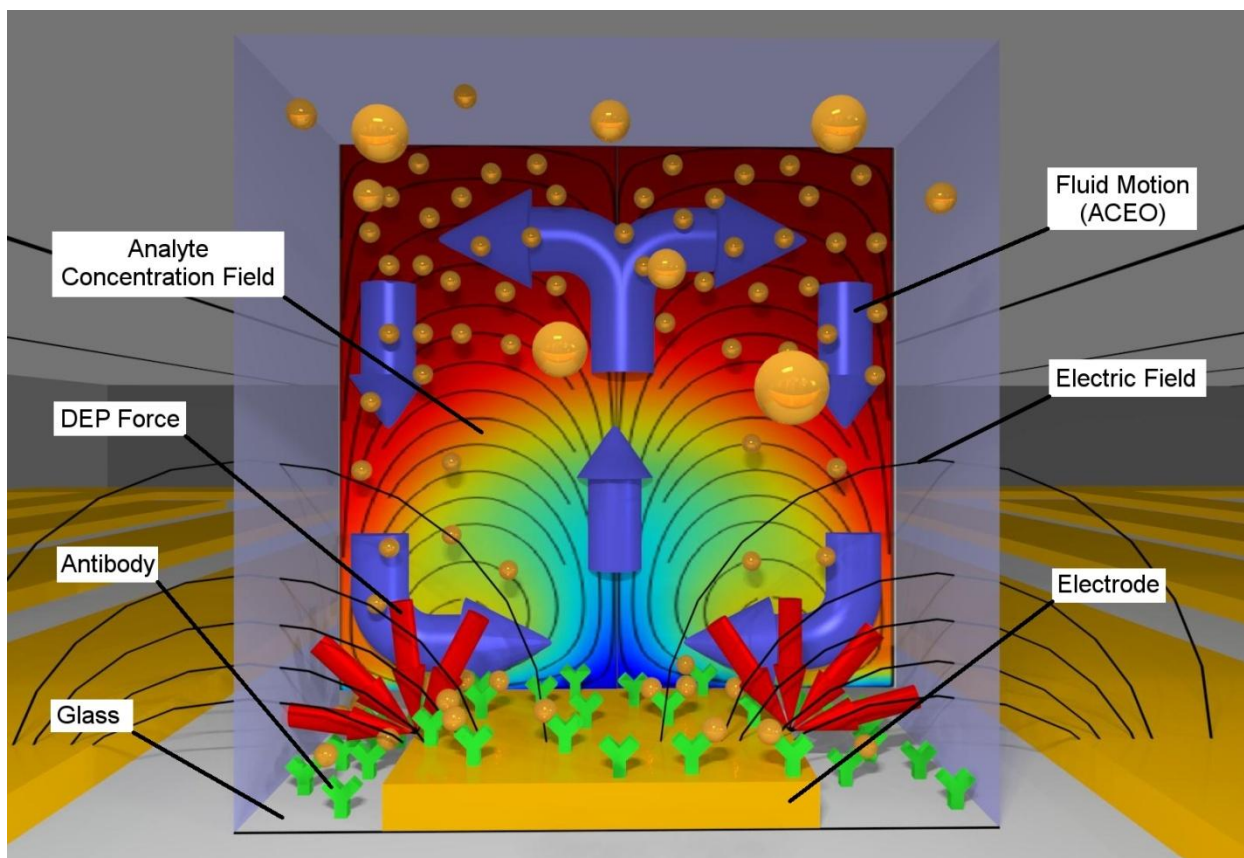


Figure 3-1: Diagram of an immunoassay performed with AC electrokinetic enhancement on a microelectrode. The concentration is indicated both by the antigen particles (orange) and the concentration field (red: high concentration, blue: low concentration). The fluid motion caused by ACEO is shown as blue arrows as well as the streamlines in the concentration field image. Red arrows indicate the force due to DEP and the antibodies are bound both on the surface of the electrode as well as on the glass substrate.

ACEO is one of three AC electrokinetic phenomena. The other two are the electrothermal effect (ETE) and dielectrophoresis (DEP). Like ACEO, ETE is a hydrodynamic force. ACEO arises from the movement of induced charges in the double layer on the electrode surface, whereas ETE

arises from the movement of induced charges generated from Joule heating within the bulk of the solution. Both ETE and ACEO can generate rotational velocity patterns near the electrodes (Figure 3-1). In general, ETE dominates in higher conductivity solutions and at higher electrical frequencies (typically > 1 mS/cm and around 100 kHz) [70] while ACEO exists at lower frequencies and conductivities (typically < 10 μ S/cm and less than 10 kHz [53]). The capability for ETE to improve heterogeneous assays by stirring has been investigated already [70, 90]. Though ETE can operate in physiologically relevant fluids, voltages of an order of magnitude larger are typically required in order to attain useful ETE velocities. The other AC electrokinetic force, DEP is caused by a difference in polarizability between a particle and the medium in which it is suspended. In a non-uniform AC field, this difference results in a force on the particle which causes it to move either towards high electric field strength (positive DEP – shown in Figure 3-1) or towards low electric field strength (negative DEP – not shown). DEP is often used to manipulate particles larger than several hundred nanometers but is not generally used for molecules. When particles are of molecular length scales the DEP force becomes non-deterministic due to the dominance of thermal randomization [66, 91]. Though DEP has not yet been applied to improving molecule detection, it has been shown to improve particle detection [8, 92].

In this article, the use of AC electroosmosis to improve the rate of antibody binding to a sensor surface was investigated using finite element modeling and fluorescent immunoassays. The aim of this paper is to understand how the geometry of the electrodes and fluidic channel affect assay improvement, what optimum voltage and frequency to use, what types of reactions will benefit from the use of ACEO and finally to show proof of concept by performing fluorescent immunoassays. These assays will also demonstrate the feasibility of applying these techniques to relevant biological tests performed on biosensors. As is the case with many sensor systems, the

more rapid and sensitive the technology is, the more applications become available. Currently there are no widely used immunosensors in diagnostics or clinical research. This study is targeted to help translate these technologies.

3.2.1 AC Electroosmosis overview

ACEO is caused by an interaction between a non-uniform electric field and the electric double layer that is induced at the surface of a submerged electrode. This electric double layer consists of counter ions that accumulate near the surface of the polarized electrode. The free charges in the double layer experience a lateral coulomb force due to the electric field and translate across the electrode surface. The mass movement of these charges drags the fluid from the edge of the electrode towards the center. This driving force, which exists only very near the surface (a few nanometers) [93], is transferred to the bulk solution through viscous drag ultimately forming a rotational fluid pattern (Figure 3-1). A more detailed description of ACEO, including equations describing the fluid motion near the electrode surface are described in an section 2.3.2 on page 57.

3.2.2 Description of an Immunoassay Surface Reaction

Immunoassays were performed in order to provide empirical validation of simulation results and as a way of observing the pattern of antibody binding on interdigitated electrodes. Immunoassays are ubiquitous and rely on the excellent specificity of antibody-antigen reactions to capture target proteins (also viruses, bacteria, etc.). They are currently a mainstay of medical diagnostics and clinical research. Heterogeneous immunoassays consist of a surface-based attachment between an antibody and an antigen. Either species may be first immobilized on the solid phase while the other is contained in the sample volume and allowed to react with the surface. The use of a tracer, which may be radioactive or fluorescent, is required to generate the signal. In biosensor

applications, the tracer is usually eliminated and the presence of analyte is detected through mass, optical, electrical or other physical change on the surface of the transducer.

The chemical reaction that describes a surface binding event is as follows:



where c is concentration of the species, θ is concentration of binding sites at the surface, c_s is concentration of bound species at the surface, k_{ads} is the forward binding constant and k_{des} is the reverse constant. The rate of change of the bound species at the surface, including surface diffusivity is [10]:

$$\frac{\partial c_s}{\partial t} + \nabla \cdot (-D_s \nabla c_s) = k_{ads}c\theta - k_{des}c_s \quad 3.2$$

The concentration of remaining binding sites, θ , can also be described as the difference between the total number of binding θ_0 sites and the occupied sites c_s . This equation can therefore be expressed as follows:

$$\frac{\partial c_s}{\partial t} + \nabla \cdot (-D_s \nabla c_s) = k_{ads}c(\theta_0 - c_s) - k_{des}c_s \quad 3.3$$

Since this reaction removes species from the bulk solution near the surface, concentration gradients will form and, in a flow field, interact with fluid flow. This makes the determination of c nontrivial and requires concurrent solving of the mass transport and flow fields in the bulk solution.

One way to estimate whether or not a reaction is transport limited or reaction-rate limited is to calculate the Damkohler number (Da). This is a ratio of the reaction velocity ($k_{ads}\theta_0$) to the rate of transport (D/h) where h is chamber height (Figure 3-2). $Da \gg 1$ indicates a transport limited

system while $Da \ll 1$ indicates a reaction-rate limited system. A range of chemical reactions with varying transport-limited Da numbers was employed for the numerical simulations. If the analyte is a large molecule, a protein for example, Da will usually be high due to its small diffusion coefficient, especially if the reaction at the surface is a simple, rapid binding event.

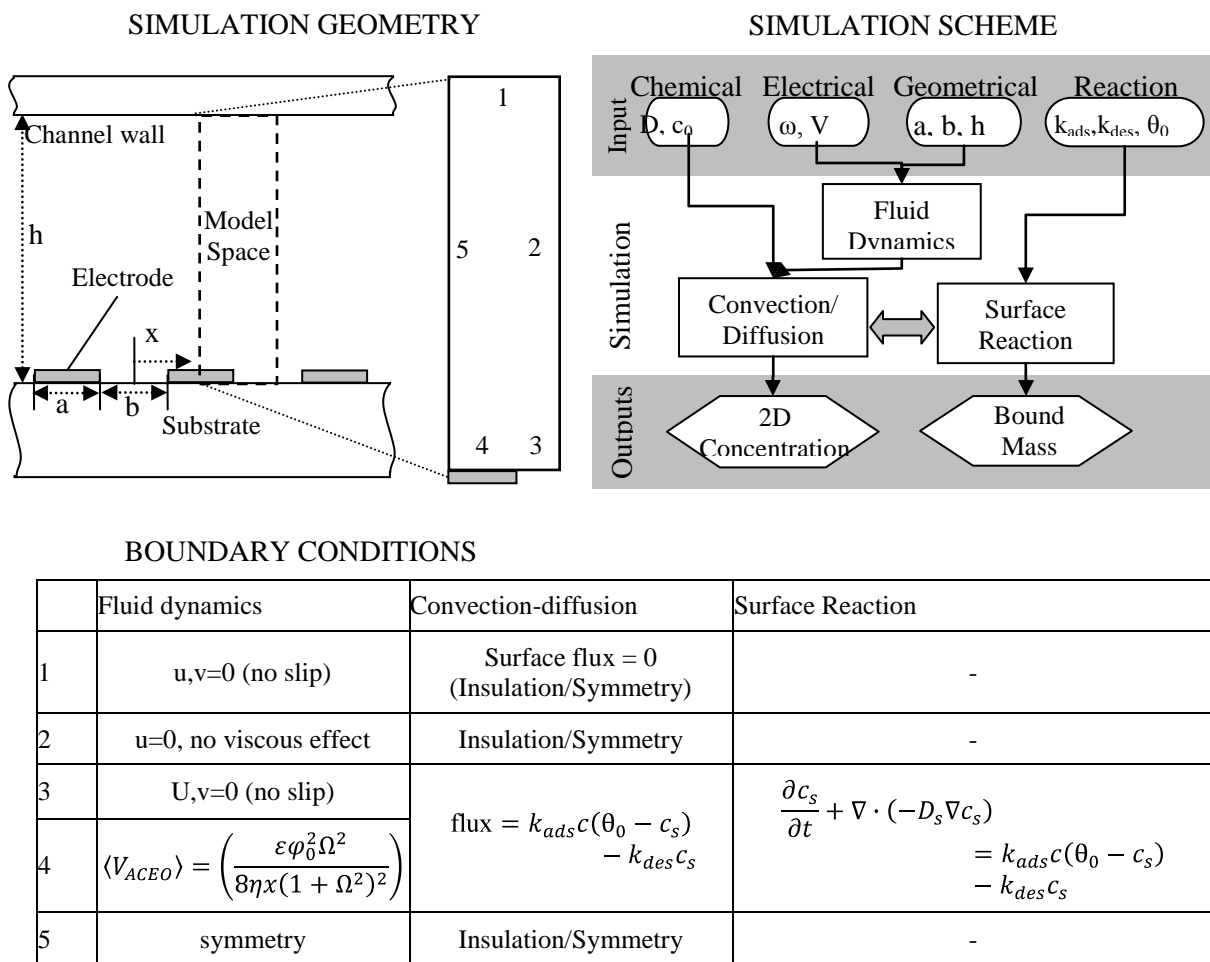


Figure 3-2: Top Left and Bottom: Simulation geometry and boundary conditions. The numerical simulation consists of a cross-section of an interdigitated electrode placed on one side of a microfluidic chamber. The model takes advantage of symmetry and repeating units and only

considers one half of an electrode and gap. h , a and b are the channel height, electrode width and gap width respectively. x is the cross-sectional position starting from the center of the electrode gap. Boundaries are numbered and explained in the table to the right. Note that the reaction occurs only on the bottom surface (3 and 4). The reaction simulation is therefore inactive on all other boundaries. Equation details are described in section 2.3 on page 52. Top Right: Flow chart describing simulation scheme. The input parameters shown are important but not a complete set. For example, viscosity and density of the fluid are inputs for the fluid dynamics simulation but not shown in the diagram.

3.3 Finite Element Simulation of an Immunoassay in the Presence of AC Electroosmosis

3.3.1 Description of the Finite Element Simulation

The numerical simulation describes the behavior of a parallel interdigitated electrode (IDE) placed at the bottom of a microchannel. The model assumes a location in the center of the IDE which is free of edge effects. Furthermore, since the fluid behavior is the same along the length of an electrode, a 2D simulation is sufficient. (IDEs used in the experimental section consist of 40 to 200 fingers, each 1 cm long.) As the structure consists of repeating units of electrodes with each unit behaving identically, it was only necessary to model a single electrode. Moreover, the simulation can take advantage of the symmetry of each electrode finger and the generated fluid pattern. A schematic of the simulation geometry and boundary conditions is shown in Figure 3-2(top left).

The overall model consists of three linked simulations, which are diagrammed in Figure 3-2(top right). (1) A steady-state fluid dynamics simulation generates a fluid field produced by ACEO.

Parameters for this simulation include (among others) the geometry of the electrode and chamber, the frequency and voltage of the excitation signal and viscosity and density of the fluid. Next, the fluid velocity field is used by a pair of coupled time dependant simulations – (2) a convection and diffusion simulation and (3) a surface reaction simulation. These two simulations are coupled since mass is removed from the 2D space and deposited on the boundary where the reaction takes place. The rate of reaction will depend on the concentration near the boundary as well as the amount of material already bound. These simulations depend on the concentration and diffusion coefficient of the free analyte as well as certain properties of the chemical reaction (rate constants and density of surface binding sites). The result of these three coupled simulations consists of concentration maps for the time span used as well as a record of the bound material over time. These simulations were all carried out using COMSOL MULTIPHYSICS™ version 3.5a finite element software with Matlab support.

(1) Fluid dynamics simulation

The 2D fluid dynamics simulation uses the Navier-Stokes equations for an incompressible Newtonian fluid. The temperature of the liquid is assumed to be constant because the expected Joule heating will be insignificant due to the low solution conductivity ($2 \mu\text{S}/\text{cm}$) and the voltages applied will be low [26]. Steady state is achieved in an insignificant time (less than a second) compared to the time scales of the binding reaction (minutes or hours)[94]. Furthermore, the fluid behavior is the same along the length of the electrode, except near the end of the electrode finger. The Reynolds numbers are well below 0.1, allowing for a laminar flow assumption as well.

The two equations governing fluid flow are the mass conservation equation

$$\nabla \cdot U = 0$$

where U is the velocity vector, and the Navier-Stokes equation,

$$\rho U \cdot \nabla U = -\nabla P + \mu \nabla^2 U \quad 3.5$$

where ρ is the fluid density, P is the pressure, and μ is the dynamic viscosity. Boundary conditions (Figure 3-2) are as follows. A no slip boundary condition exists on the top chamber wall and the glass portion of the chamber bottom. Symmetry boundary conditions are placed on the two side walls. The electrode generates the fluid motion as a boundary condition according to the ACEO equations described in section 2.3.2 on page 57.

(2) Convection-diffusion simulation

At the start of the simulation, the analyte is evenly distributed within the bulk solution and the surface receptors are completely free of bound material. As the time increases, the reaction at the surface removes material from the solution till equilibrium between the two domains is reached. The movement of mass within the defined geometry is governed by the convection-diffusion equation:

$$\frac{\partial c}{\partial t} + \nabla \cdot (-D \nabla c + c \mathbf{u}) = 0 \quad 3.6$$

where c is concentration, t is time, D is the diffusion coefficient and \mathbf{u} is the fluid velocity vector.

Boundary conditions (Figure 3-2) consist of insulation on all boundaries except the bottom surface where mass is removed from the subdomain according to the following: $flux =$

$$k_{ads}c(\theta_0 - c_s) - k_{des}c_s.$$

(3) Surface reaction simulation

Since there is a balance between the bound surface material and the material contained within the bulk solution, the convection-diffusion simulation must be coupled to the surface reaction simulation. COMSOL's weak boundary form [COMSOL 95], which provides the ability to

implement PDEs on a boundary and couple them to the physics in other simulations is needed in order to model the reactive boundary. This both allows for the tracking of bound material and provides for a means of simulating surface diffusion. The condition at the surface is a PDE (Equation [3.3]) which describes the accumulation of mass from the solution as well as surface diffusion along the boundary.

3.3.2 Simulation results

For a given parameter set (geometry, electrical, chemical...) the simulation produces a series of time-dependent concentration maps. An example of concentration maps produced by the simulation can be seen in Figure 3-3.

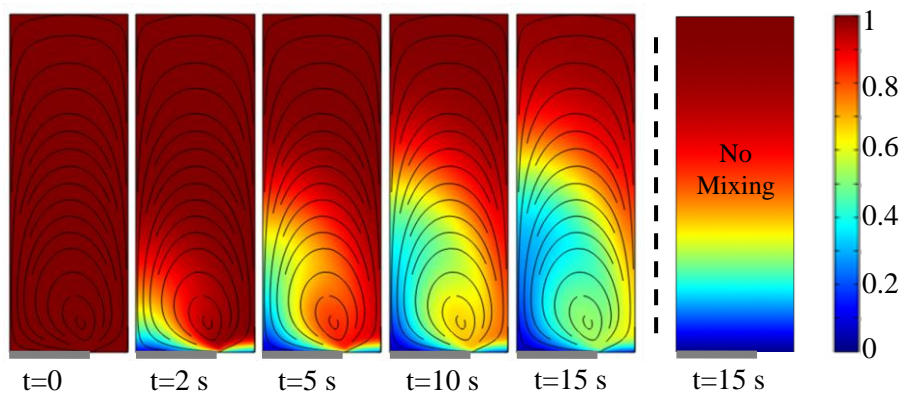


Figure 3-3: Concentration maps of a 100 μm wide electrode and 30 μm wide gap operating at 2 V_{pp} . The scale shows the relative concentration c/c_0 . Electrode position is indicated by the gray line under each map. Flow across the surface of this half of the electrode will be from right to left. The last concentration map is for an inactive electrode.

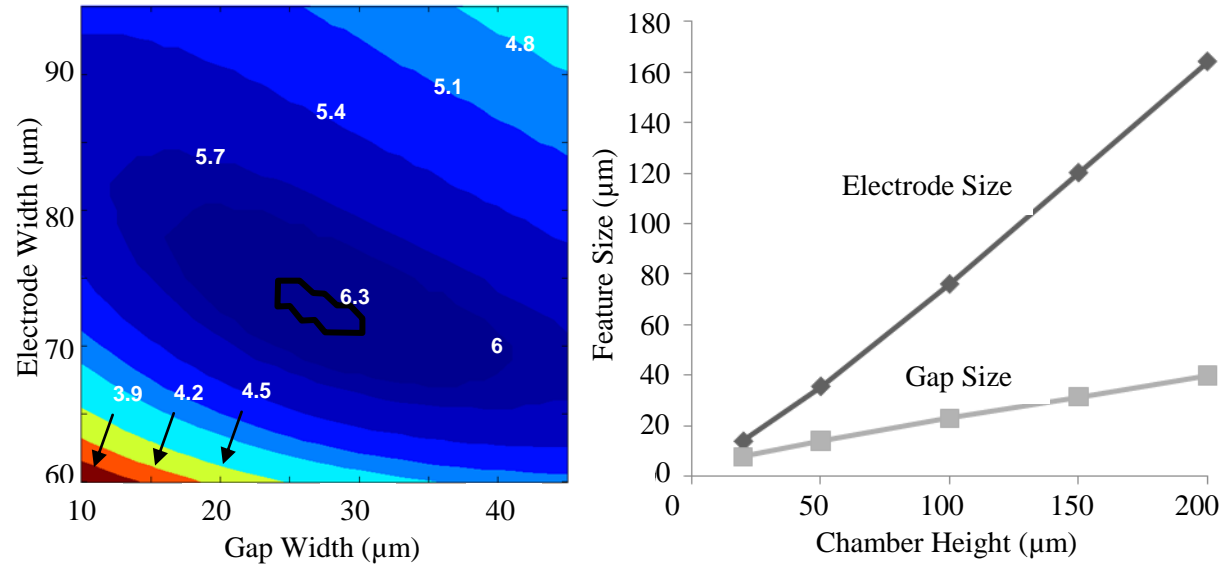


Figure 3-4: Geometry optimization. Left: Contour plot showing the improvement factor as a function of electrode and gap widths for a 100 μm chamber height. Right: Optimum geometry as a function of chamber height. For each chamber height, the ideal geometry was determined by finding the shortest time to reach equilibrium. Voltage was adjusted for each geometry so that the maximum electric field was the same regardless of the gap width.

(1) Optimization of electrode geometry and excitation frequency

Electrode geometry and excitation frequency will both affect fluid velocity and binding rates. To find the most efficient electrode geometry a range of electrode sizes and gap sizes were tested for several chamber heights. For each chamber height, electrode width, a , and gap width, b , (Figure 3-2 (top left) were varied within 1% to 200% of the channel height. An initial scan of these geometries was performed with 5% increments followed by a finer scan at 1% increments near the optimum region. These simulations used 100 kV/m maximum electric field (voltage was made proportionate to the gap size – for example, an electrode with a 20 μm gap would receive a $2 V_{pp}$ signal). An improvement factor was calculated by dividing the time to reach equilibrium in the unmixed case ($t_{eq-unmixed}$) by the time for the mixed case ($t_{eq-mixed}$). Equilibrium was considered to be achieved when the adsorption rate was a factor of a thousand less than the initial rate. Figure 3-4(left) shows a surface map of the improvement factors for a fine pass using a 100 μm chamber height. The dimensions that produced the lowest time for each chamber height were selected and plotted in Figure 3-4(right).

Simulations to determine the optimum frequency were performed as well by varying frequency (from 40 Hz to 1 MHz) on the ideal electrode geometry. It was observed that the optimum frequency was independent of the electrode size. The optimum electrode width and gap distance is $\sim 70\%$ and $\sim 30\%$ of the chamber height respectively. The reason for this optimum is likely a balance between two geometrically dependant properties. Decreasing both the electrode and gap size too far contains the vortex within a narrow geometry and consequently causes most of the flow velocity to be constrained to a shallow depth. Increasing the electrode too far decreases the efficiency as well. The highest fluid velocity occurs at the electrode edge and decreases towards the electrode center. Electrodes that are too wide will therefore cause slower overall fluid

velocities. A balance, therefore, of electrode size and gap size with the chamber height will cause the most efficient mixing.

Optimum frequencies are in the kHz or lower range, with the best time near 100-200 Hz. (The binding time, as a function of frequency, is shown in Figure 3-5(left) for a 100 μm chamber height.) This corresponds to the range of highest generated velocity. The lowest frequency simulated was 40 Hz, which is slightly below what is safe to use in the lab due to hydrolysis and electrode damage. This prediction was corroborated by fluorescent assays and will be discussed below.

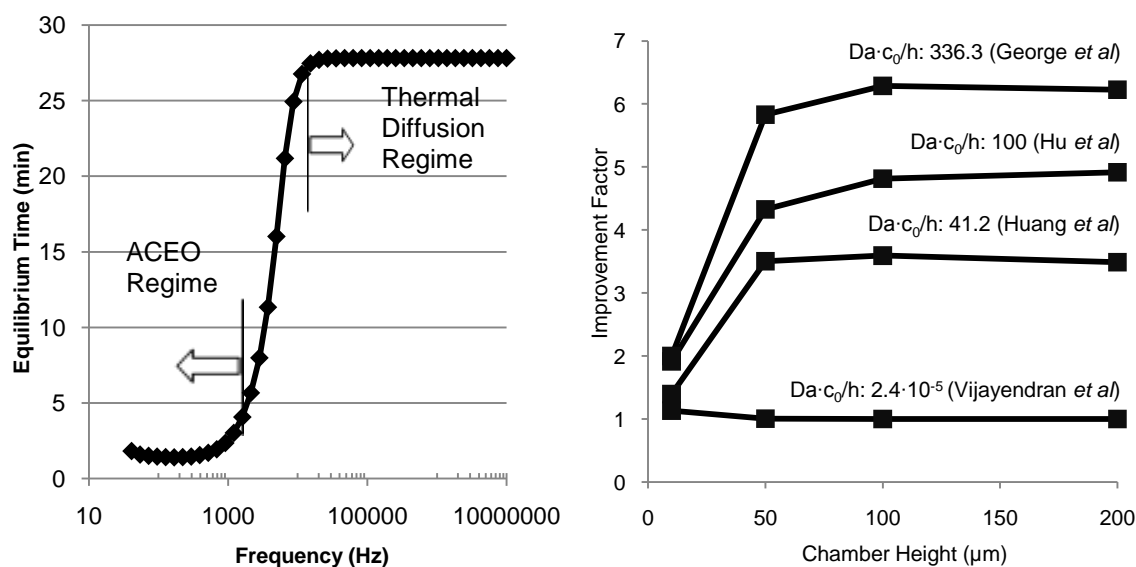


Figure 3-5: Left: Equilibrium binding time as a function of frequency for a 100 μm chamber height using a 70 μm electrode width and a 30 μm gap width. The electric field was 100 kV/m. Highest velocities are near the 100 Hz range with the phenomena dying out in the kHz range. After 10 kHz, binding time is purely determined by diffusion. Right: Assay enhancement for four

different sets of reaction constants. Improvement factors are calculated by comparing the equilibrium times for mixed and unmixed samples with a maximum electric field of 100 kV/m. For each chamber height, ideal electrode geometry (as shown in Figure 3) was used. An improvement factor of 1 means no improvement.

(2) Improvement for different types of assay chemistries

In order to determine how much improvement can be gained from using ACEO mixing, four different reaction chemistries were simulated, representing a range of reaction types. The reaction types are as follows: (1) Bound Saporin with anti-saporin IgG in solution [96], (2) generic immunoassay values [10], (3) Immobilized C reactive protein (CRP) and anti-CRP IgG in solution [90] and (4) immobilized anti-TNT antibodies with trinitrobenzene (340 Da molecular weight) in solution [89]. Values for the relevant parameters were obtained from literature and are displayed in Table 3-1. For each reaction, a range of chamber heights was used with appropriate scaling of electrode and gap size. An electric field of 100 kV/m was used with a frequency of 100 Hz. Results of this comparison are shown in Figure 3-5(right).

Table 3-1: Binding Constants for the simulation. George *et al.* used immobilized saporin and free IgG as the analyte. Hu *et al.* used generic immunoassay values. Huang *et al.* used immobilized C reactive protein (CRP) and free IgG as the analyte. Vijayendran *et al.* used immobilized anti – TNT antibodies with free trinitrobenzene (340 Da molecular weight)

Parameter	George	Hu	Huang	Vijayendran
$k_{\text{ads}} (\text{mol}\cdot\text{m}^3 \text{ s}^{-1})$	503	100	1E4	320
$k_{\text{des}} (\text{s}^{-1})$	1.83E-4	1E-3	2.6E-2	1.5E-2
$c_0 (\text{mol}\cdot\text{m}^{-1})$	5E-5	1E-4	6.4E-6	3.3E-8

D (mol·m ² s ⁻¹)	1E-11*	1E-11	2.18E-11	19E-10
θ_0 (mol·m ²)	1.35E-7	1E-7	1.4E-8	4.3E-9

As the chamber heights get larger, the surface reaction becomes more transport-limited which makes mixing more beneficial. The mixing enhancement generally increases with chamber height until about 100 μm , where the enhancement plateaus. This plateau is most likely a limitation of ACEO, which, because it is a surface effect, can only extend into the fluid through viscous forces that die out with distance. For the most transport rate-limited case (George *et al*) equilibrium time is reduced by a factor of about 6. For the least transport limited case (Vijayendran *et al*) no improvement is gained from mixing at all. This is to be expected due to the high diffusion coefficient of the analyte.

3.4 Use of ACEO to Improve Fluorescent Immunoassays

3.4.1 Immunoassay Experimental Method

A heterogeneous fluorescent immunoassay can reveal the presence of a biological analyte by binding it to a surface and labeling it with a fluorescent antibody. Using this technique can reveal whether ACEO increases the accumulation of fluorescently labeled antibodies on the surface. These assays were performed on the surface of IDEs and imaged using fluorescence microscopy. In order to test the simplest transport-limited case, a direct, non-specific adsorption assay using fluorescent IgG was employed. This assay, a diagram of which is shown in Figure 3-6(left), consisted of incubating a solution of purified fluorescein-labeled IgG on the IDE surface for an allotted time period. The second assay tests binding on a functionalized surface. In this case, the functionalized surface is prepared by incubating whole rabbit IgG on the surface of the device, blocking with BSA, and then reacting with fluorescein-labeled goat anti-rabbit IgG. A diagram of this assay is shown in Figure 3-6(right).

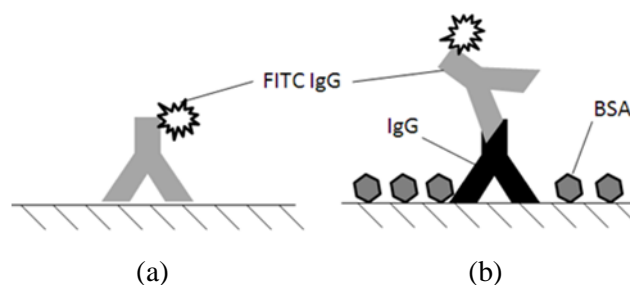


Figure 3-6: Two fluorescent assays were developed to test proof of concept for the ACEO mixer device. (a) shows a non-specific adsorption assay with FITC-IgG. (b) shows an immunoassay with a functionalized surface.

(1) Device fabrication and cleaning procedure

IDEs consisting of chromium/gold electrodes on a glass substrate were fabricated using the lift-off technique, which is described in an earlier work [97]. IDE devices were immersed sequentially in the following solutions for 10 minutes each: methanol, acetone and isopropanol. After drying under N_2 gas, the devices were placed in piranha solution (7:3 $H_2SO_4:H_2O_2$) for 1 minute at 80 °C, followed by a 10 minute immersion in water. The devices were then washed in an ethanol stream, dried under N_2 gas, and then baked dry in an 80 °C oven for 30 minutes.

(2) Antibody solution preparation

Antibody solution was prepared as follows. 2 $\mu S/cm$ water was prepared using a Millipore filtration system and the conductivity was adjusted with potassium chloride. Conductivity was tested with an Orion 105A+ conductivity meter (Thermo Electron Corp). In order to accurately control the final conductivity of the antibody solution, which was originally prepared in PBS,

dialysis was performed. A 20 kDa-cutoff dialysis cartridge (Thermo Scientific) was immersed in the 2 $\mu\text{S}/\text{cm}$ water for 1 minute in order to hydrate the membrane. Next, 300 μl of 0.1 mg/ml FITC goat anti-rabbit IgG (Sigma Aldrich) in 1X PBS was injected into the cartridge and allowed to incubate in a beaker of 2 $\mu\text{S}/\text{cm}$ water for 2 hours. The conductivity of the water in the beaker will increase slightly due to the dialysis and so it was replaced with fresh 2 $\mu\text{S}/\text{cm}$ water half way through the incubation. The IgG was then removed from the cartridge and diluted to 0.01 mg/ml using the same 2 $\mu\text{S}/\text{cm}$ water as diluent.

(3) Description of the Nonspecific binding assay

The nonspecific binding assay was performed by placing the antibody solution in direct contact with the IDE. IDEs were cleaned immediately prior to each experiment. The antibody solution was incubated for 15 minutes on an IDE while the electrodes were supplied with a signal from a function generator (HP 33120A). After incubation, the electrodes were washed in DI water and imaged using fluorescence microscopy (Nikon eclipse ME600 upright microscope). Primarily two geometry electrodes were used: (1) a 100 μm electrode with a 25 μm gap (edge to edge), and (2) a 20 μm electrode with a 20 μm gap. An AC signal (2 V_{pp} and 100 Hz) was applied to each electrode. Other electrodes designs were used and described in the results section.

Image analysis was performed using NIH ImageJ on the 20 μm electrode experiment by measuring the fluorescent intensity in several regions throughout each image. Background fluorescence was removed by subtracting the intensity from an unreacted bare electrode surface (a blank). Each measurement region was taken with a ratio of glass and gold equal to that of the general device ratio. For 20 μm IDEs, this ratio is 1:1.

(4) Description of the Heterogeneous immunoassay

The heterogeneous immunoassay was performed by first functionalizing the surface of the IDE and then reacting with a fluorescent antibody under ACEO mixing conditions. The surface was

functionalized by direct adsorption of 0.1 mg/ml whole rabbit antibodies (Sigma Aldrich) in PBS for 2 hours, after which, the substrate was washed with DI water three times. Next, the surface was blocked with 1 mg/ml BSA in PBS overnight. Negative controls were prepared with BSA alone. To test the effectiveness of ACEO for improving detection, 0.01 mg/ml FITC-anti-rabbit antibodies (Sigma Aldrich) were incubated on the surface for 15 minutes while a 100 Hz signal was supplied to the devices. Devices with the 20 μm gap and those with a 25 μm gap were excited with a 2 V_{pp} and 2.5 V_{pp} signal respectively. Fluorescent microscopy was performed to visualize distribution of IgG binding. Image analysis was performed as in section 2.2.3.

3.4.2 Fluorescent Assay Results

(1) Effect of Varying Frequency and voltage of the excitation signal

Direct adsorption of fluorescent antibodies was performed for a range of frequencies and voltages. Two different designs of electrodes were employed: (1) a 100 μm electrode with a 25 μm edge-to-edge gap and (2) a 20 μm electrode with a 20 μm edge-to-edge gap. The results (Figure 3-7 (first and second row)) show that lower frequencies cause more fluorescent antibodies to attach. The image analysis is shown in the left chart in Figure 3-7 and shows that at the lowest frequencies, the fluorescent intensity is at least 3 times that of the higher frequencies. The frequency dependence shown by the images and chart agrees with the simulation results as shown in Figure 3-5(left). Empirical results show that the 20 μm device outperforms the 100 μm device and is contrary to the prediction made by the simulation which shows the 100 μm device to be superior. It is hypothesized that this is due to DEP, which is indicated by the increased fluorescent intensity near the edges of the electrode and at the ends of the fingers. The possibility of the presence of DEP will be explained in more detail below.

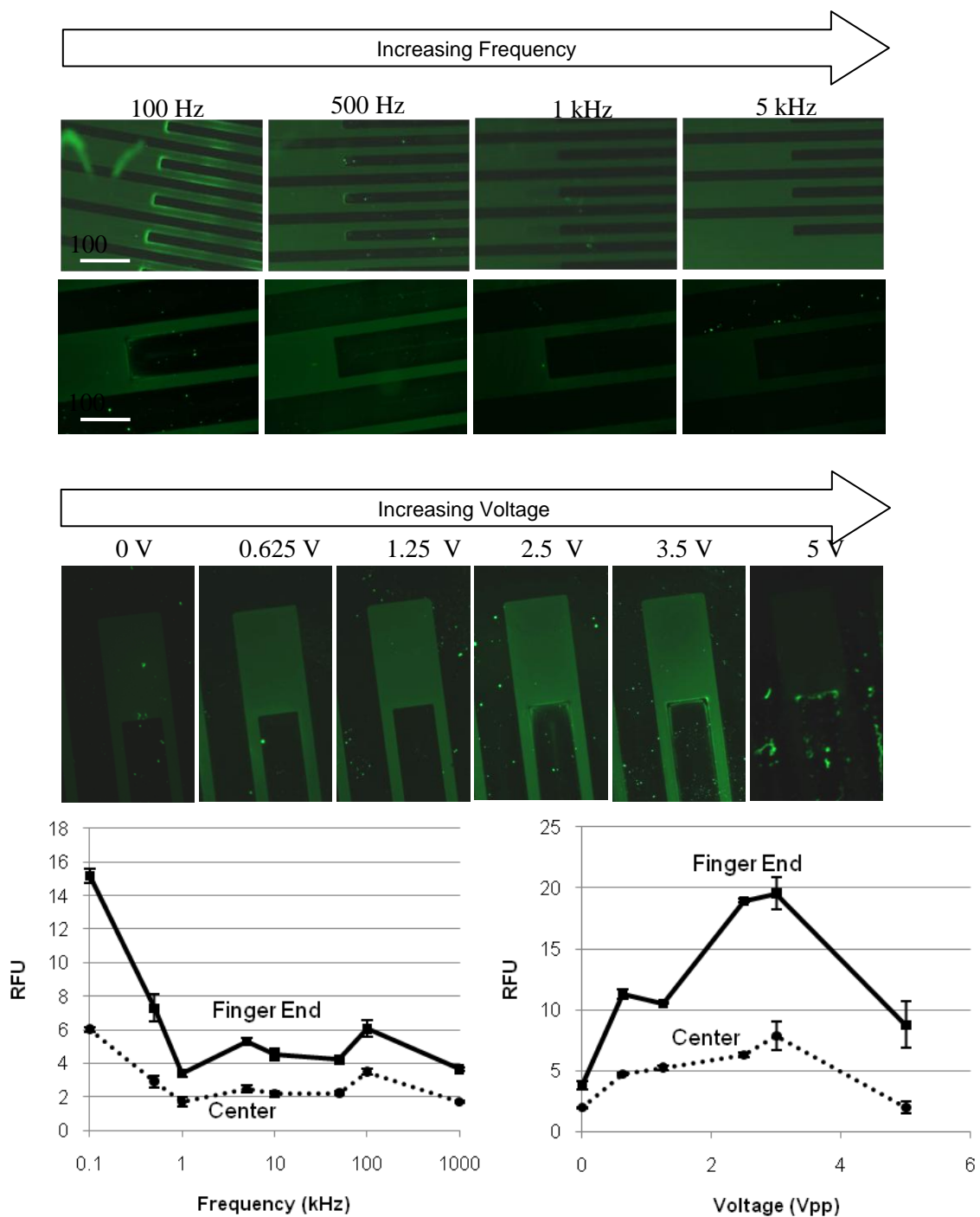


Figure 3-7: First and second row: Direct adsorption assay using 0.01 mg/ml FITC-IgG. The applied signal was 2 V_{pp} and varied in frequency (displayed above). The top row features

electrodes that were 20 μm wide with a 20 μm edge-to-edge gap. The bottom image row shows electrodes that were 100 μm wide with a 25 μm edge-to-edge gap. Third row: Increasing voltage (displayed in V_{pp}) for direct adsorption of 0.01 mg/ml IgG. Solution conductivity was 2 $\mu\text{S}/\text{cm}$ and frequency was 100 Hz. Note the increasing fluorescence till 5 V_{pp} where electrode damage occurred. Bottom: Relative Fluorescence Unit (RFU) for the respective images. The frequency chart (left) was taken from the 20 μm and using some images not shown above. For both charts, fluorescent intensity was measured both near the electrode finger ends and towards the center of the device, each shown in separate plots.

Using the best frequency value (100 Hz), a range of voltages was tested for the 100 μm electrode design. This design was used despite the better performance of the 20 μm design in order to reduce the suspected effects of DEP. The resulting images are shown in Figure 3-7(third row) and a chart showing fluorescent intensity as a function of voltage is shown below. The measurement area for the image analysis contained a ratio of gold to glass of 100:25 in order to match the general device ratio. As expected, the intensity increases with voltage, achieving an enhancement of 4 times at 3.5 V_{pp} (5 near the electrode end) until about 5 V_{pp} where electrode damage was apparent. It should be noted that due to photobleaching and different experimental conditions, relative fluorescence unit (RFU) values from separate assays cannot be directly compared.

(2) Application of ACEO mixing on a functionalized surface

In order to perform selective detection of an analyte, a series of assays was performed with a fully functionalized surface. IDE surfaces were prepared as described in section 2.2.4 and a binding assay was performed using a 100 kV/m maximum voltage at 100 Hz (1 V_{pp} for 10 μm gap, 2 V for 20 μm gap, etc.). The results for 20 μm parallel electrodes are shown in Figure 3-8(top) with

a chart comparing fluorescent intensity of each device and reaction type (bottom). Negative controls consisted of (1) a completely blocked surface under non-mixing conditions, (2) a blocked surface under mixed conditions, and (3) a functionalized surface that was unmixed. (1) shows the effectiveness of the blocking agent to prevent nonspecific binding, (2) shows the same effectiveness under the presence of ACEO, and (3) shows a full immunoassay performed on the IDE without mixing and serves as a baseline against which the other samples may be compared. Two different castellated electrode designs and the 100 μm parallel electrode pattern were tested as well and shown in the bottom row of the same figure. The negative controls for these devices (not shown) are similar to those of the 20 μm devices.

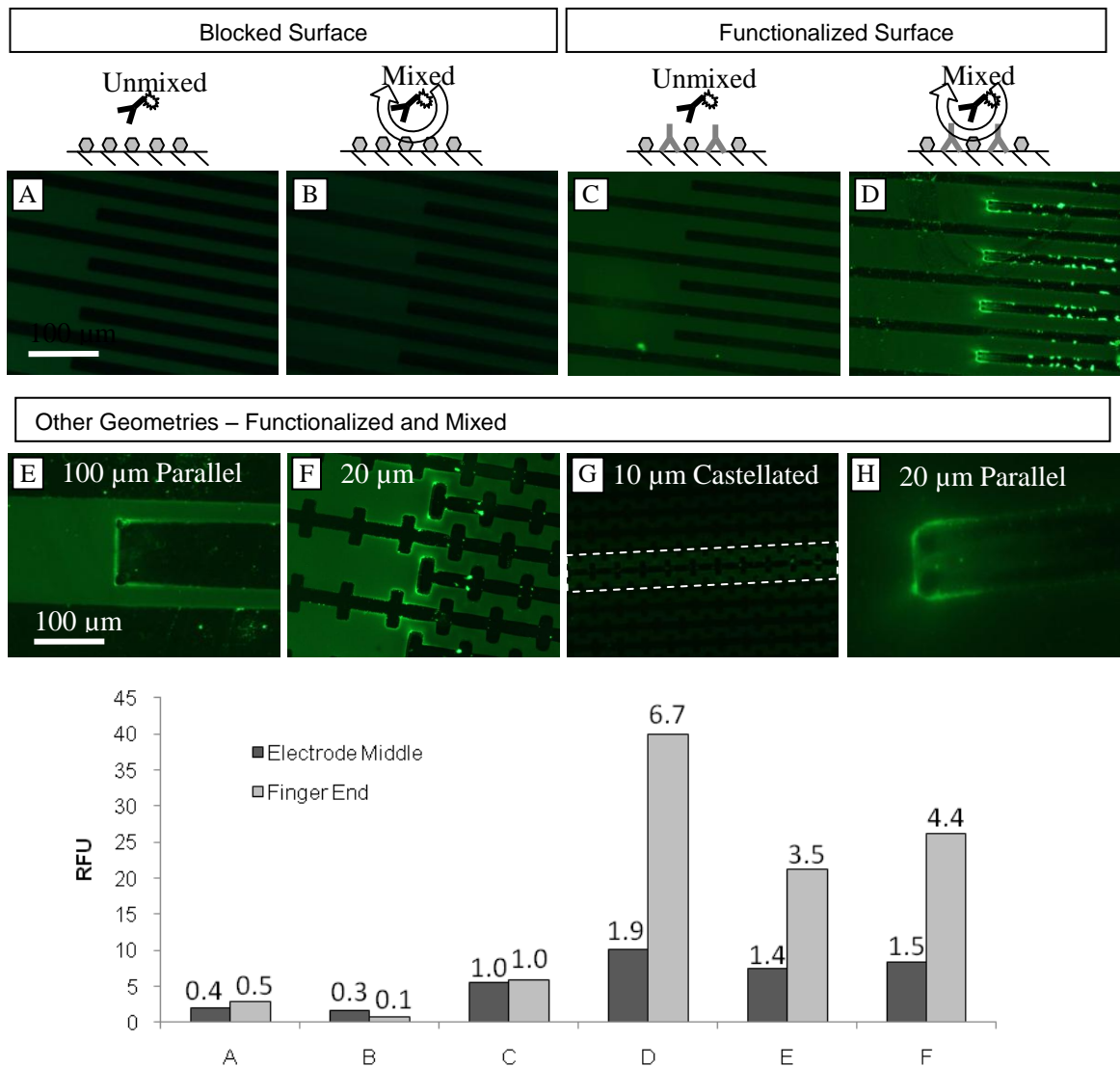


Figure 3-8: Binding of fluorescent secondary antibodies to IDEs. Images are on top and their respective fluorescent intensity is shown in the chart below. Numbers on top of each column indicates the enhancement factor which is the ratio of sample intensity compared to the unmixed

functionalized surface (C). The blocked surface has been prepared with BSA only. The functionalized surface has been prepared first with primary antibody and then blocked with BSA. The mixed samples have been supplied with a 100 kV/m, 100 Hz electric field. Non-mixed samples received no electrical signal. The lower row contains images of the fully functionalized surface with mixing on different geometry electrodes, as well as an enlarged image of the 20 μm parallel electrode. These IDEs were supplied with the same signal as those of the top row. The 10 μm castellated device was serendipitously broken in many places during fabrication, allowing only sparsely activated electrodes. Such an activated electrode is shown in the dotted line. Note the 20 μm parallel electrode has been enlarged 5 times compared to the other images.

Importantly, there was little observable nonspecific binding when active mixing was applied to a completely blocked surface. When comparing activated and inactivated electrodes on fully functionalized surfaces, a large enhancement of fluorescent signal can be seen around the electrode edges. Enhancement of signal (in the center of the IDEs) is shown above each column of the figure and was about 1.4 to 1.9 times improved compared to an unmixed assay. The 10 μm castellated device shows an area of the electrode pattern where only a single active finger is surrounded by broken electrodes on either side. There is manifest enhancement around this single finger compared to its neighbors. The best enhancement occurs near the ends of the electrode fingers reaching an enhancement factor of about 6.7 for the straight 20 μm electrode. This enhancement at the electrode ends may not necessarily be due to the presence of the corners which cause there to be high field strength. Castellated electrodes have many corners and still show this “finger end-effect.” A likely reason is that at the ends of each finger, the electrode has “access” to antibodies past the end of the finger and is thereby made much more efficient. For these reasons, the concentration efficiency at the electrode end will likely surpass the predictions

made by the 2D simulation. This observation has important design ramifications for future devices, especially for biosensors that may incorporate AC electrokinetic assay enhancement. Sensors performing bulk detection across a large surface will not benefit from this end-effect but smaller transducers could benefit from the local 3D concentrating effects.

3.4.3 Surface Concentration Nonuniformity

(1) Investigation of Patterning Using Simulation

An unexpected finding from the fluorescent immunoassay results was that there was a high degree of fluorescence at the edges of the electrodes and much less everywhere else. The simulation results indicate that the surface concentration would be mostly uniform and that no patterning effect would be present (see Figure 3-9). It is clear from this figure that the initial nonuniformity, which is present initially, has rapidly become reduced over time.

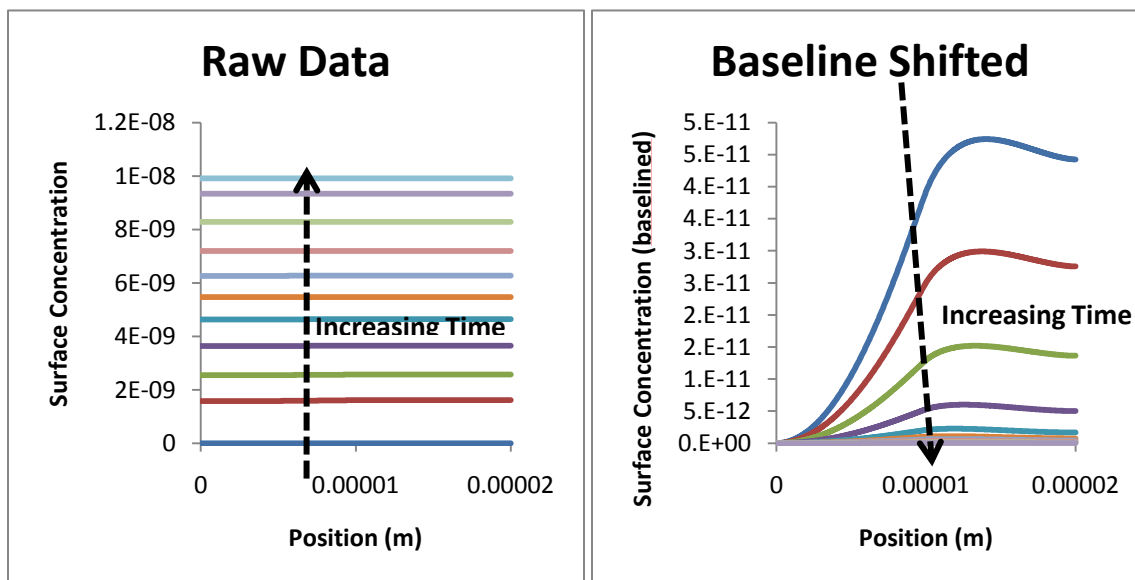


Figure 3-9: Surface Concentration Profiles for George et al constants. Left: Raw data shown for several time points ranging from 1 second to 512 seconds. Each time point is twice that of the former (eg. 1, 2, 4, 8... seconds). Right: The same data as on the left, but the value of the first point has been subtracted from each plot in order to view each time point on the same baseline.

Several reaction parameters could potentially affect the ability of the simulation to produce nonuniform binding. Primarily, though, surface diffusion should be the dominant factor. However, k_{ads} , k_{des} and θ_0 may all have some effect. An investigation of the ability for the simulation to produce nonuniformity was undertaken. First, a parameter set was chosen that eliminated surface diffusion and desorption, increased the forward rate constant ($10,000 \text{ mol}\cdot\text{m}^3 \text{ s}^{-1}$) and the number of binding sites ($1\text{E-}6 \text{ mol/m}^2$). This system is therefore highly transport rate-limited and there are enough binding sites so that analyte will rapidly bind and will not be slowed

down dramatically by a reduction in available sites. The result of this test system shows that surface nonuniformity can be generated for a specific parameter set (Figure 3-10)

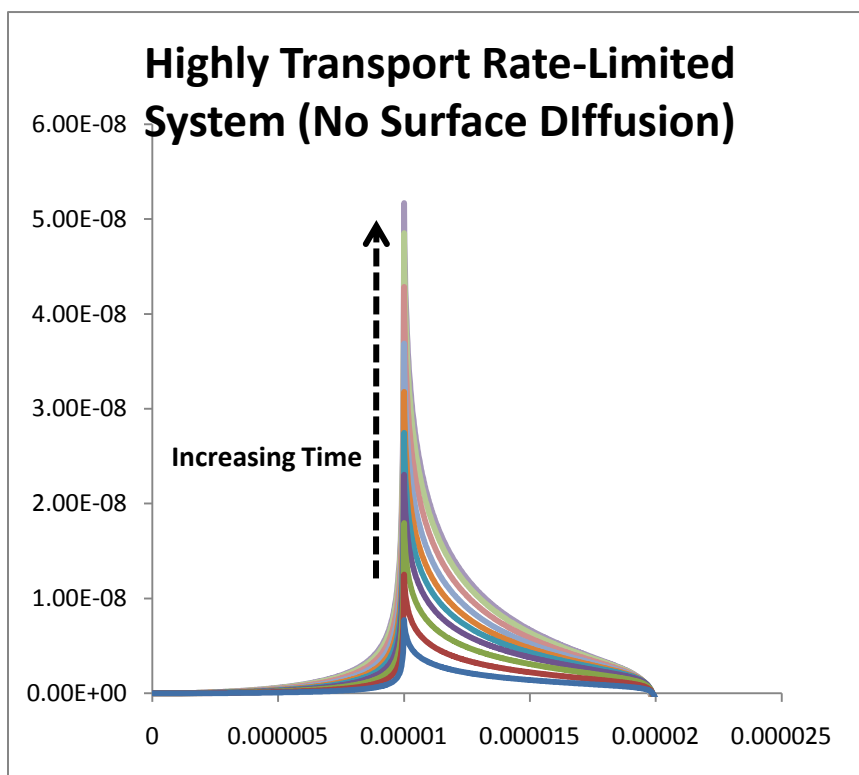


Figure 3-10: Nonuniformity generated by a highly transport rate-limited system with no surface diffusion.

The surface diffusion coefficient (D_s) was studied using this system. Any amount of surface diffusion will ultimately result in a uniform surface concentration at equilibrium. However, in the time scales employed for these binding events, 5-20 minutes, a nonuniformity can be generated even with surface diffusion present. A range of values for D_s was applied to the time dependant

reaction simulation and the degree of nonuniformity was plotted. Degree of nonuniformity was calculated as the maximum concentration divided by the average concentration. The results of these simulations are shown in Figure 3-11.

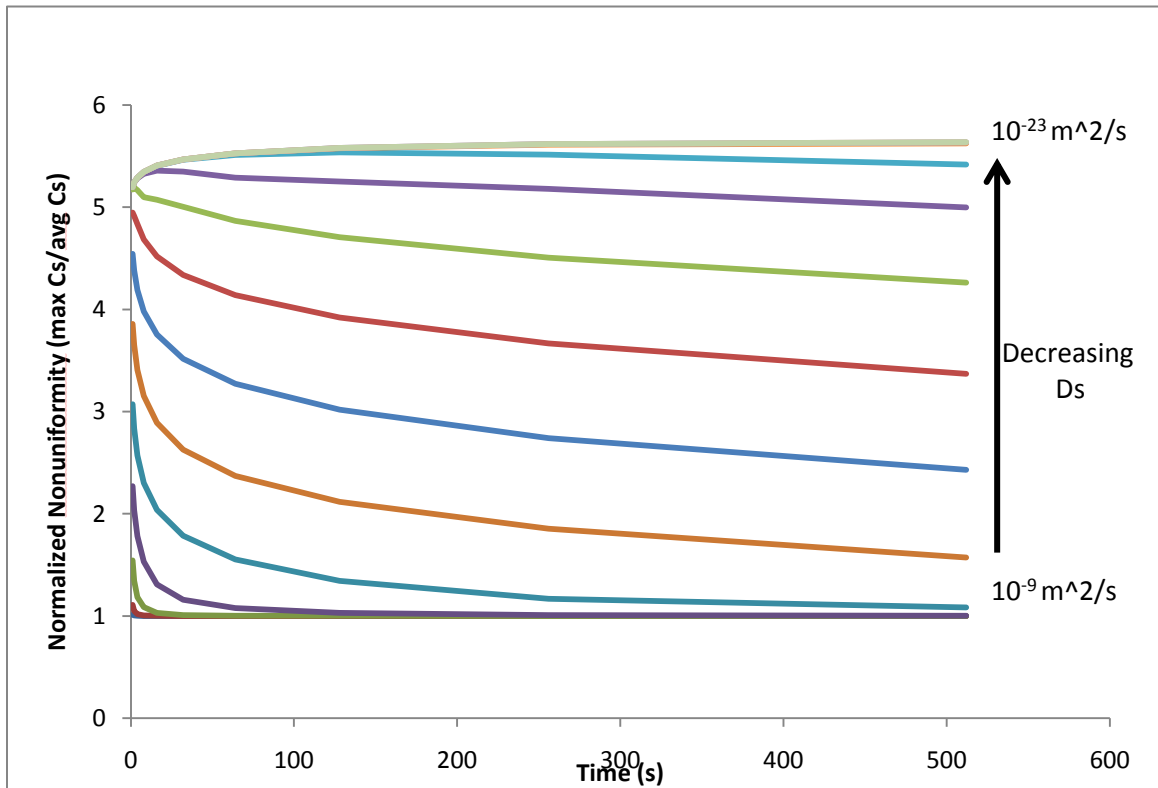


Figure 3-11: Degree of nonuniformity caused by different surface diffusion coefficient values

For all values of D_s , a nonuniformity is initially present to some degree. For high values of D_s , the nonuniformity, immediately begins to disappear as indicated by the downward trend. For very low values of D_s , the nonuniformity increases initially. For the lowest values of D_s , the nonuniformity continues to increase throughout the entire time span. Eventually, even these

simulations would show a decrease as the concentration is used up and the movement of material from high surface concentration to low concentration overtakes the accumulation of material from the bulk.

The initial rate of accumulation as a function of D_s is shown in Figure 3-12. The transition between an initial decrease and an initial increase in nonuniformity occurs when D_s is near 10^{-17} m^2/s . This is 8 orders of magnitude smaller than the D_s used by Hu et al who used 10^{-9} .

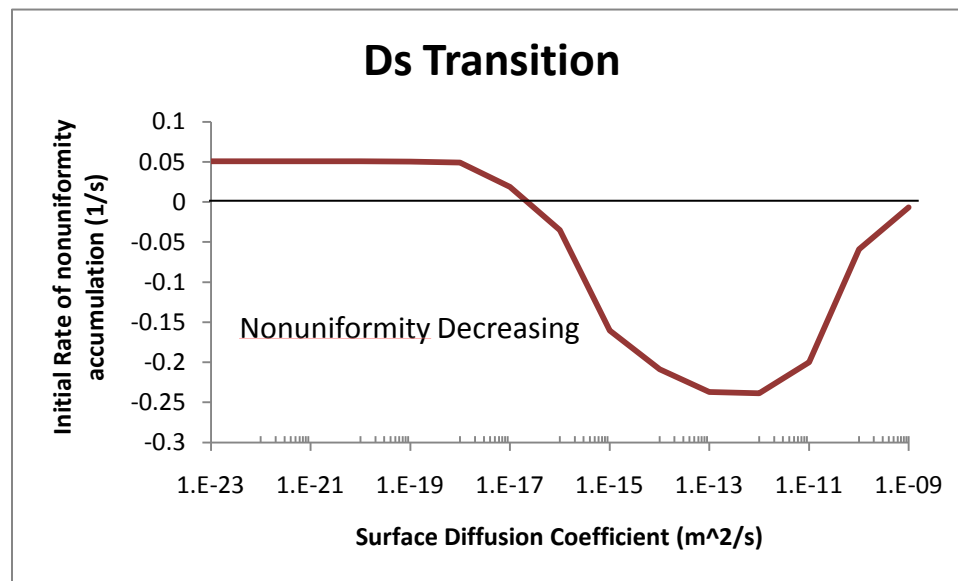


Figure 3-12: Rate of nonuniformity generated as a function of D_s

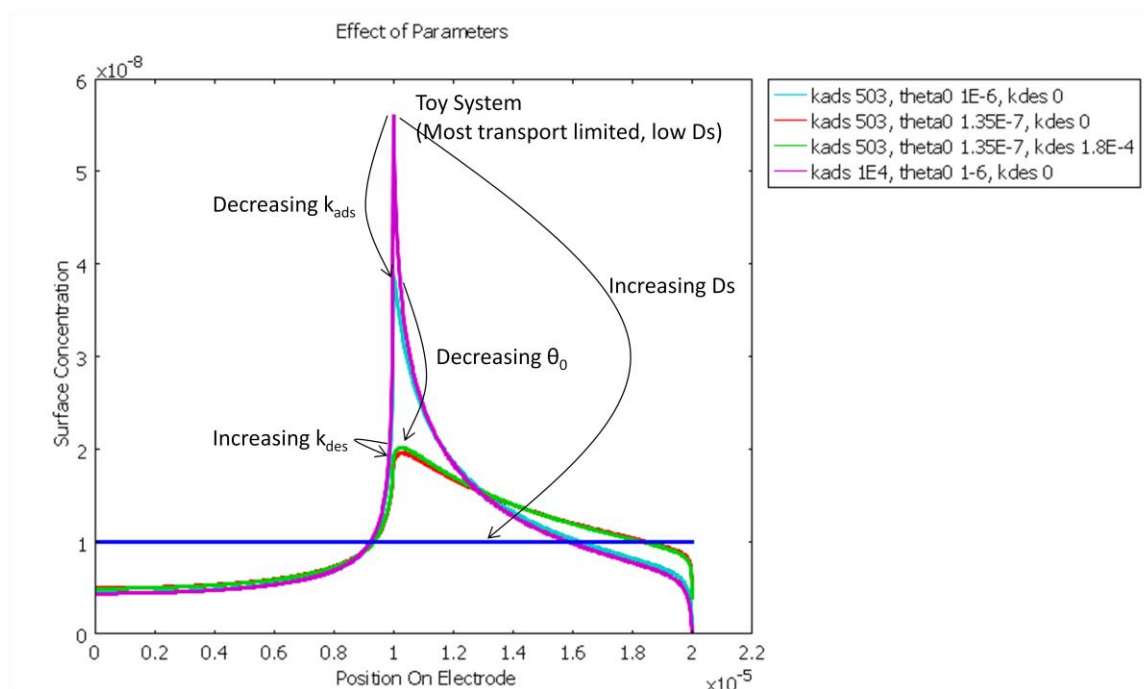


Figure 3-13: Effect of various parameters on the normalized surface concentration nonuniformity after 512 seconds. The “Toy” system is highly transport rate-limited.

In Figure 3-13, the surface concentration is shown after 512 seconds for a variety of different parameter sets. The “Toy System” is the one used in Figure 3-10 and is the most transport rate-limited and contains no surface diffusion. The most dramatic effect comes from increasing D_s to the literature value. However, the other variables do, play a role to some extent.

Some future work is recommended to verify the surface diffusion coefficient experimentally and to validate the theoretically determined cut-off value for D_s that would cause surface concentration nonuniformities. This investigation would additionally require measurement of all reaction parameters, perhaps using surface Plasmon resonance and the ability to measure surface concentration more accurately than is allowed by fluorescence imaging.

(2) Consideration of the Ability for Dielectrophoresis to Affect Antibody Binding

The presence of DEP is a secondary candidate for the presence of surface concentration nonuniformity. (The primary candidate is patterning through the fluidic pattern as mentioned in the previous section). There are, however, two reasons for suspecting DEP may play a role. First, the high degree of concentration of antibodies at the electrode edge is a typical signature of positive DEP. This is present in both the ACEO-binding of primary antibody to a bare surface (Figure 3-7) as well as the labeling of uniformly distributed primary antibody by an ACEO-enhanced secondary antibody reaction (Figure 3-8). As an illustration, a 3D electric field simulation of a castellated electrode shows that the ∇E^2 , which is proportional to the DEP force, closely resembles the pattern produced by the fluorescent antibodies (Figure 3-14). Second, the simulation described in section 2.1, which considers ACEO alone, shows insignificant variation of antibody binding across the surface, even if the surface diffusion term is reduced or removed. However, two arguments would suggest that ACEO plays an important role. First, DEP is not expected to operate deterministically on molecules but instead is typically only useful for manipulating much larger particles. A dimensional analysis performed by Lifeng *et al.* [91] indicates that molecular collection by DEP should not be possible using this electrode geometry without significantly higher voltages (at least two orders of magnitude). (A special case can be made for DNA however [98].) Second, that frequencies around 100 Hz show improved binding, and frequencies greater than 1 kHz show no improvement is a strong indication of ACEO rather than DEP. At the solution conductivities used, ACEO velocity is greatest near 100 Hz and quickly dies out.[65, 97] The DEP force, on the other hand, is expected to be constant in this frequency range. [91] It is therefore suggested that the enhanced antibody collection at the edges is due to a combination of ACEO and DEP. This suggestion is given weight by early observations by Washizu *et al* [99] recent collection of quantum Dots under a combination of ACEO and DEP.[100] However, the quantum dots used were at least two times the diameter of

an antibody which means the DEP force would be at least 8 times stronger. Finally, DEP will have a greater impact on the smaller gap sizes of the 20 μm electrode compared to the larger gap size of the 100 μm device. This explains the better collection of antibodies by the 20 μm device, despite the non-optimal tuning for ACEO as predicted by the simulation.

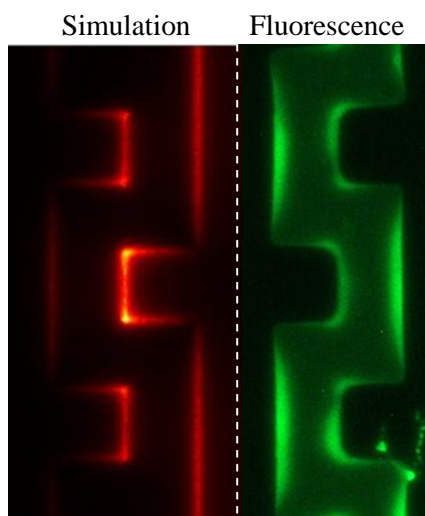


Figure 3-14: Comparison of 20 μm castellated electrode after a direct adsorption assay with a 3D electric field simulation. The simulation side shows ∇E^2 , which is proportional to DEP force.

3.5 Conclusions

This work demonstrates the feasibility of using ACEO to improve the detection time and sensitivity of immunoassays. This improvement appears to be aided by DEP as well, despite the small size of the molecules being used and the relatively large feature size of the devices.

Furthermore, the greatest enhancement occurs near the ends of the electrode fingers due to an

“end effect.” For the best advective mixing, which can shorten the time to reach equilibrium up to a factor of 6, the feature size of the interdigitated electrode should scale with the channel height - the electrode width and gap sizes should be about 70% and 30% of the channel height respectively. The height of the chamber also dramatically affects the binding enhancement. For the voltage and electrode designs simulated, a 100 μm chamber height or above provided the best mixing. Operational parameters were also tested with fluorescent assays. Lower frequencies and higher field strengths exhibited better performance but can also lead to electrode damage and electrolysis of water. Safe ranges include frequencies above 100 Hz and field strengths less than 100 kV/m. Finally, complete heterogeneous immunoassay with a functionalized surface was shown to be enhanced by the use of combined ACEO and DEP with the best improvement occurring at the end of each electrode finger where three-dimensional collection of molecules could take place. For the best design-type, fluorescent signal for these immunoassays was enhanced by a factor of 1.9 in the center of the device and by 6.7 at the ends of the device.

CHAPTER 4: IMPROVED PROTEIN DETECTION ON AN AC ELECTROKINETIC QUARTZ CRYSTAL MICROBALANCE

4.1 Problem Statement

Biosensors generally rely on the reaction or attachment of an analyte with a solid support – usually a bio-functionalized transducer. They can therefore suffer from transport limitations common to many surface-based reactions with biological analytes. The approach to solving this problem was to devise a novel sensor capable of both biological detection and AC electrokinetic actuation. A test sensor was selected (a QCM) and modified using microfabrication techniques. This was characterized both electrically and experimentally, and used to detect antibody binding in the presence or absence of AC electrokinetics. The sensor results were corroborated with the use of protein quantification assays and with fluorescent microscopy.

4.2 Introduction

Biosensors often suffer from long detection times due to the slow transport of biomolecules onto the transducer surface creating a need, especially in microfluidic systems, for a method of continuous active mixing [3, 81-82]. In the microfluidic regime, the low Reynolds numbers preclude turbulent mixing and few active mixing options exist. In this article, the use of AC electroosmosis (ACEO) as a method for enhancing transport of protein to a transducer surface is investigated. ACEO is an electrokinetic phenomenon characterized by stable rotational velocity patterns that exist near the surface (less than a few hundred microns) of microelectrodes (Figure 4-1(left)) [97]. These rotational patterns can be used to stir the bulk solution in a microchannel which will help reduce sensor detection time. A reduction in detection time is often accompanied by a practical increase in sensitivity since a small, but rapid signal may be more

easily distinguished from long term drift. Both a decrease in detection time and an increase in sensitivity can help aid translation of biosensor systems, thereby strengthening their impact on point-of-care diagnostics, environmental monitoring and counterterrorism [83-86].

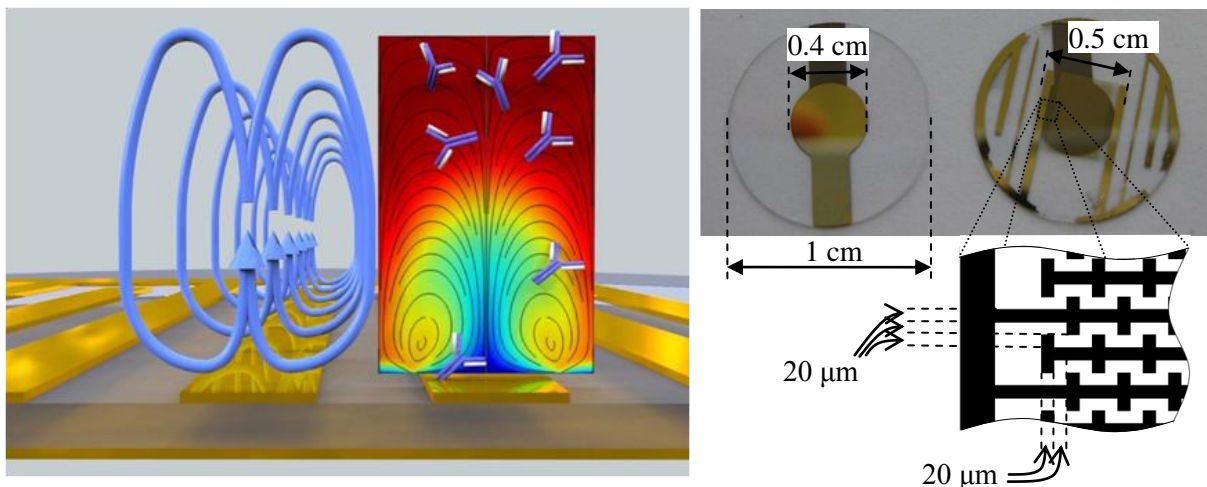


Figure 4-1: Left: a conceptual diagram of ACEO motion (blue arrows) produced by parallel interdigitated electrodes and its effect on analyte concentration (color map) which is removed from the bulk solution by a reaction at the bottom surface. Right: images of a standard QCM (left) and an EKQCM. Image of (left) an unmodified QCM and (right) a QCM that has been modified with a microelectrode pattern. The QCMs used were 1 cm in diameter and 167 μm in thickness.

Quartz crystal microbalances (QCM), were selected as a test sensor because they are well-studied, robust and planar, which allows for easy modification with microfabrication [101-103]. QCMs were modified by replacing the continuous circular electrode with a pair of interdigitated microelectrodes (IDEs), which can generate ACEO (Figure 4-1 (right)). This new sensor-actuator type is termed 'EKQCM' (Electrokinetic Quartz Crystal Microbalance). This term is more general

than ‘DEP QCM’ which was coined by Fatoyinbo *et al*[7] who used a modified QCM to produce dielectrophoresis, another electrokinetic phenomenon. Immunoglobulin G (IgG), a ubiquitous protein used in most immunoassays was used in a direct adsorption assay on the surface of an EKQCM using the dip-dry method to demonstrate proof of concept. By using FITC-labeled IgG and fluorescent microscopy an understanding of the IgG distribution on the sensor surface could be gained and a qualitative comparison of mixed and unmixed sensors could be made. The results from the EKQCM experiments were also compared with predictions made by a convection-diffusion finite element simulation.

The IDEs required to generate ACEO are simple and inexpensive to fabricate and can be incorporated onto most MEMS materials (plastic, glass, silicon, etc...). Voltage and power requirements are quite low - less than 5 V_{pp} and 10 mV respectively. Furthermore, the electrodes can be made thin (tens to hundreds of nanometers), optically transparent and do not generate much heat [26]. The operational frequency is in the sub kilohertz range which is often far enough away from that of many sensor types, allowing for tandem sensor-ACEO operation. The major drawback of ACEO is that it can function only in low conductivity solutions. This technology will therefore be limited to applications where the analyte exists in DI water or where it can be rapidly extracted from highly buffered physiological media using filtration or dialysis. Though the focus of this investigation was for the detection of IgG, the results should be relevant to most proteins, nucleic acids and other biomolecules with high diffusion coefficients.

4.2.1 AC electroosmosis

When an IDE is submerged in an aqueous solution, an electric double layer will form upon application of a potential between the digits. Because the field is non-uniform, (and has a component tangential to the surface) free charges within the double layer will translate across the surface [93]. These moving charges interact with the fluid through viscous drag and cause fluid

motion. The result is a stable rotational velocity pattern depicted in Figure 4-1. Fluid velocities at the surface can reach up to 1 mm/s but die out with distance, causing little motion a few hundred microns away. A more thorough explanation of ACEO including a mathematical discussion can be found in an earlier work [97].

In addition to ACEO, there are two other common AC electrokinetic phenomena, the electrothermal effect (ETE) and dielectrophoresis (DEP). The ETE, like ACEO, is caused by the movement of free charges and results in rotational velocity patterns. However the inducement of the free charges originates with temperature gradients caused by joule heating within the fluid. The ETE is used for high conductivity solutions and has already been investigated for use in improving heterogeneous immunoassays. DEP, unlike the other two effects, acts directly on submerged particles which move toward or away from high electric field gradients.

Unfortunately, DEP cannot be easily used for molecular manipulation (though some exceptions exist) and is typically reserved for handling much larger particles (cells, bacteria, viruses, etc...).

ACEO is commonly generated with IDEs that are parallel and straight. However, a variety of other designs produce ACEO but with different patterns of fluid motion. In this investigation, the castellated design (Figure 4-1) was used because the periodic corners might introduce more folds and bends into the fluid, enhancing the mixing capability.

4.2.2 The transport limited system

Transport-limited systems occur because of the large diffusion coefficients of most biomolecules, the relatively long distances these molecules need to travel and the rapid reactions that take place at the transducer surface. In other words, the reactants near the surface are quickly consumed and are not adequately replenished by fresh reactants which are slow moving and far away from the surface. The result is long binding and detection times which can be improved by adequate

mixing. Figure 4-1 shows a conceptual representation of a mixed (with ACEO) surface reaction on an interdigitated microelectrode. An unmixed case would be represented as a one dimensional concentration gradient.

A system can also be reaction rate-limited if diffusion rates are high, travel distances are small and the reaction rate is fast. To gauge whether a system is reaction rate-limited or transport-limited, a dimensionless number known as the Damköhler number (Da) can be used. This is the ratio of reaction rate to the transport rate. $Da \gg 1$ indicates a system that is highly transport-limited whereas a $Da \ll 1$ indicates a system that is highly reaction rate-limited. Even in microchannels where the diffusion distance is not great, the Da can be on the order of 100 or higher [10].

4.2.3 Quartz crystal microbalance

A QCM is a piezoelectric resonator that has been widely used as a biosensor and has been shown to be capable of detecting both small and large particles such as bacteria[103-105], viruses [106-108], and proteins [102, 109-110]. It consists of a thin disk of AT-cut quartz sandwiched between two electrodes, usually made of gold. Application of an AC current at its resonance frequency produces a standing shear wave. A change in the surface-bound mass will result in a shift in resonance frequency. In vacuum conditions or in air, the change in frequency is directly proportional to mass and can be accurately estimated using the Sauerbrey equation [48].

4.3 Materials and methods

4.3.1 QCM modification

QCMs were modified by replacing one circular electrode with a pair of interdigitated electrodes (Figure 4-1 (right)). The process started with a 10 MHz QCM (100 nm Au/10 nm Ti)

(International Crystal Manufacturing). One side of the QCM was protected with kapton tape while the electrode on the other side was removed with Au etchant (Transene Company Inc.) and 1% Buffered Oxide Etchant (Transene Company Inc.) in deionized water to remove the Au and Ti layers. Photolithography was performed with Futurrex NR-7 followed by thermal evaporation of 10 nm of Cr and 100 nm. Lift-off was performed in Acetone followed by a DI water rinse, a 1 minute cleaning in piranha solution (7:3 H₂SO₄:H₂O₂) and another DI water rinse. Samples were blown dry with N₂ gas.

4.3.2 Measurement system and calibration

Measurement of the QCMs was carried out using an HP4395a network/impedance analyzer connected to a PC with a GPIB/USB cable. The QCMs were placed in a custom-built brass housing with a Teflon chamber. Thin gold wires were passed between o-ring seals and the QCM contact pads to make an electrical connection. These wires were connected to the ports of the network analyzer with SMA cables. For unmodified QCMs, the top and bottom electrodes were connected to the two network analyzer ports. On modified QCMs, the bottom (circle electrode) was connected to one port and either one of the top electrodes was connected to the other port or both of the top electrodes were connected by shorting them together. Resonance frequency was obtained with in-house software programmed using LabVIEW. The software measured the S21 parameter using a 5 kHz span and 1 kHz bandwidth near the resonance frequency. The 0° phase crossing point was found using a least squares linear fit method.

Calibration of QCMs were performed by applying aqueous concentrations (0%, 10%, 20% and 30%) of glycerin to one surface of modified and unmodified QCMs. QCMs were tested before modification and then afterwards. To predict the frequency shift of the QCM to the different concentrations of glycerin, a Mason transmission line model (TLM) was used. This is a representation of the physically based one-dimensional wave and piezoelectric constitutive

equations and boundary conditions [111]. In this model, the piezoelectric crystal is represented with two acoustic ports and one electric port. Then a non-piezoelectric layer (the liquid) is represented by a 2x2 matrix, which converts material properties and acoustical parameters to electrical parameters and vice versa. Acoustic impedance can be determined by calculating the output current and voltage as a linear function of the input current and voltage and the acoustic parameters of the layers [112]. This acoustic impedance is equal to the motional arm impedance of the Butterworth-Van Dyke (BVD) equivalent circuit of a QCM sensor (Figure 2) [113]. This TLM approach was used rather than the Kanazawa equation [51] because the latter ignores static capacitance (C_0) and only considers the motional arm of the BVD circuit. The measurements made with the network analyzer include static capacitance and so the TLM was more suitable.

4.3.3 Antibody adsorption assays

(1) Antibody detection on EKQCM

Antibody binding onto the surface of the EKQCMs was measured using the dip-dry technique, which entails comparing the resonance frequency of the sensor before and after a period of binding. EKQCMs were first cleaned by immersing them in methanol, acetone and then isopropanol for 10 minutes each, followed by drying under N_2 gas. Next, the EKQCMs were placed in piranha solution (7:3 $H_2SO_4:H_2O_2$) for 1 minute at 80 °C, followed by a 10 minute immersion in deionized water. A final wash in ethanol was followed by another drying step and a bake in an 80 °C oven for 30 minutes.

In order to accurately control the conductivity of the antibody solution, which has a large impact on ACEO, a dialysis step was used. Deionized water was adjusted to 2 $\mu S/cm$ using potassium chloride while monitoring with a conductivity meter (Orion 105A Thermo Scientific). A 20 kDa-cutoff dialysis cartridge (Thermo Scientific) was first hydrated for 1 minute in the 2 $\mu S/cm$ water. Next, 300 μl of 0.1 mg/ml affinity-purified polyclonal FITC goat anti-rabbit IgG (Sigma Aldrich)

in 1X PBS was injected into the cartridge and allowed to incubate in a beaker of 2 $\mu\text{S}/\text{cm}$ water for 2 hours. The solution was replaced after one hour since the conductivity of the water in the beaker will increase slightly due to the dialysis. IgG was then removed from the cartridge and diluted to 0.01 mg/ml using the same 2 $\mu\text{S}/\text{cm}$ water as diluent.

To perform the dip-dry experiment, the resonance frequency of eight EKQCMs was measured and a 50 μl droplet of antibody solution was pipetted directly onto the surface of each sensor for 15 minutes. ACEO mixing was applied to four of the EKQCMs by supplying the IDE with a 2 V_{pp} , 100 Hz signal. The other four interdigitated electrodes remained inactive. The liquid from each device was then carefully aspirated and saved. (Solution could not be recovered from two out of the four activated QCMs due to mishandling.) Next, the EKQCMs were washed in deionized water 3 times and dried under N_2 . This was followed by another resonance frequency measurement and imaging with fluorescent microscopy (Nikon eclipse ME600 upright microscope).

The saved solutions from each QCM were then subjected to a protein quantification assay (MicroBCA, Thermo). By comparing the concentration of the initial solution to the solutions after they had been applied to the QCM surfaces, the amount of adsorbed protein could be determined. A standard dilution of IgG was prepared in 2 $\mu\text{S}/\text{cm}$ water in a transparent 96-well corning plate. Samples from the QCMs were added to the well plate and all samples were mixed with MicroBCA reagents and incubated for 1 hour at 37 $^{\circ}\text{C}$. After 5 minutes of cooling, the absorbance of each well was measured using a plate reader (Tecan Infinite M200) at 562 nm. The linear fit R^2 value was 0.999.

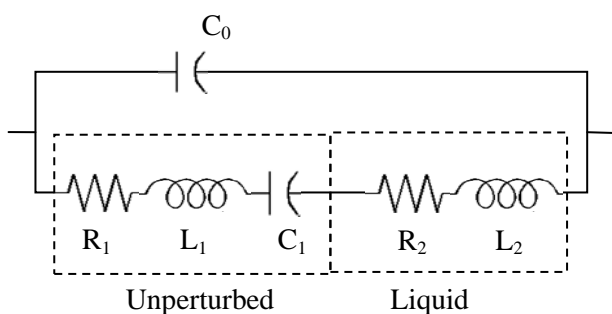
(2) *Immunoassay on functionalized surface*

The ability of IgG to retain its function after subjection to dialysis and high strength electric fields (up to 100 kV/m) is vitally important for future applications. This was tested with fluorescent

immunoassays performed on interdigitated electrodes fabricated on glass substrates. The immunoassays consist of (1) functionalizing the surface of a device with direct adsorption of 0.001 mg/ml IgG in 1X PBS for two hours, (2) blocking with 1% BSA in 1X PBS overnight and (3) labeling with 0.001 mg/ml fluorescently labeled secondary antibody in 1X PBS for two hours. A short incubation with ACEO was substituted for either the first step (case 1) or the third step (case 2) with the other steps remaining the same. In the steps using ACEO, PBS solution was replaced with 2 μ S/cm water using dialysis and incubation times were reduced to 15 minutes. Case 1 shows whether a protein (the primary antibody) may be first subjected to ACEO and then successfully labeled. Case 2 shows whether a protein (the secondary antibody) may be successfully captured by a receptor layer in the presence of ACEO. Both cases were compared to unmixed samples that received similarly short, 15 minute incubations.

4.4 Results and Discussion

4.4.1 Electrical testing and calibration



Parameter	Standard QCM	ACEK one finger	ACEK both fingers
R_1 (Ω)	6.65	23.63	7.87
C_1 (fF)	27.97	27.60	27.69
L_1 (mH)	9.10	9.19	9.16
C_0 (pf)	7.13	5.84	7.16
Q	5318	4596	5278
Δf (kHz)	-	-23.90	-22.53

Figure 4-2: Electrical equivalent circuit of TSM sensor. C_0 : static capacitance of quartz, C_1 , R_1 and L_1 are intrinsic capacitance, resistance and inductance of quartz respectively. R_2 , L_2 represent the liquid loading.

The electrical equivalent circuit for a QCM is shown in Figure 4-2. Using the impedance analyzer mode of the HP 4395a, values for R_1 , C_1 , L_1 , and C_0 were extracted from a standard QCM as well as for the ACEK QCM. The ACEK QCM could be operated using just one of the top electrode fingers or by shorting the top two electrodes. Both cases were measured and the equivalent circuit values are shown in Figure 4-2. Compared to the shorted top electrode option, the single-finger operation has greater electrical losses at resonance, which is explained by the high R_1 value. The quality factor (Q) is quite high for all cases and is only slightly negatively affected by the alteration to the top electrode. Using only one finger reduced the Q by about 14% from the original. Q was calculated by dividing the resonance frequency by the span at -3 db from resonance amplitude.

A simple prediction of the resonance frequency shift that would be caused by modification of the QCM ($\Delta f_0 = f_{0-original} - f_{0-modified}$) can be made using the Sauerbrey equation. Typically used for estimating deposition of mass on the surface, the Sauerbry equation predicts a linear relationship between resonance frequency and deposited mass. According to this equation, the sensitivity of the 10 MHz QCM is about 2.89 Hz/ng. The original electrode area was $7.85E-6 \text{ m}^2$ and its thickness was 100 nm of gold and 10 nm of titanium. This solid electrode was replaced with a set of castellated electrodes, the pattern of which has a special coverage of about 50% compared to the solid electrode (100%). The castellated electrode was made from 100 nm Au and 10 nm Cr. The difference in mass between the original and modified QCM will be about 7,500 ng, which would cause a 21.68 kHz frequency shift. (This calculation only considers the acoustically active

region that overlaps with the bottom electrode and ignores the parts of the top electrode that don't overlap). The experimental resonance frequency shift that occurred during the fabrication process is shown in the last row and differs from the predicted frequency shift by about 10% for the single-finger operation and by 4% for the dual-finger operation.

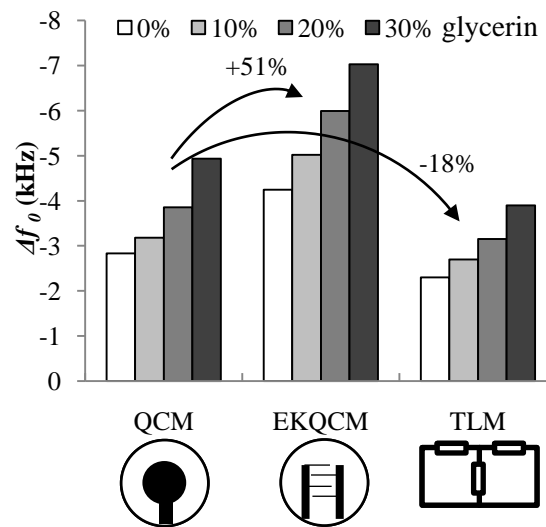


Figure 4-3: Frequency response of the QCM and EKQCM to varying aqueous concentrations of glycerin. A prediction made by the transmission line model (TLM) is in the final column group.

QCMs are also sensitive to changes in the viscosity and density of a fluid in contact with the transducer surface. In order to ensure that the EKQCM can still function similarly to an unmodified QCM, different aqueous concentrations of glycerin were applied to the sensors and the resonance frequency shift was measured ($\Delta f_0 = f_{0\text{-liquid}} - f_{0\text{-air}}$) and compared. The transmission line model, detailed in Section 2.2 was also employed and the simulation results are shown

alongside the empirical data in Figure 4-3. The three data sets show a similar relationship to the different concentrations, though with differing sensitivity. Compared to the QCM, the EKQCM was approximately 51.4% more sensitive while the transmission line model predicted a sensitivity of approximately 18.2% less. If the values for each technique were normalized by compensating for sensitivity differences, the greatest error between techniques for a given concentration would be less than 3.2%.

Though interesting, the improved sensitivity of the EKQCM to the properties of the liquid load is not the central focus of this inquiry but rather, the fact that the EKQCM functions well as a sensor at all. An investigation of this improved sensitivity will be left for future work.

4.4.2 Antibody sensor detection

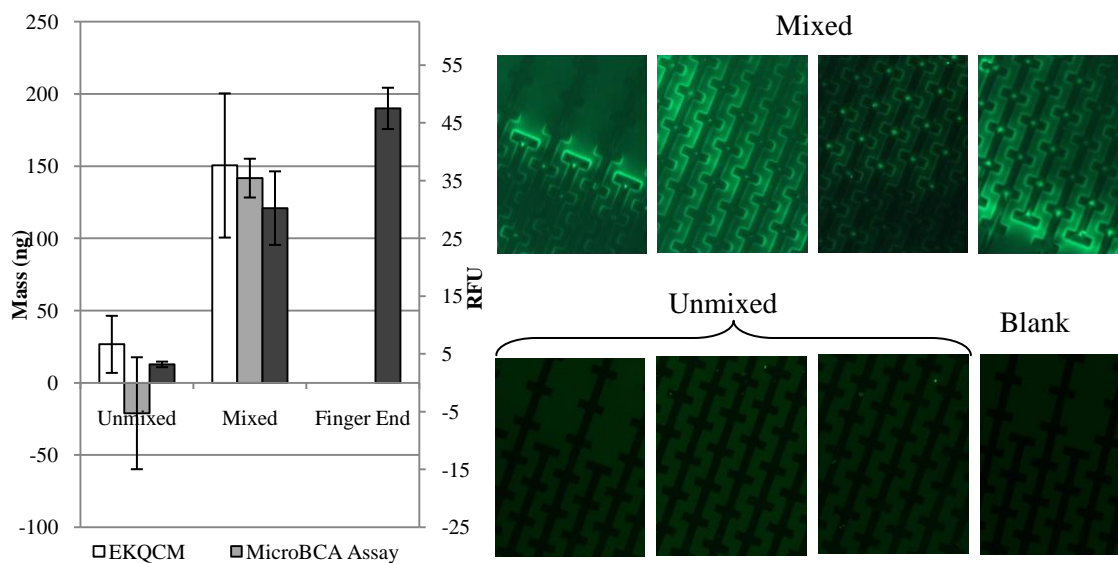


Figure 4-4: Sensor, protein assay and fluorescence imaging results. The chart shows the quantity of adsorbed protein using three different approaches. Note that the fluorescence series uses the

secondary axis on the right and is the only method that can measure values from the finger end. The others are bulk measurement techniques. The images show mixed samples, unmixed samples and a blank, which was not subjected to any fluorescent IgG. (EKQCM n=4, MicroBCA assay (unmixed n=4, mixed n=2), Fluorescence n=10).

A comparison of the mixed and unmixed EKQCMs for a 15 minute incubation in 0.01 mg/ml IgG is shown in Figure 4-4(left). The EKQCM response was converted from frequency to mass using the Sauerbrey equation. The adsorbed mass provided by the MicroBCA assay was calculated by comparing the concentrations of the solution before and after the 15 minute incubation. The concentration 'lost' during this process was considered to be adsorbed onto the surface and was converted to mass and plotted. The negative value for the unmixed sample is due to measurement error and can be considered close to zero. According to the EKQCM data, in the 15 minute incubation, the amount of mass adsorbed was increased by a factor of about 5.6.

In addition to these quantitative methods, which closely agree, fluorescent photomicrographs are provided and show good qualitative agreement as well. Fluorescent intensity was also measured from ten locations for each condition and the average value was plotted on Figure 4-4.

Background fluorescence was subtracted using measurements from the blank sample, which was not reacted with protein. The fluorescent micrographs indicate a fluorescent enhancement of 9.5 in the middle of the device and 14.9 at the electrode fingers. Interestingly, the antibody is preferentially adsorbed near the edges of the activated electrodes and also towards the ends of each finger – a pattern that usually indicates DEP. Furthermore, there are spots of high antibody intensity at the center of the castellated 'cross' regions, which is highly indicative of ACEO particle collection. This might indicate the possibility of agglomerated IgG, the increased size of which would make them more susceptible to DEP. Fluorescent intensity is also much higher at

the ends of each finger – an effect likely caused by the ‘access’ the finger has to IgG past the end of the finger. Images of polystyrene microspheres under the influence of AC electrokinetic forces that show similar collection patterns were discussed in a previous work.[97]

4.4.3 Immunoassay on glass IDEs

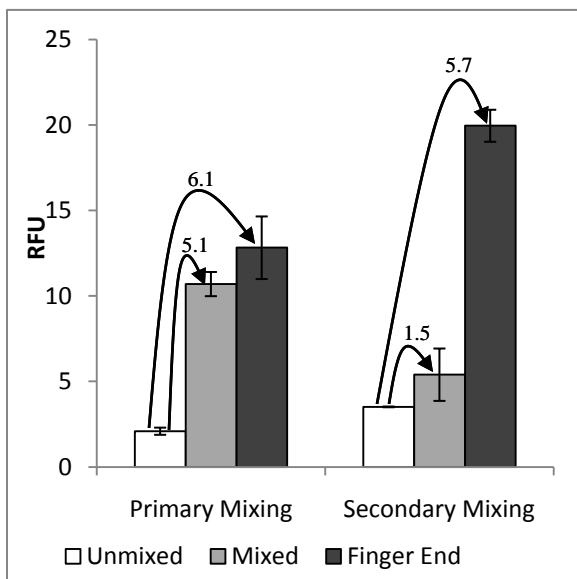
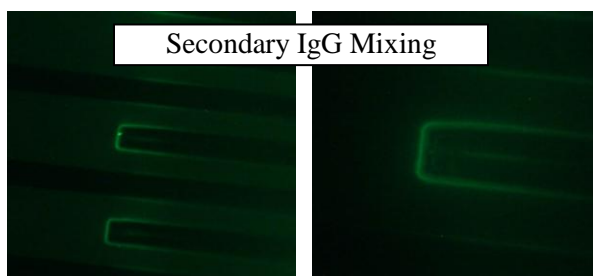
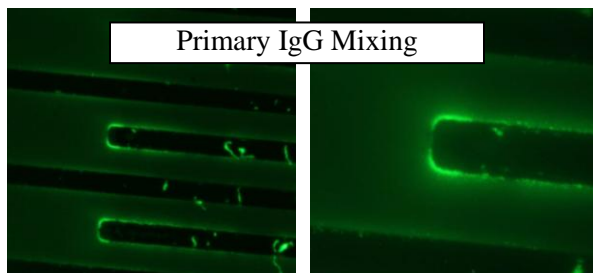


Figure 4-5: Fluorescent immunoassays performed on IDEs with AC electrokinetic mixing. Two variations are shown on the normal three-step assay which is as follows: (1) 2 hour primary IgG incubation, (2) overnight 1% BSA blocking, (3) 2 hour secondary IgG incubation. Left: Images from immunoassays subjected to AC electrokinetic forces during either step 1 (primary IgG mixing) or step 3 (secondary IgG mixing). Right: Fluorescent intensity measurements. Background fluorescence was removed by measuring a blank sample. Labeled arrows show an enhancement factor from the unmixed sample. (Unmixed n=4, Mixed n=4, Finger End n=3)

In order to perform selective detection of an antigen, a biosensor must first be functionalized with a receptor layer. Results so far have only indicated the ability of ACEO to enhance nonspecific binding and do not indicate whether the antibodies have retained function after subjection to high electric fields and the dialysis procedure. To test this, the assays described in section 2.3.2 were carried out and the results are shown in Figure 4-5. Like the direct adsorption assay, antibody attachment around the edges of the electrode is much more pronounced and collection at the finger ends is also much greater than in the center of the device. In both cases, fluorescent signal near the finger ends is enhanced by about 6 times. However, in the center of the device, mixing during the primary IgG binding step was much more effective than during the secondary step. It is not clear why this discrepancy exists but it is conceivable that the immune complex, which is formed during the secondary IgG step and is larger, is therefore more susceptible to shearing forces encountered during active mixing, which might cause them to be removed from the surface.

4.4.4 Electrode damage at high voltages

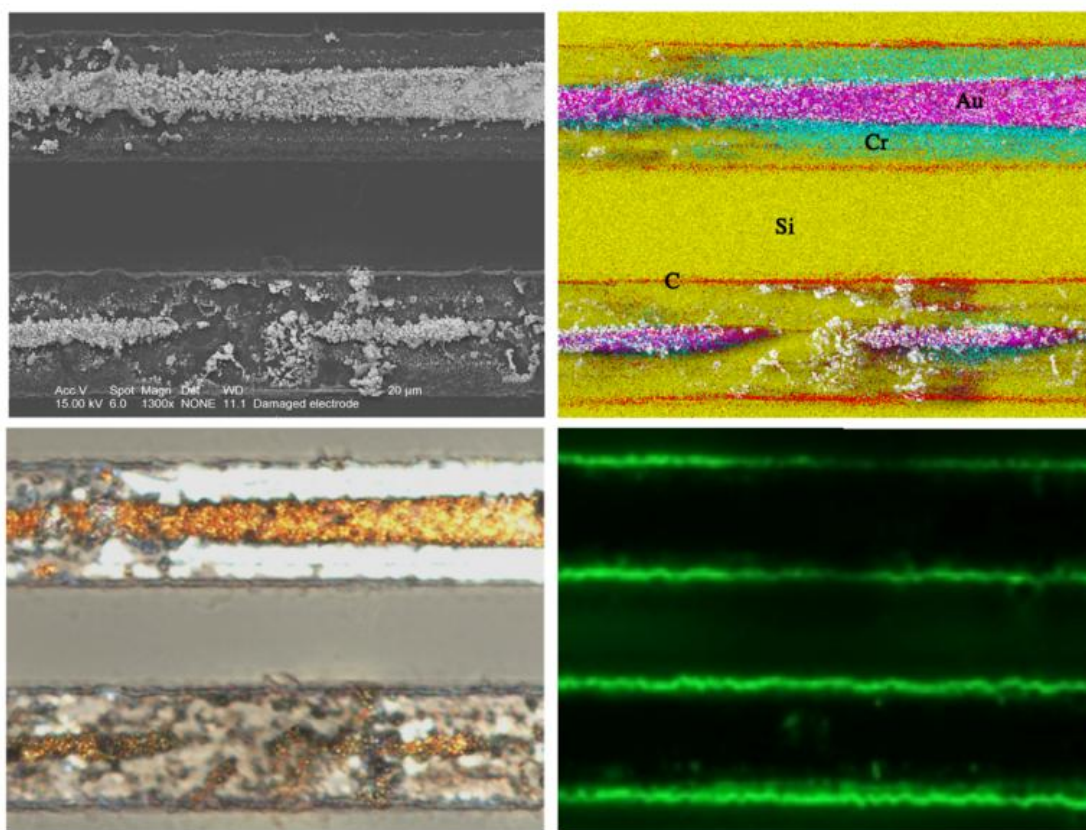


Figure 4-6: The same location on the device was analyzed with four different techniques: scanning electron microscope (Top left) energy-dispersive X-ray analysis (Top right), light microscopy (Bottom left) and fluorescent microscopy (Bottom right).

Throughout the experiments, a voltage of $2 V_{pp}$ was applied to the electrodes to induce electroosmotic mixing. The maximum field strength in this case is about 100 kV/m. Increasing voltage has the clear effect of increasing antibody collection on the electrodes. However, voltage cannot be raised indefinitely due to electrolysis of water and damage to the electrode itself. Others have reported similar findings without investigation [24, 114]. It was noted that $5 V_{pp}$ (field strength of about 250 kV/m) or greater caused visible electrode damage. It was therefore

decided that voltages no higher than $2 V_{pp}$ would be used. The mechanism of this damage is currently unknown but, like electrolysis of water, the electrode damage is dependent on voltage and frequency and it seems likely that this is due to some electrochemical reaction. Lower frequencies and higher voltages are more likely to damage the electrode. Interestingly, this damage also is related to the antibody concentration. Higher concentrations of antibodies in solution are more likely to damage the electrodes. To study this phenomenon, a straight parallel IDE (20 μm electrode width and 20 μm gap width) was severely damaged by applying a 10 V_{pp} 100 Hz signal for 30 minutes using an antibody concentration of 0.1 mg/ml with a solution conductivity of 1 $\mu\text{S/cm}$. Images of the damaged device using four different modalities are shown in Figure 4-6. In some locations, both the gold and the chromium layers are removed, and in others, only the gold. Antibodies are accumulated on the electrode edges even when the electrode is no longer there. It is hypothesized that the electrodes are being removed by an electrochemical process (perhaps electrodisolution of Cr, which can happen has been shown to occur in acidic conditions at high DC field strengths [115]) that may be enhanced by the presence of the antibodies.

4.5 Conclusion

For the first time, ACEO has been used to improve detection of protein on a biosensor. Using this phenomenon as a means of stirring diffusion-limited adsorption of protein onto a transducer surface resulted in an increase of bound protein by a factor of 5.6. In order to accomplish this, a novel electrokinetically enhanced transducer, an electrokinetic QCM (EKQCM), was designed and fabricated. The increase in the amount of adsorbed protein was corroborated by a protein assay, as well as with fluorescent microscopy, the former agreeing with the estimated mass deposited on the EKQCM and the latter showing a bulk enhancement of 9.5 times. Near the electrode finger ends, the fluorescent intensity was greatest with an enhancement of about 14

times. Immunoassays on interdigitated electrodes were used to show that this technique did not significantly decrease protein function. ACEO was used either during the direct adsorption of primary antibody to the transducer surface (enhancement of 5.1 times in the device center and 6.1 times at the finger ends) or during the binding of secondary antibody to the primary (enhancement of 1.5 times in the device center and 5.7 times at the finger ends). ACEO mixing velocity increases with voltage which benefits performance. However, this can eventually damage the device, as evidenced by brown discoloration and removal of areas of the gold and chromium electrodes. It was considered safe to use a 100 Hz, 2 V_{pp} signal which creates a maximum 100 kV/m electric field. An applied voltage of 5 V_{pp} or higher resulted in damage and device failure.

CHAPTER 5: CONCLUSION & FUTURE WORK

The often long detection times for analytes in biosensor systems is a limiting factor for the translation of new technologies which could help transform healthcare, environmental monitoring and counterterrorism efforts. These long detection times are, in many cases, due to the slow transport of reactants to the sensor surface. The central hypothesis of this work was that AC electrokinetics could quicken this transport by providing advective mixing near the surface of a biosensor or other solid detection region. This hypothesis was tested during the course of this thesis using antibodies as a test analyte and a quartz crystal microbalance as a test sensor. The conditions and details of binding enhancement were analyzed using a variety of different overlapping techniques. A general characterization and evaluation of the forces involved was gained through the use of finite element simulations and through careful observations of particle behaviors under a wide variety of conditions. Fluorescent antibodies were used to observe

surface binding under the influence of AC electrokinetics. Finally, a novel biosensor capable of performing AC electrokinetic actuation as well as mass sensing was constructed and used to show proof of concept for improved antibody binding.

5.1 Specific Aims

5.1.1 Aim 1: Characterize AC electrokinetic forces

Micro- and nanoparticles display a multitude of different behaviors under the presence of nonuniform AC electric fields. The different behaviors, which can be seen in Figure 2-8, include assembly-lining, edge collection, orbiting, particle chaining, active concentration and levitation. These different behaviors were isolated experimentally under the different conditions required to bring them about, which included (1) size and concentration of a submerged particle, (2) geometry of the electrodes, (3) voltage and frequency of the applied signal and (4) conductivity of the immersing solution. A deeper understanding of the forces generated by these electric fields was gained through the use of a finite element model which, unlike its predecessors in the literature, included all three of the major AC electrokinetic phenomena. This model showed good agreement with the experimental observations and provided a means to extract valuable relationships between important parameters and the generated AC electrokinetic forces that were not able to be learned from experimental observations alone. For example, the individual contribution of forces from each electrokinetic effect could be learned as well as how these forces are distributed throughout the microchamber. Important parameters such those described above [(1), (3) and (4)] were studied in order to show corroboration.

5.1.2 Aim 2: Evaluate the effect of AC electrokinetics on transport-limited heterogeneous immunoassays

The information gained from this elementary understanding was then applied to the problem of improving heterogeneous assays. The aforementioned finite element model was modified so that it was able to track the movement of analyte material undergoing a surface reaction under the presence of AC electrokinetics. Again, important system and operational parameters were studied so that the optimum geometry of the device, best frequency range, conductivity, etc... were learned. The improvement to be gained was also predicted for a wide variety of common reaction chemistries discussed within the research community. The model was, again, accompanied with empirical observations in the form of fluorescent protein assays. Interestingly, the presence of AC electrokinetics caused the antibodies to become patterned on the surface, an unexpected finding which was investigated and believed to be due to the contribution of dielectrophoretic force. Stirring a heterogeneous immunoassay was shown to improve the binding of antibody by a factor of 1.9 near the center of the device and a factor of 6.7 near the device edge.

5.1.3 Aim 3: Quantify the effect of AC electrokinetics on a biosensor system

A novel sensor, capable of generating AC electrokinetic forces on its surface, was constructed using microfabrication techniques. The so-called EKQCM underwent a suite of electrical and experimental tests to determine that the sensor still functioned as expected and that the performance was not severely limited by alteration. In fact, the quality factor was only reduced marginally (-14% compared to a normal QCM) and the sensitivity of the EKQCM to changes of viscosity was improved by 51% compared to a normal QCM. Sensor measurements of protein binding events showed that the use of AC electrokinetics improved the response by about 5.6 times which was corroborated by a quantitative protein assay. Fluorescent images of the sensor surface showed an even more dramatic improvement 9.5 times at the device middle and 14.9 times at the device edges. Concurrent tests done on glass electrodes using similar conditions but

performing full immunoassays with primary and secondary antibodies showed fluorescent enhancement of 1.5-6 times depending on which step was mixed and the image location.

5.2 Contributions

There are three main areas to which this thesis contributes. First, a deeper understanding of a relatively new set of phenomena was gained by experimental and computational means (section 5.2.1 below). Second, AC electrokinetics was applied to improving immunoassays which was not shown before this thesis work. Third, a novel sensor, equipped with AC electrokinetic capabilities was constructed and shown to enhance protein binding kinetics.

5.2.1 Contributions from CHAPTER 2: COMPREHENSIVE ANALYSIS OF PARTICLE MOTION UNDER NON-UNIFORM AC ELECTRIC FIELDS IN A MICROCHANNEL

(1) Development of a computational method for predicting particle behavior

AC Electrokinetics is a relatively new field, especially when applied to microfluidics. As such, there are very few published computational means to predict particle and fluid behavior. Under conditions where the different AC electrokinetic forces are overlapping, there were no published predictive methods at all. The work described in CHAPTER 2: COMPREHENSIVE ANALYSIS OF PARTICLE MOTION UNDER NON-UNIFORM AC ELECTRIC FIELDS IN A MICROCHANNEL, and which has been published in the peer review literature contributes such a method. Now engineers and scientists who wish to design a system using AC electrokinetics will be able to refer to this work in order to model their system. The complex nature of these forces, which depend on many different parameters, often makes such modeling essential for the successful development of a device. The essential parameters affecting these forces were incorporated into the model so that a wide range of behaviors and effects can be predicted. The

model considers system parameters, such as the geometry of the electrodes and microfluidic chamber, thermal properties of the materials and the size and electrical properties of the particles. Operational parameters included the conductivity and temperature of the fluid as well as frequency and voltage of the applied electrical signal. No models before this included all of these important parameters.

(2) *Description of relationships between parameters and AC electrokinetic forces*

A quantitative description of the theoretical relationships between parameters and AC electrokinetic forces was provided in this chapter as well. How the forces change with distance from the electrode, with frequency and voltage of the applied signal, with conductivity of the fluid and particle size were all discussed in great detail and provided to the community where such information was not readily available.

(3) *Explanation of particle behaviors under non-uniform electric fields*

The AC electrokinetic force model described in CHAPTER 2: COMPREHENSIVE ANALYSIS OF PARTICLE MOTION UNDER NON-UNIFORM AC ELECTRIC FIELDS IN A MICROCHANNEL was subsequently used to help explain the many different types of behaviors that particles exhibit when under non-uniform electric fields. Though many of the behaviors are understood by the community in a limited sense, the analysis described in this chapter provides a more quantitative understanding. Furthermore, subtle differences between particle behaviors can now be much more accurately described. For example, particle orbiting is known to be caused by AC electroosmotic flow. However, how the location of the orbiting center point changes with frequency and conductivity was not described before this work.

(A few other groups have demonstrated this feasibility using different electrokinetic forces during the course of this thesis.) Enhanced protein binding was accomplished and sensor function was essentially unaffected by the modifications.

5.2.2 Contributions from CHAPTER 3: ENHANCEMENT OF HETEROGENEOUS IMMUNOASSAYS USING AC ELECTROOSMOSIS

(1) Enhancement of heterogeneous immunoassays using AC Electroosmosis

For the first time, AC electroosmosis was used to enhance a heterogeneous immunoassay. The quantity of bound antibody for a given incubation time was significantly increased by using AC electroosmosis. This advance could help to positively influence the translation of microfluidic test devices designed to detect small amounts of protein or other biological material. As far as the author knows, this is only the second time AC electrokinetics was used to stir protein assays.

(The first group to do so used the AC electrothermal effect during the course of this thesis work.)

Most of the previous work focused on the manipulation of large colloidal particles (greater than several hundred nm) that can be controlled much more easily.

(2) Development of a novel predictive model

The development of a novel predictive finite element model describing the effects of AC electroosmosis on heterogeneous immunoassays was also described in CHAPTER 3: ENHANCEMENT OF HETEROGENEOUS IMMUNOASSAYS USING AC ELECTROOSMOSIS. This model provides information about reaction kinetics under a wide variety of circumstances. It can be used to predict how effective the mixing is and which types of reactions can be enhanced.

(3) Optimization of parameters using experiments and a finite element model

Using fluorescent antibody binding experiments and the finite element model, an optimization scheme was conducted to determine optimum operational and system parameters for effective stirring of heterogeneous immunoassays. An optimization scheme was carried out using the finite element model in order to determine the best electrode geometry, which was discovered to scale with chamber height. Furthermore, a description of how the system changes based on frequency and voltage parameters was undertaken experimentally in order to find the most efficient electrical signal to enhance antibody binding. These are all new findings which are important for the successful development of new sensor and microfluidic platforms for protein detection.

(4) Discovered evidence of the presence of DEP

An unexpected finding from this work was the strong evidence for the capability of DEP to influence antibody binding. It is generally understood from scaling analysis, that the DEP force acting on such small particles as proteins should be non-deterministic due to the effects of thermal randomization. However, strong evidence for its presence in manipulating antibodies was discovered during the course of this thesis work and presented in CHAPTER 3: ENHANCEMENT OF HETEROGENEOUS IMMUNOASSAYS USING AC ELECTROOSMOSIS.

5.2.3 Contributions from CHAPTER 4: IMPROVED PROTEIN DETECTION ON AN AC ELECTROKINETIC QUARTZ CRYSTAL MICROBALANCE

(1) Successful modification of a sensor equipped with AC electrokinetic device

In CHAPTER 4: IMPROVED PROTEIN DETECTION ON AN AC ELECTROKINETIC QUARTZ CRYSTAL MICROBALANCE, the successful modification of a quartz crystal microbalance to be able to perform AC electrokinetic actuation in addition to its normal sensing

functions was shown. This novel sensor maintained an excellent quality factor and its basic sensing function was essentially unaffected by the modification. (In fact, its sensitivity to viscosity was improved by this modification.) The QCM was used as a test sensor and using the methods described in this chapter, a researcher may similarly modify any number of sensors to be able to perform dual functions as well.

(2) *Demonstration of the ability to use AC electrokinetics on fully functionalized heterogeneous immunoassays*

In order for AC electroosmosis to be useful for biological assays, the ability to perform fully functionalized heterogeneous immunoassays is important. This ability was demonstrated in CHAPTER 4:IMPROVED PROTEIN DETECTION ON AN AC ELECTROKINETIC QUARTZ CRYSTAL MICROBALANCE as well and is not present in the current literature. AC Electroosmosis was used independently in different stages of heterogeneous immunoassays and accompanied by many different negative controls. It was shown that AC electroosmosis did not significantly increase nonspecific binding and that the assay could be safely enhanced during the primary antibody binding or the secondary antibody binding.

(3) *Improved detection of IgG on a sensor using AC electrokinetics*

The major goal of this thesis was to determine if AC electrokinetics could be used to enhance a protein assay on a biosensor. This was demonstrated conclusively and for the first time during this thesis and is described in CHAPTER 4:IMPROVED PROTEIN DETECTION ON AN AC ELECTROKINETIC QUARTZ CRYSTAL MICROBALANCE. Protein enhancement was carried out using AC electrokinetic mixing on a novel biosensor which was corroborated using two independent means – a protein quantification assay and fluorescent imaging.

5.3 Future work

Future areas of exploration pertaining to this work fall under three broad categories; (1) improvements to modeling and predictive tools; (2) Exploration of the protein patterning effects; and (3) Sensor and application-driven development.

5.3.1 Improvements to modeling and predictive tools

One of the main shortcomings of the modeling work presented in this thesis was that the presence of the particle was not considered to affect the electric field. The consideration of this effect may help explain some particle behaviors more thoroughly, for example, assembly-lining and particle-particle interactions, which are currently not well understood by the research community. Since AC electrokinetics comes about due to nonuniformities in the electric field, it stands to reason that the presence of particles, which have different electrical properties than the surrounding media, will themselves cause micro- and nano- perturbations of the electric field. These minute nonuniformities will be a secondary source for AC electrokinetics. Perhaps an in-depth study of these effects and inclusion into future models would help explain some of the particle-particle interactions observed – for example, particle chaining and the regular spacing of assembly-lined particles seen at low particle concentrations. Another hypothesis is that the electric field perturbations that exist around a particle very close to the center of an interdigitated electrode causes a positive DEP force which is the true source of assembly-lining. All of these hypotheses can be tested with proper simulation techniques.

Another shortcoming of the modeling work is an inability to predict some AC electrokinetics on more complicated geometries. Simulations are currently limited to a 2D space because the ACEO effect is not well enough understood to be included as more than a 2D boundary condition. In other words, there is no theoretical formula that describes this phenomenon on

complex electrode geometries that would require 3D modeling approaches. A fundamental approach using more basic principles may be successfully applied to explaining ACEO. This tactic might yield better results that can be applied to a 3D space.

5.3.2 Exploration of the protein patterning effects

An unexpected outcome of this research was the fact that protein, under the presence of AC electrokinetic effects, becomes patterned (i.e. along the electrode edges). Our current theoretical understanding of these phenomena indicates that this should not be possible for such small particles as antibodies (12 nm in their largest dimension). Thermal randomization effects should counter the concentrating effects of DEP.

There is another patterning effect - the finger end-effect, which causes high concentration near the electrode ends. This may not necessarily be contrary to our theoretical understanding – at least in part. The end effect probably occurs partially due to the fact that the electrokinetic forces can reach past the end of the electrode finger and have ‘free access’ to the analyte that exists there. This hypothesis also has need of testing more extensively. For example, a series of experiments may be carried out by controlling the geometrical space beyond the electrode fingers. A channel may be aligned such that a carefully controlled distance exists between the end of the electrode and the edge of the channel. By increasing or decreasing this distance, the end effect should be positively or negatively affected respectively. This end-effect causes the most dramatic concentration enhancement and might be leveraged successfully for sensors that can operate on microscopic regions (microcantilevers, laser fluorescence, etc...)

5.3.3 Other means of micromixing

The primary AC electrokinetic phenomenon studied was ACEO. The main limitation of ACEO is that it is relegated to solutions with very low conductivities which are therefore not

physiologically relevant. The other electro-hydrodynamic force is the electrothermal effect which, though it has been looked at as a means of improving assay enhancement already, has still undergone comparatively little research. Modification of a sensor with an electrothermal effect device has, as far as the author is aware, not been accomplished yet and is recommended for future work. Some difficulty arises in the fact that the electrothermal effect has, so far, only been produced in microsystems made from silicon substrates, which are required due to its high thermal conductivity. This high thermal conductivity helps to create the strong temperature gradients required. It may not be easy to produce the same effect on many sensor types – for example, ones made from quartz as was used in this research. Furthermore, the electrothermal effect may require a temperature controlling system, such as a Peltier device for extended activation times.

DC electroosmosis (EO) is also a viable option. EO is capable of operating in buffered solution. Typically EO is used to generate flow along the length of a channel but recent work by Lynn et al [33] has shown the capability to do transverse mixing in a channel by using this effect with cleverly placed electrodes.

Acoustic methods described in Section 1.4.8(2) (page 30) may also be used in conjunction with fluorescent assays, although it might be difficult to apply these to biosensors, which may be adversely affected by coupling to a piezoelectric device.

5.3.4 Sensor and application-driven development

A true biosensor performs real-time sensing on a functionalized surface. The sensor results reported, however, were not real-time, but a before and after measurement and the detection surface was not functionalized. The former shortcoming was due to sensitivity of the QCM, which was not able to take accurate measurements of such small concentrations in an aqueous

environment. The inability to perform experiments on functionalized surfaces was for practical reasons. Modifying the sensors in a small university facility was expensive and time consuming. A fabrication success rate of about 20% was due to the extreme fragility of the thin quartz wafers and the many different steps required to perform successful fabrication. A higher success rate would have meant more sensors available on which to perform experiments. Performing a full immunoassay with the many different types of controls and samples was not feasible with the equipment and techniques available. This experimental work is important, but left for future researchers.

So far, results were only presented on modified quartz crystal microbalances. There are a wide variety of biosensors that might benefit from modification with AC electrokinetic devices. Perhaps the most obvious case is that of electrochemical sensors. Electrochemical impedance spectroscopy has been used as a sensing technique and the electrodes used for spectroscopy may also serve the dual-purpose of performing active mixing as well. Almost every sensor category has device types that may benefit from modification as well. The main limitations are that the electrokinetic device does not inhibit normal sensor operation and that the reaction is transport-rate limited rather than reaction-rate limited. Strong electric fields may sometimes affect sensor performance – for example, on piezoelectric transducers. The presence of the electrodes themselves may also inhibit sensor performance although electrodes can be made optically transparent with indium tin oxide (ITO) films.

The different AC electrokinetic phenomena may be intelligently employed in a multi-step whole-assay microfluidic biosensor. A combination of effects may be used for different parts of the assay to gain the best enhancement. For example, the biosensor surfaces may be more effectively functionalized by using ACEO or ETE. Capturing of larger antigen particles (viruses or bacteria)

can be carried out with DEP. Labeling steps can be carried out with any of the effects depending on the labeling technique.

Another unsolved mystery is that of the electrode damage that occurs at low frequencies, high voltages and is somehow enhanced by the presence of antibodies. An electrode was severely damaged and studied with several different imaging modalities (Figure 4-6). Still, even with these investigative efforts, the cause of the damage remains elusive.

REFERENCES

1. Lei, K.F. and Y.K.C. Butt, *Colorimetric immunoassay chip based on gold nanoparticles and gold enhancement*. *Microfluidics and Nanofluidics*, 2010. **8**(1): p. 131-137.
2. Watanabe, E., et al., Immunoassay based on a polyclonal antibody for sex steroid hormones produced by a heterogeneous hapten-conjugated immunogen: Estimation of its potentiality and antibody characteristics. *Analytica Chimica Acta*, 2010. **658**(1): p. 56-62.
3. Zimmermann, M., et al., Modeling and optimization of high-sensitivity, low-volume microfluidic-based surface immunoassays. *Biomedical Microdevices*, 2005. **7**(2): p. 99-110.
4. Luong, J.H.T., K.B. Male, and J.D. Glennon, *Biosensor technology: Technology push versus market pull*. *Biotechnology Advances*. **26**(5): p. 492-500.
5. Rasooly, A., *Biosensor technologies*. *Methods*, 2005. **37**(1): p. 1-3.
6. Rotman, D., *Shoveling Water: Why does it take so long to commercialize new technologies*, in *Technology Review*. 2010.
7. Fatoyinbo, H.O., et al., An integrated dielectrophoretic quartz crystal microbalance (DEP-QCM) device for rapid biosensing applications. *Biosensors and Bioelectronics*, 2007. **23**(2): p. 225-232.
8. Wu, J., N. Islam, and M. Lian. *High sensitivity particle detection by biased AC electroosmotic trapping on cantilever*. 2006. Istanbul, Turkey: Institute of Electrical and Electronics Engineers Inc.
9. Schuck, P., Kinetics of ligand binding to receptor immobilized in a polymer matrix, as detected with an evanescent wave biosensor. I. A computer simulation of the influence of mass transport. *Biophysical Journal*, 1996. **70**(Copyright 1996, IEE): p. 1230-49.
10. Hu, G., Y. Gao, and D. Li, *Modeling micropatterned antigen-antibody binding kinetics in a microfluidic chip*. *Biosensors and Bioelectronics*, 2007. **22**(7): p. 1403-1409.
11. Goldstein, B. and M. Dembo, Approximating the effects of diffusion on reversible reactions at the cell surface: ligand-receptor kinetics. *Biophys J*, 1995. **68**(4): p. 1222-30.
12. Sikavitsas, V.I., et al. Studies of transport limitations in the dextran layer of the BIACORE optical biosensor. in *Proceedings of the First Joint BMES/EMBS Conference*, 13-16 Oct. 1999. 1999. Piscataway, NJ, USA: IEEE.
13. Zwanzig, R. and A. Szabo, Time dependent rate of diffusion-influenced ligand binding to receptors on cell surfaces. *Biophys J*, 1991. **60**(3): p. 671-8.
14. Glaser, R.W., Antigen-antibody binding and mass transport by convection and diffusion to a surface: a two-dimensional computer model of binding and dissociation kinetics. *Anal Biochem*, 1993. **213**(1): p. 152-61.
15. Karlsson, R., A. Michaelsson, and L. Mattsson, Kinetic analysis of monoclonal antibody-antigen interactions with a new biosensor based analytical system. *J Immunol Methods*, 1991. **145**(1-2): p. 229-40.
16. Sell, S., *Immunology, Immunopathology, and Immunity*. 6 ed. 2001, Washington DC: ASM press.
17. Borisov, S.M. and O.S. Wolfbeis, *Optical Biosensors*. *Chemical Reviews*, 2008. **108**(2): p. 423-461.

18. Yalow, R.S. and S.A. Berson, *Immunoassay of endogenous plasma insulin in man*. 1960. *Obes Res*, 1996. **4**(6): p. 583-600.
19. Kuby, J., *Immunology*. 3rd ed. 1997, New York: W.H. Freeman and Company.
20. Haeberle, S. and R. Zengerle, *Microfluidic platforms for lab-on-a-chip applications*. *Lab on a Chip*, 2007. **7**(9): p. 1094-1110.
21. Terry, S.C., J.H. Jerman, and J.B. Angell, *A gas chromatographic air analyzer fabricated on a silicon wafer*. *Electron Devices, IEEE Transactions on*, 1979. **26**(12): p. 1880-1886.
22. Pohl, H.A., *The motion and precipitation of suspensoids in divergent electric fields*. *Journal of Applied Physics*, 1951. **22**(Copyright 2004, IEE): p. 869-871.
23. Pohl, H.A., *Some effects of nonuniform fields on dielectrics*. *Journal of Applied Physics*, 1958. **29**(8): p. 1182-1188.
24. Bakewell, D.J. and H. Morgan, *Dielectrophoresis of DNA: time- and frequency-dependent collections on microelectrodes*. *NanoBioscience, IEEE Transactions on*, 2006. **5**(1): p. 1-8.
25. Hoeb, M., et al., *Light-induced dielectrophoretic manipulation of DNA*. *Biophysical Journal*, 2007. **93**(3): p. 1032-8.
26. Green, N.G., et al., *Electrothermally induced fluid flow on microelectrodes*. *Journal of Electrostatics*, 2001. **53**(2): p. 71-87.
27. Kuan-Rong, H., et al., *Simulation on binding efficiency of immunoassay for a biosensor with applying electrothermal effect*. *Journal of Applied Physics*, 2008. **104**(6): p. 064702 (11 pp.).
28. Thomas, R.S., H. Morgan, and N.G. Green, *Negative DEP traps for single cell immobilisation*. *Lab on a Chip*, 2009. **9**(11): p. 1534-1540.
29. Brown, A.B.D., C.G. Smith, and A.R. Rennie, *Pumping of water with ac electric fields applied to asymmetric pairs of microelectrodes*. *Physical Review E (Statistical Physics, Plasmas, Fluids, and Related Interdisciplinary Topics)*, 2001. **63**(Copyright 2001, IEE): p. 016305-1.
30. Burch, D. and M.Z. Bazant, *Design principle for improved three-dimensional ac electro-osmotic pumps*. *Physical Review E*, 2008. **77**(Copyright (C) 2010 The American Physical Society): p. 055303.
31. Chang, C.-C. and R.-J. Yang, *Electrokinetic mixing in microfluidic systems*. *Microfluidics and Nanofluidics*, 2007. **3**(5): p. 501-525.
32. Hessel, V., H. Lowe, and F. Schonfeld, *Micromixers - A review on passive and active mixing principles*. *Chemical Engineering Science*, 2005. **60**(8-9 SPEC. ISS.): p. 2479-2501.
33. Lynn, N.S., C.S. Henry, and D.S. Dandy, *Microfluidic mixing via transverse electrokinetic effects in a planar microchannel*. *Microfluidics and Nanofluidics*, 2008. **5**(4): p. 493-505.
34. Leu, T.S. and F.C. Ma, *Novel EHD-pump driven micro mixers*. *Journal of Mechanics*, 2005. **21**(3): p. 137-144.
35. Yi-Kuen, L., et al. *Chaotic mixing in electrokinetically and pressure driven micro flows*. in *Micro Electro Mechanical Systems*, 2001. MEMS 2001. The 14th IEEE International Conference on. 2001.

36. Deval, J., P. Tabeling, and H. Chih-Ming. A dielectrophoretic chaotic mixer. in Micro Electro Mechanical Systems, 2002. The Fifteenth IEEE International Conference on. 2002.
37. Sigurdson, M., W. Dazhi, and C.D. Meinhart, *Electrothermal stirring for heterogeneous immunoassays*. Lab on a Chip, 2005. **5**(12): p. 1366-73.
38. Feidman, H.C., M. Sigurdson, and C.D. Meinhart, *AC electrothermal enhancement of heterogeneous assays in microfluidics*. Lab on a Chip, 2007. **7**(11): p. 1553-9.
39. Vivek, V. and K. Eun Sok. *Novel acoustic-wave micromixer*. 2000. Piscataway, NJ, USA: IEEE.
40. Hongyu, Y., K. Jae Wan, and K. Eun Sok, *Microfluidic mixer and transporter based on PZT self-focusing acoustic transducers*. Journal of Microelectromechanical Systems, 2006. **15**(4): p. 1015-24.
41. Jang, L.-S., et al., *Resonant mode-hopping micromixing*. Sensors and Actuators A: Physical, 2007. **138**(1): p. 179-186.
42. Sritharan, K., et al., *Acoustic mixing at low Reynold's numbers*. Applied Physics Letters, 2006. **88**(5): p. 054102-3.
43. Liu, R.H., R. Lenigk, and P. Grodzinski, *Acoustic micromixer for enhancement of DNA biochip systems*. Journal of Microlithography, Microfabrication, and Microsystems, 2003. **2**(3): p. 178-184.
44. Liu, R.H., et al. Acoustic microstreaming for biological sample mixing enhancement. in Microtechnologies in Medicine & Biology 2nd Annual International IEEE-EMB Special Topic Conference on. 2002.
45. Liu, R.H., et al., *Bubble-induced acoustic micromixing*. Lab on a Chip, 2002. **2**(3): p. 151-7.
46. Suzuki, H., H. Chih-Ming, and N. Kasagi, *A chaotic mixer for magnetic bead-based micro cell sorter*. Microelectromechanical Systems, Journal of, 2004. **13**(5): p. 779-790.
47. Kee Suk, R., et al., Micro magnetic stir-bar mixer integrated with parylene microfluidic channels. Lab on a Chip, 2004. **4**(6): p. 608-13.
48. Sauerbrey, G., Use of quartz vibrator for weighing thin layers and as a micro-balance. Zeitschrift fur Physik, 1959. **155**(2): p. 206-222.
49. Mehta, N., The Development of a Portable Electronic System (PES) for Piezoelectric Biosensors, in School of Biomedical Engineering, Science & Health Systems. 2007, Drexel: Philadelphia. p. 85.
50. Auge, J., et al., *Quartz crystal microbalance sensor in liquids*. Sensors and Actuators B: Chemical, 1994. **19**(1-3): p. 518-522.
51. Reed, C.E., K.K. Kanazawa, and J.H. Kaufman, *Physical description of a viscoelastically loaded AT-cut quartz resonator*. Journal of Applied Physics, 1990. **68**(5): p. 1993-2001.
52. Pohl, H.A., *Dielectrophoresis*. 1978, Cambridge: Cambridge University Press.
53. Ramos, A., et al., *Ac electrokinetics: a review of forces in microelectrode structures*. J.PhysD.: Appl. Phys., 1998. **31**: p. 2338-2353
54. Morgan, N.G.G.a.H., Separation of submicrometre particles using a combination of dielectrophoretic and electrohydrodynamic forces. J. Phys. D: Appl. Phys., 1998. **31**: p. L25-30

55. Green, N.G. and H. Morgan, *Dielectrophoretic separation of nano-particles*. Journal of Physics D: Applied Physics, 1997. **30**: p. L41-L84.
56. Hywel Morgan, a.N.G.G., *AC Electrokinetics: colloids and nanoparticles*. 2002 England: SRP Ltd.
57. Vykoukal, P.R.C.G.a.J., *Particle separation by dielectrophoresis*. Electrophoresis, 2002. **23**: p. 1973-1983
58. Morgan, N.G.G.a.H., *Dielectrophoretic investigations of sub-micrometre latex spheres*. J. Phys. D: Appl. Phys., 1997. **30**: p. 2626
59. Voldman, A.R.a.J., *Dielectrophoretic Traps for Single-particle Patterning*. Biophysical Journal, 2005. **88**: p. 2193-2205
60. Bunthawin, P.W.a.S., *Determination of Cell Dielectric Properties Using Dielectrophoretic Technique*. ScienceAsia, 2002. **28**: p. 113-119
61. M. Riegelman, H.L., and H. H. Bau, *Controlled Nanoassembly and Construction of Nanofluidic Devices*. J. Fluids Engineering, 2006. **128**: p. 6-13
62. Jones, T.B., *Electromechanics of Particles*. 1995 New York: Cambridge University Press.
63. Adam Rosenthal, B.M.T., Joel Voldman, *Quantitative modeling of dielectrophoretic traps*. Lab Chip, 2006. **6**(): p. 508-515.
64. Liu, Y., et al., *Dielectrophoretic Assembly of Nanowires*. Journal of Physical Chemistry B, 2006. **110**: p. 14098-14106.
65. Green, N.G., et al., *Fluid flow induced by nonuniform ac electric fields in electrolytes in microelectrodes. I. Experimental measurements*. Physical Review E, 2000. **61**: p. 4011-4018.
66. Castellanos, A., et al., *Electrohydrodynamics and dielectrophoresis in Microsystems: scaling laws*. J. Phys. D: Appl. Phys., 2003. **36**: p. 2584-2597
67. Andre Belisle, M.B., Ted Hubbard, and Marek Kujath, *Microelectrode arrays for two-dimensional polar movement of microparticles in water*. J. Vac. Sci. Technol. A, 2006. **24**: p. 737-741
68. Huang, S., et al., *AC electroosmotic generated in-plane microvortices for stationary or continuous fluid mixing*. Sensors and Actuators B, 2007. **125**: p. 326-336.
69. Jacobson, S., T. McKnight, and J. Ramsey, *Microfluidic devices for electrokinetically driven parallel and serial mixing*. Analytical Chemistry, 1999. **71**: p. 4455-4459.
70. Sigurdson, M., D. Wang, and C.D. Meinhart, *Electrothermal stirring for heterogeneous immunoassays*. Lab on aChip, 2005. **5**: p. 1366 - 1373
71. Dazhi Wang, M.S., and Carl D. Meinhart, *Experimental analysis of particle and fluid motion in ac electrokinetics*. Experiments in Fluids, 2005. **38**: p. 1-10
72. Li, P., Shi, K., Liu, Z., *Manipulation and spectroscopy of a single particle by use of white-light optical tweezers*. Optics Letters, 2005. **30**(2): p. 156-158
73. Ashkin, A., *History of optical trapping and manipulation of small-neutral particle, atoms, and molecules*. IEEE Journal on Selected Topics in Quantum Electronics, 2000. **6**(6): p. 841-856
74. Blideran, M.M., et al., *Mechanically actuated silicon microgripper for handling micro- and nanoparticles*. Microelectronic Engineering, 2006. **83**: p. 1382-1385.

75. Thelander, C.a.S., L. , AFM manipulation of carbon nanotubes: Realization of ultra-fine nanoelectrodes. *Nanotechnology*, 2002. **13**(1): p. 108-113
76. Ramachandran, T.R., Baur, C., Bugacov, A., Madhukar, A., Koel, B.E., Requicha, A., Gazen, C. , *Direct and controlled manipulation of nanometer-sized particles using the non-contact atomic force microscope*. *Nanotechnology*, 1998. **9**(3): p. 237-245
77. Takekawa, T., Nakagawa, K., Hashiguchi, G. , The AFM tweezers: Integration of a tweezers function with an AFM probe, in *TRANSDUCERS '05 - 13th International Conference on Solid-State Sensors and Actuators and Microsystems*. 2005.
78. Hywel Morgan, a.N.G.G., *AC Electrokinetics: colloids and nanoparticles*. 2002, England: SRP Ltd.
79. John Paul Urbanski, T.T., Jeremy A. Levitan, and Martin Z. Bazant, *Fast ac electro-osmotic micropumps with nonplanar electrodes*. *Appl.Phys. Lett.*, 2006. **89**: p. 143508
80. D.R.Lide, *CRC Handbook of Chemistry and Physics*. 81st edn ed. 2000 New York: CRC Press.
81. Beumer, T., P. Haarbosch, and W. Carpay, Convection during incubation of microplate solid phase immunoassay: Effects on assay response and variation. *Analytical Chemistry*, 1996. **68**(8): p. 1375-1380.
82. Bange, A., H.B. Halsall, and W.R. Heineman, *Microfluidic immunosensor systems*. *Biosensors and Bioelectronics*, 2005. **20**(12): p. 2488-2503.
83. Ali, Z., *Lab-on-a-chip for terrorist weapons management*. *Measurement and Control*, 2005. **38**(3): p. 87-91.
84. Wang, J., *Microchip devices for detecting terrorist weapons*. *Analytica Chimica Acta*, 2004. **507**(1): p. 3-10.
85. Bogue, R., *MEMS sensors: past, present and future*. *Sensor Review*, 2007. **27**(1): p. 7.
86. Owen, V.M., *Biosensors - The Needs of the Healthcare Market*. *Sensor Review*, 1993. **13**(4): p. 3.
87. Wojciechowski, P.W. and J.L. Brash, Computer simulation for the study of macromolecular adsorption with special applications to single-component protein adsorption. *Journal of Colloid and Interface Science*, 1990. **140**(1): p. 239-252.
88. Lionello, A., et al., Protein adsorption in static microsystems: effect of the surface to volume ratio. *Lab on a Chip*, 2005. **5**(3): p. 254-260.
89. Vijayendran, R.A., F.S. Ligler, and D.E. Leckband, *A computational reaction-diffusion model for the analysis of transport-limited kinetics*. *Analytical Chemistry*, 1999. **71**(23): p. 5405-5412.
90. Huang, K.-R., et al., Simulation on binding efficiency of immunoassay for a biosensor with applying electrothermal effect. *Journal of Applied Physics*, 2008. **104**(6): p. 064702-11.
91. Lifeng, Z., et al. Towards single molecule manipulation with dielectrophoresis using nanoelectrodes. 2003. Piscataway, NJ, USA: IEEE.
92. Hoettges, K.F., et al., *Optimizing particle collection for enhanced surface-based biosensors*. *IEEE Engineering in Medicine and Biology Magazine*, 2003. **22**(6): p. 68-74.
93. Morgan, H. and N. Green, *AC Electrokinetics: colloids and nanoparticles*. 2002, England: SRP Ltd.

94. Hart, R., et al., *AC Electrokinetic Phenomena Generated by Microelectrode Structures*. JoVe, 2008. **17**: p. <http://www.jove.com/index/details.stp?id=813>.
95. COMSOL MULTIPHYSICS User's Guide. 2008.
96. George, A.J., R.R. French, and M.J. Glennie, Measurement of kinetic binding constants of a panel of anti-saporin antibodies using a resonant mirror biosensor. *J Immunol Methods*, 1995. **183**(1): p. 51-63.
97. Oh, J., et al., Comprehensive analysis of particle motion under non-uniform AC electric fields in a microchannel. *Lab on a Chip*, 2008(9): p. 62-78.
98. Ueda, M., K. Yoshikawa, and M. Doi, Stretching of long DNA under alternating current electric fields in a concentrated polymer solution. *Polymer Journal*, 1997. **29**(12): p. 1040-1043.
99. Washizu, M., et al. *Molecular dielectrophoresis of bio-polymers*. 1992. New York, NY, USA: IEEE.
100. Sin, M.L.Y., et al., *Active manipulation of quantum dots using ac electrokinetics*. *Journal of Physical Chemistry C*, 2009. **113**(16): p. 6561-6565.
101. O'Sullivan, C.K. and G.G. Guilbault, *Commercial quartz crystal microbalances-theory and applications*. *Biosensors & Bioelectronics*, 1999. **14**(8-9): p. 663-70.
102. Michalzik, M., R. Wilke, and S. Buttgenbach, *Miniaturized QCM-based flow system for immunosensor application in liquid*. *Sensors and Actuators B (Chemical)*, 2005. **111-112**: p. 410-15.
103. Ricci, F., et al., A review on novel developments and applications of immunosensors in food analysis. *Analytica Chimica Acta*, 2007. **605**(2): p. 111-129.
104. Li, Y. and S. Xiao-Li, A QCM immunosensor for Salmonella detection with simultaneous measurements of resonant frequency and motional resistance. *Biosensors & Bioelectronics*, 2005. **21**(6): p. 840-8.
105. Su, X.L. and Y. Li, A self-assembled monolayer-based piezoelectric immunosensor for rapid detection of Escherichia coli O157:H7. *Biosensors & Bioelectronics*, 2004. **19**(6): p. 563-74.
106. Chen, S.-H., et al., A method of layer-by-layer gold nanoparticle hybridization in a quartz crystal microbalance DNA sensing system used to detect dengue virus. *Nanotechnology*, 2009. **20**(21).
107. Chunyan, Y., et al., *Hybridization assay of hepatitis B virus by QCM peptide nucleic acid biosensor*. *Biosensors and Bioelectronics*, 2008. **23**(Copyright 2008, The Institution of Engineering and Technology): p. 879-85.
108. Utenthaler, E., et al., Ultrasensitive quartz crystal microbalance sensors for detection of M13-Phages in liquids. *Biosensors and Bioelectronics*, 2001. **16**(9-12): p. 735-743.
109. Kurosawa, S., et al., Evaluation of a high-affinity QCM immunosensor using antibody fragmentation and 2-methacryloyloxyethyl phosphorylcholine (MPC) polymer. *Biosensors and Bioelectronics*, 2004. **20**(6): p. 1134-1139.
110. Park, I.-S., et al., Development of a direct-binding chloramphenicol sensor based on thiol or sulfide mediated self-assembled antibody monolayers. *Biosensors and Bioelectronics*, 2004. **19**(7): p. 667-674.
111. Rosenbaum, J., *Bulk Acoustic Wave Theory and Devices*. 1988, Boston: Artech House.

112. Granstaff, V.E. and S.J. Martin, Characterization of a thickness-shear mode quartz resonator with multiple nonpiezoelectric layers. *Journal of Applied Physics*, 1994. **75**(3): p. 1319-1329.
113. Bandey, H.L., et al., Modeling the Responses of Thickness-Shear Mode Resonators under Various Loading Conditions. *Analytical Chemistry*, 1999. **71**(11): p. 2205-2214.
114. Park, S. and A. Beskok, Alternating current electrokinetic motion of colloidal particles on interdigitated microelectrodes. *Analytical Chemistry*, 2008. **80**(8): p. 2832-2841.
115. Gervasio, A.P.G., et al., On-line electrolytic dissolution of alloys in flow injection analysis: Determination of iron, tungsten, molybdenum, vanadium and chromium in tool steels by inductively coupled plasma atomic emission spectrometry. *Analytica Chimica Acta*, 2000. **405**(1-2): p. 213-219.
116. Blideran, M.M., Bertsche, G., Henschel, W., Kern, D.P.A "Mechanically actuated silicon microgripper for handling micro- and nanoparticles" *Microelectronic Engineering*, 83(4-9) SPEC. ISS., *Mechanically actuated silicon microgripper for handling micro- and nanoparticles*. *Microelectronic Engineering*. **83**: p. 4-9.

APPENDIX I - AC ELECTROKINETIC QCM PROTOTYPES

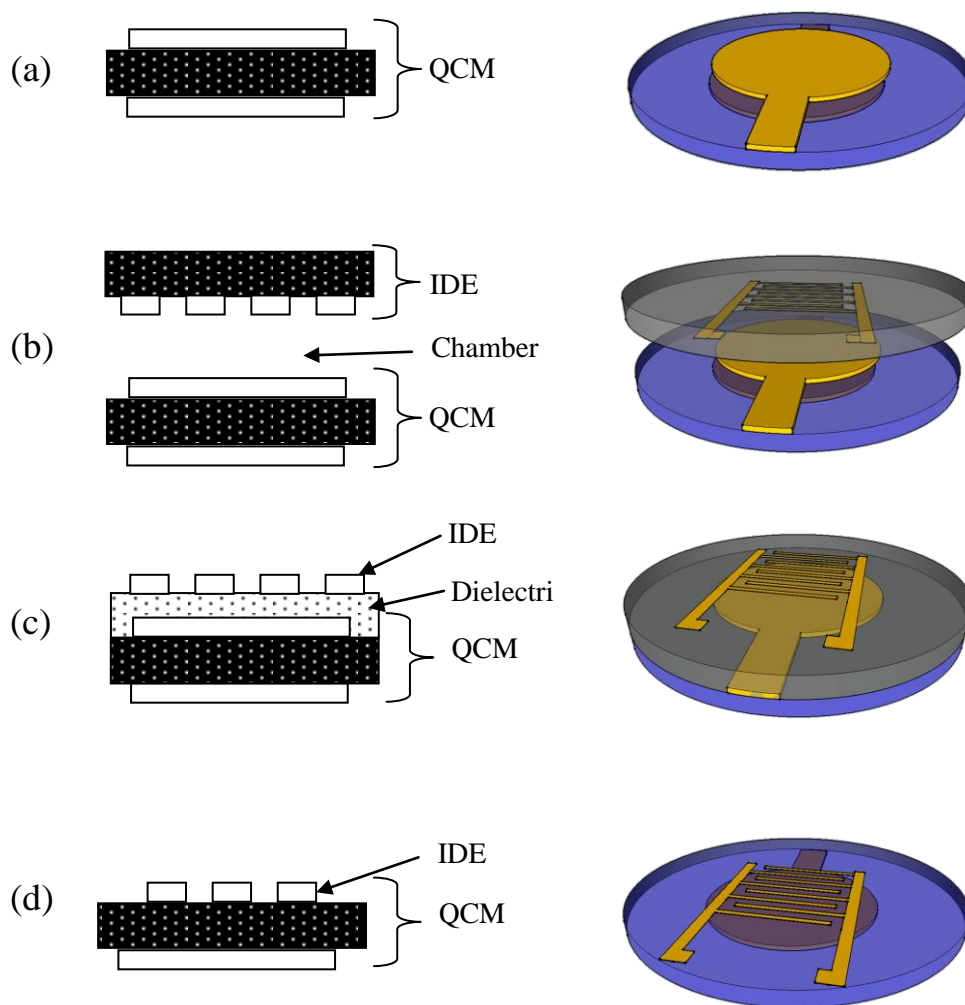


Figure 5-1: Different configurations for enhancing QCM binding with AC electrokinetics. (a) Depicts a standard QCM made from a piece of quartz with circular gold electrodes on either side. (b) Shows the first prototype which consisted of an IDE built on a glass substrate and placed in

close proximity to the QCM surface. (c) Consists of a QCM onto which a dielectric material (glass) was deposited. IDEs were then fabricated on the glass surface. (d) This is the final prototype and consists of a piece of quartz with an IDE on top and a circular electrode on bottom

Schematics of the different prototypes used throughout the research are shown in Figure I-1. Figure I-1(a) shows a regular QCM for comparison. The prototype depicted in (b) was an attempt to place a QCM in close proximity to an IDE electrode. The distance however, was not close enough to make an impact on the sensor. Later research would show that the distance needs to be well below the 1 mm thickness used for this chamber height. Prototype (c) consisted of a QCM with a dielectric material deposited on top of the surface. This was then followed by a set of IDEs fabricated on top. The dielectric material served to insulate the QCM from the IDE. The high field strengths provided to the IDE caused the dielectric material to break down and shorting occurred between the QCM and the IDEs. Prototype (d) was the final design and the device consisted of a QCM with the top electrode replaced with a set of IDEs. For more details about the operation of this QCM, see CHAPTER 4:IMPROVED PROTEIN DETECTION ON AN AC ELECTROKINETIC QUARTZ CRYSTAL MICROBALANCE. Fabrication details are described in APPENDIX II.

APPENDIX II - MICROFABRICATION TECHNIQUES

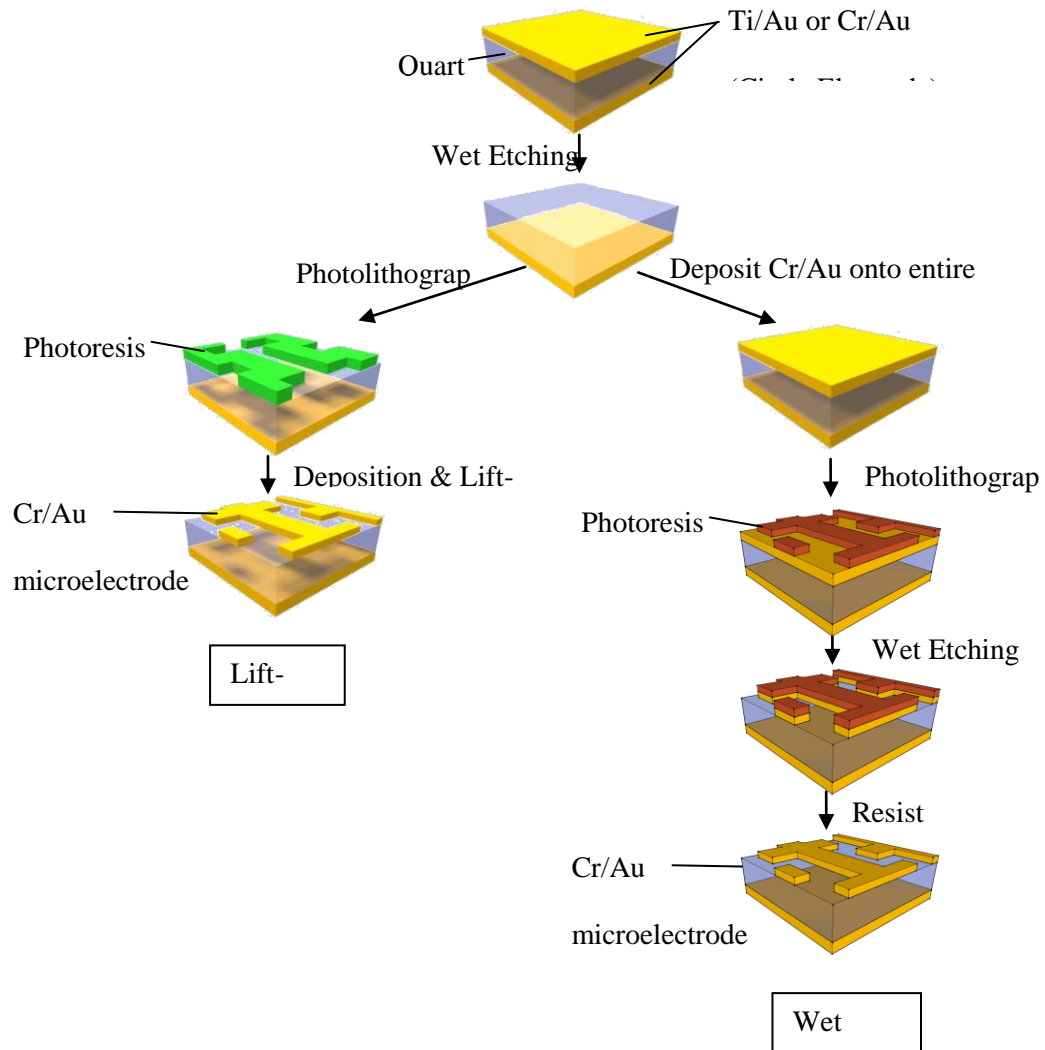


Figure 5-2: Schematic of the techniques used to fabricate EKQCMs. The left side shows the lift-off technique while the right shows the wet etch technique.

Two techniques were used to microfabricate the IDEs used to perform AC electrokinetics. For both techniques, the first step is to protect one of the gold electrodes with an adhesive, and then remove the top electrode which can consist of either Ti/Au or Cr/Au. Au is removed with Gold Etchant and Ti is removed with a low concentration of buffered oxide etchant (BOE). Cr is removed with Chromium mask etchant.

The lift-off technique used to modify a QCM is shown in Figure II-1(left). The next step is to perform photolithography to transfer the electrode pattern on the quartz surface. Next, a Cr/Au layer is deposited by thermal evaporation. Lift-off was performed by removing the photoresist using Acetone.

The wet-etch technique starts with a QCM with the top electrode removed. A Cr/Au layer is then deposited onto the entire surface of the QCM. Next, photolithography is performed with the opposite pattern as in the lift-off technique. Wet etching is then performed on the Au/Cr layers not protected by the photoresist. After the photoresist is removed, the electrodes are revealed.

APPENDIX III - FLUORESCENCE IMAGE ANALYSIS

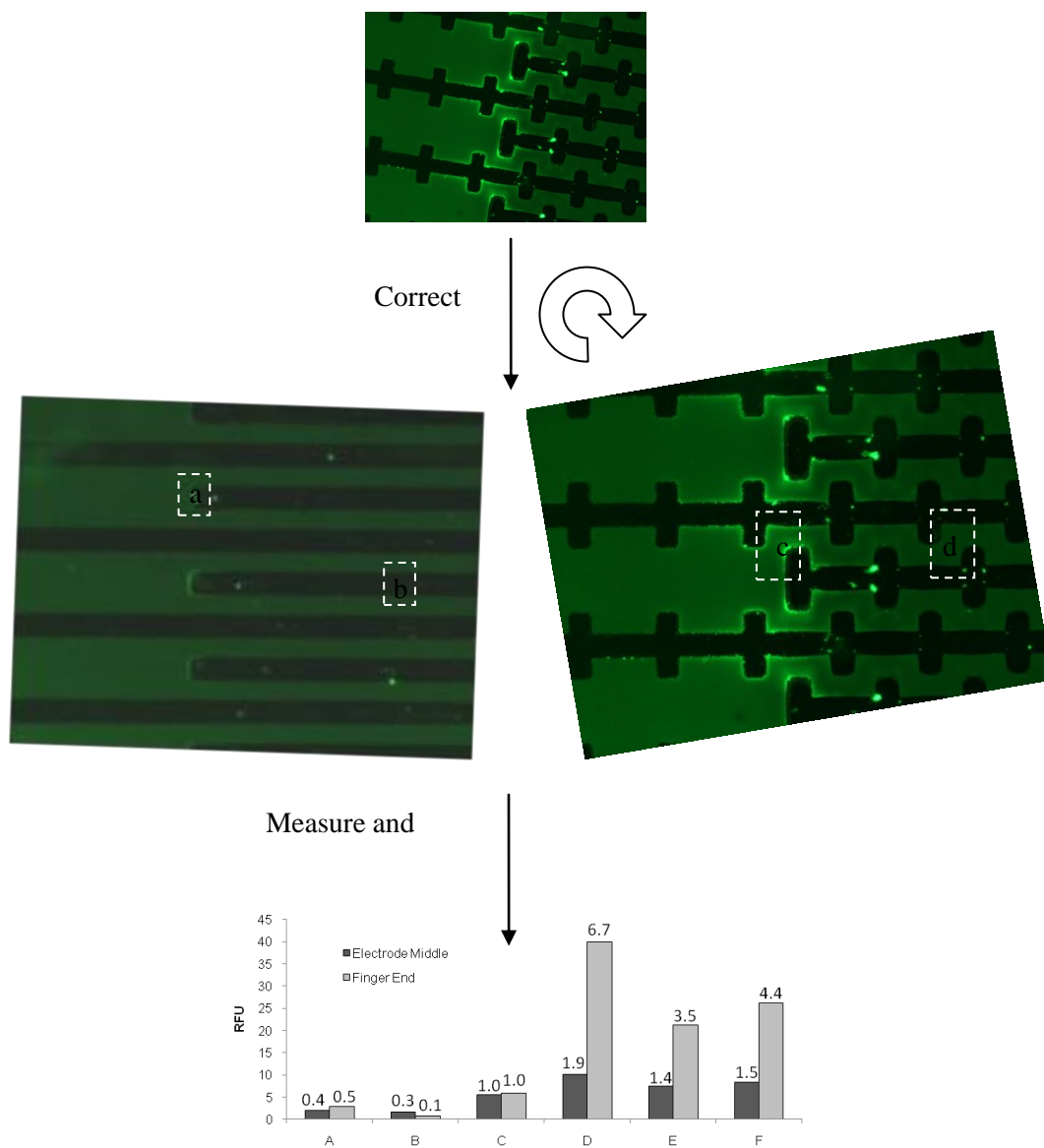


Figure 5-3: The fluorescent image analysis technique relies on measuring regions on the electrodes for intensity. ImageJ was used for this purpose and the left and right figures show measurement boxes for a parallel straight and castellated pattern respectively.

Image analysis performed on substrates with bound fluorescent antibodies was carried out using NIH ImageJ software. The measurement scheme consisted of the following steps.

For each image:

- Use the protractor tool to determine the angle of the electrodes with respect to the image.
- Rotate the image to compensate
- Draw a measurement window (shown in white broken lines)
- Measure the middle electrode region: For each image, use the same size measurement window and measure the middle electrodes (far away from the finger end) in three separate locations each (total of 10 measurements per image). Square 'b' is an example measurement window for the middle region.
- Measure the electrode finger ends: Use square 'a' to measure each of the electrode ends
- Remove background fluorescence by measuring a blank sample in the same manner. Blank readings for the finger end should be subtracted from the finger end sample measurements while blank readings for the middle of the blank should be subtracted from the middle sample measurements.

APPENDIX IV – INTER- AND INTRA-DEVICE BINDING VARIABILITY

The binding variability on interdigitated electrodes is shown qualitatively with several images below. Each group of four images was taken from a single device. Not only is there significant variation between images, but within a single image, there are bright regions and dark regions. This is true, even for images taken in the center of a device. The reasons for this variability are not understood but may be due to some device fabrication imperfections.

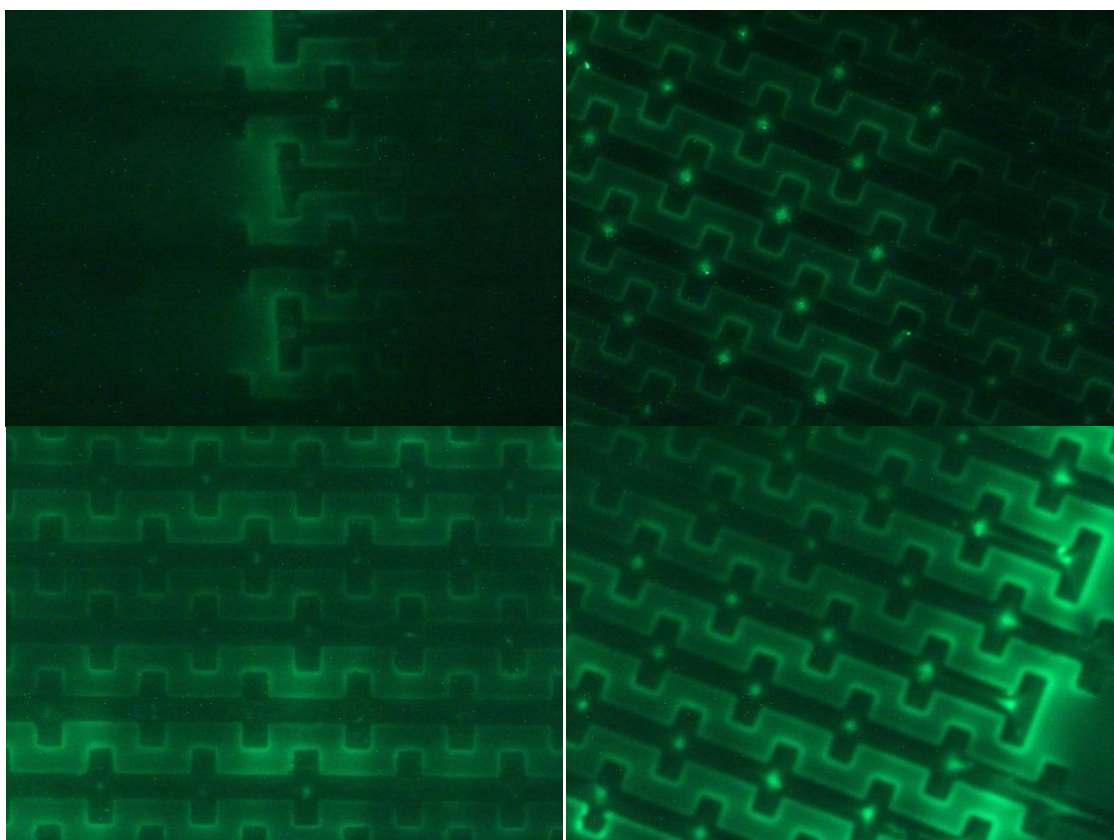


Figure 5-4: Images taken from sample 1

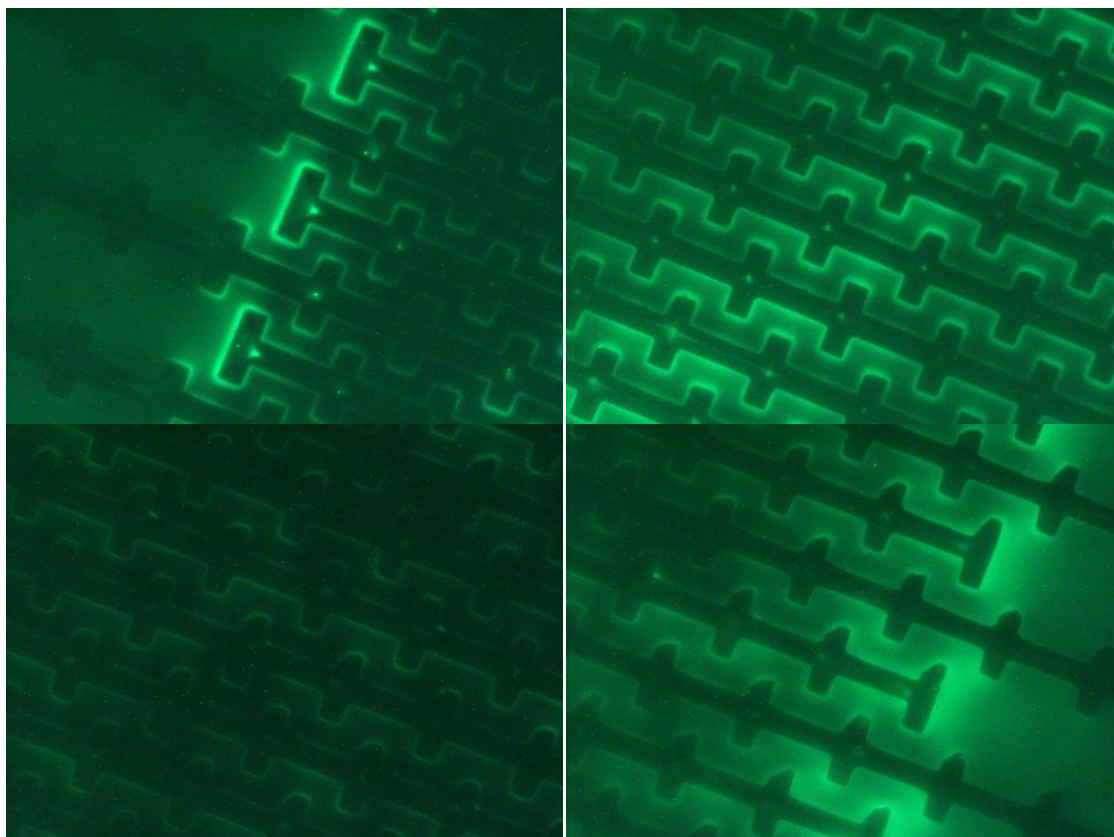


Figure 5-5: Images taken from sample 2 under the same conditions.

An interesting parallel can be drawn between the antibody binding pattern and the particle collection pattern seen with 2 μm polystyrene microspheres. The comparison is shown in Figure 5-6. Though particles will rapidly congregate at the electrode center due to ACEO and DEP, the particles eventually begin to migrate to form clusters in preferred areas. This clustering does not appear random and forms a larger pattern of clustered particles over a particular swath of the electrode. This may be due to electrodes which have a slightly smaller gap due to fabrication imperfections. By comparison, the fluorescent antibody brightness pattern also seems to occur across many electrodes in a similar swath.

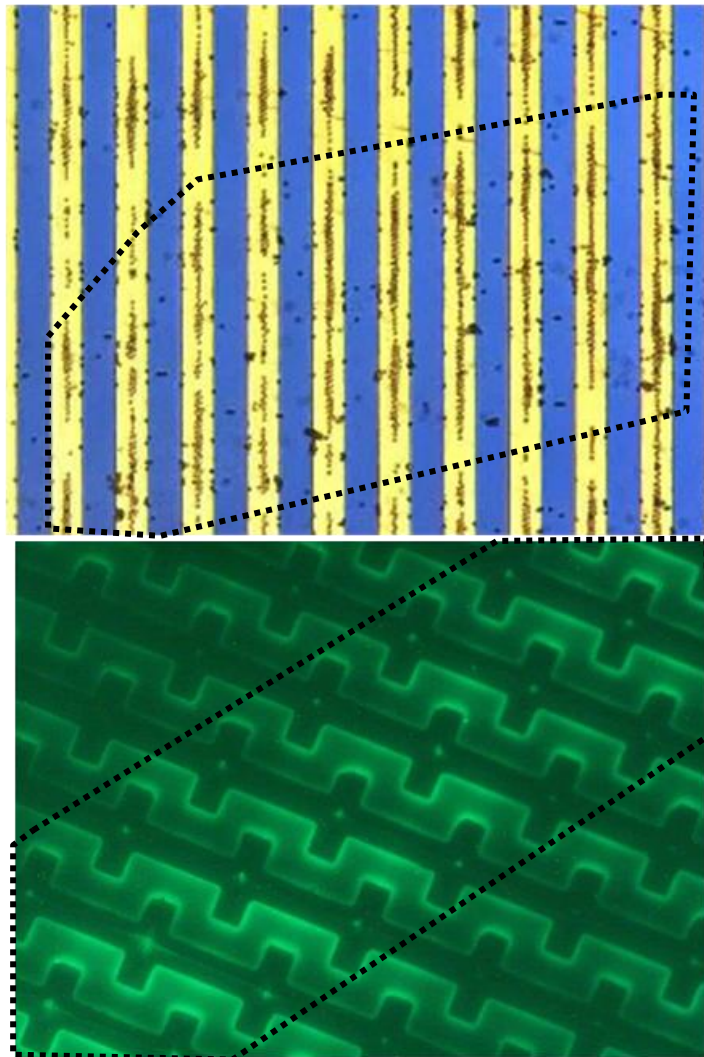


Figure 5-6: Comparison of particle collection and fluorescent antibody binding

APPENDIX V – RELATIVE BINDING CAPACITY OF NONSPECIFICALLY ADSORBED IGG ON GOLD AND GLASS

The relative binding capacities of gold and glass were tested by the following procedure. First, the glass and gold substrates were cleaned using the procedures described in 3.4.1 (1). Second, 0.1 mg/ml IgG was deposited on the surface of glass and gold for a 2 hour incubation at high humidity (to prevent evaporation). Third, fluorescent images were taken of each substrate. For each substrate, images were taken of a bound region and compared to a blank region. The innate fluorescence in the blank regions were subtracted from the sample regions and shown in Figure 5-7. The fluorescence of the glass was normalized against that of the gold (which will therefore have a value of 1). The glass substrate has a binding capacity almost 2.5 times greater than that of gold. However, it should be remembered that this procedure used nonspecific adsorption and each surface fictionalization method will result in different binding capacities. Furthermore, the fluorescence measurement method is not without problems. Quenching of fluorophores is possible and the presence of nearby gold could potentially affect the ability of the IgG to fluoresce.

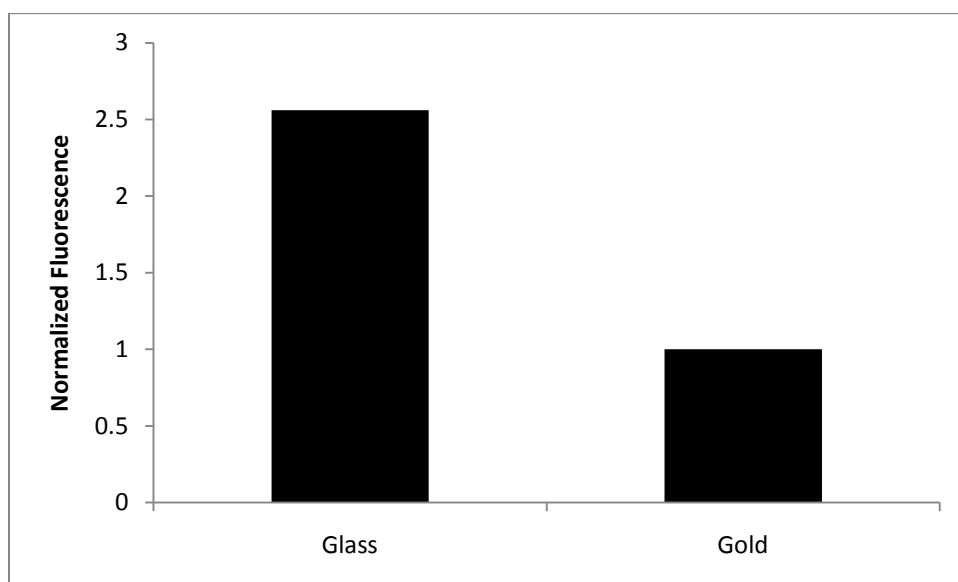


Figure 5-7: Relative binding capacity of a cleaned gold and glass surface

APPENDIX VI - FURTHER DISCUSSION ON THE POSSIBLE INFLUENCE OF DEP ON IGG BINDING

The ability of AC Electrokinetics to pattern antibodies on the surface of the interdigitated electrodes was an unexpected finding. It was only anticipated that the overall surface concentration would be greater as a result of using non-uniform electric fields and that the spatial distribution would be uniform. Such was not the case as indicated by the many fluorescent images taken of experiments throughout this investigation. The possibility that DEP unexpectedly plays a role in IgG binding is discussed in this Appendix.

First, the analysis in Figure IV-1 shows how the DEP and hydrodynamic forces scale with particle size. Hydrodynamic forces do not scale with particle size because the particles are dragged by the surrounding fluid. At low such Reynolds numbers, inertial effects may be ignored and particles can be considered to be moving exactly with the fluid (unless other forces interfere). DEP force, however, acts directly on the particle and can move it independently of the fluid. DEP force scales with particle volume (r^3) whereas Brownian motion scales with the square root of particle radius. Therefore, as the particle size decreases, the forces acting on the particle become non-deterministic because of the thermal randomization effects. This non-deterministic regime is indicated in grey in Figure IV-1. It appears that for a 10 nm microsphere, which is about the size of an antibody molecule, the DEP force is clearly non-deterministic by about two orders of magnitude. It is possible, however, that the IgG molecule does not behave like a polystyrene microsphere and might have a drastically different Clausius-Mossotti (CM) factor which affects the DEP force. DNA, for example, does not have a CM factor that is like a microsphere, and as a result, others have shown single DNA molecule manipulation.

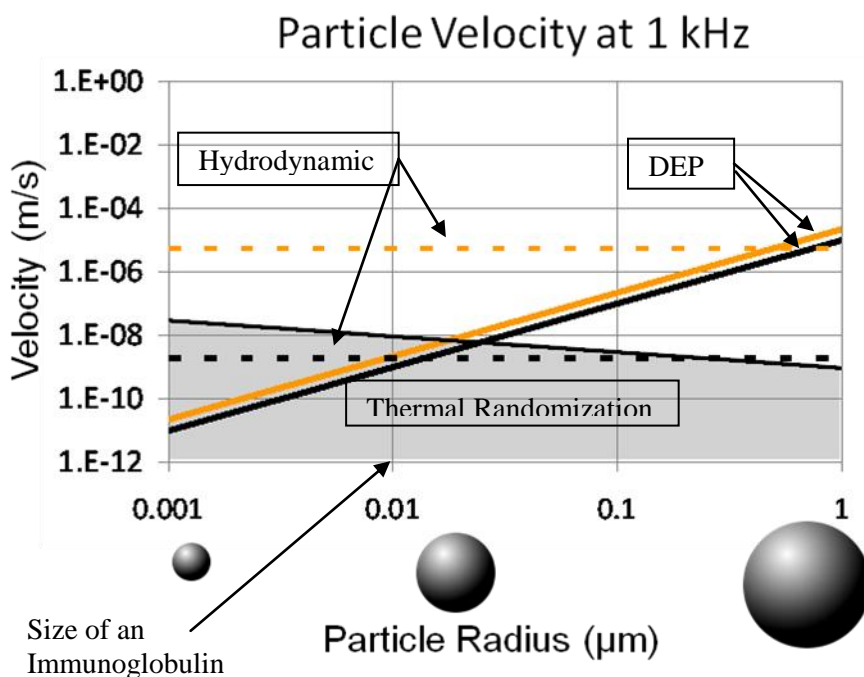


Figure 5-8: Scaling analysis of particle velocity separated by forces. Forces within the grey region are non-deterministic due to thermal randomization.

Two main ways to distinguish between DEP and ACEO are discussed, with respect to the question of IgG patterning. First, DEP and ACEO have dramatically different frequency dependencies. Second, the distribution of DEP force and ACEO force vary as well. As shown in Figure IV-2, ACEO force with respect to frequency changes dramatically with a peak value near 200 Hz and dying out almost completely at a few tens of kHz. DEP force, on the other hand is expected to be mostly constant in this frequency range. This frequency dependence on the improvement gained with fluorescent IgG deposition follows that of ACEO, rather than DEP. Furthermore, application of only high frequency signals where DEP dominates and ACEO is virtually nonexistent shows no antibody patterning.

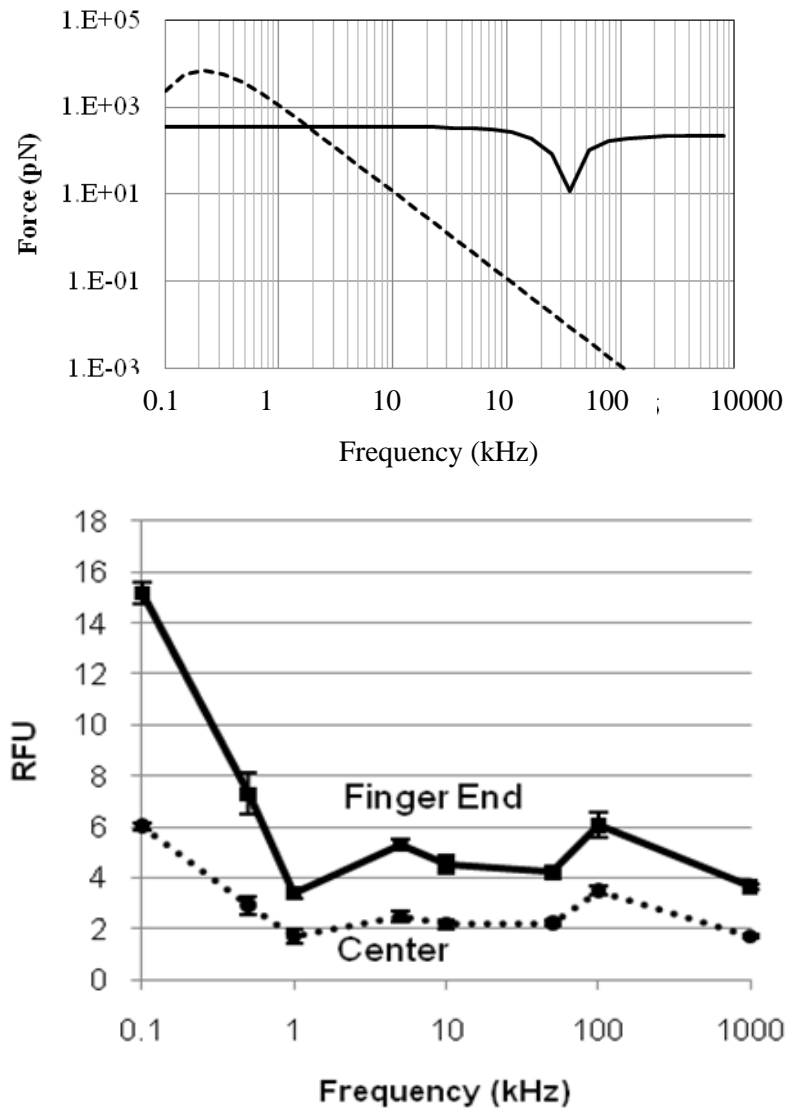


Figure 5-9: Frequency dependence of ACEO and DEP according to Theoretical prediction (top) and experimental frequency dependence of antibody capture enhancement via fluorescent imaging analysis.

It seems, therefore, ACEO must be the dominant effect. However, a simulation of antibody binding under the presence of ACEO shows that the spatial distribution is virtually homogeneous across the electrode - something clearly not seen in the fluorescent images. (Figure IV-3). In this case, ACEO does not seem to be capable of causing the IgG patterning. Furthermore, DEP force is proportional to gradient of electric field squared. A simulation of this force matches the IgG binding quite well, as shown in Figure IV-4. Here, then, is an indication of the presence of DEP-induced binding.

It is possible that both forces are responsible for the patterning – that DEP can pattern IgG but only when it is very near the electrode corner and that ACEO is instrumental in bringing the IgG close.

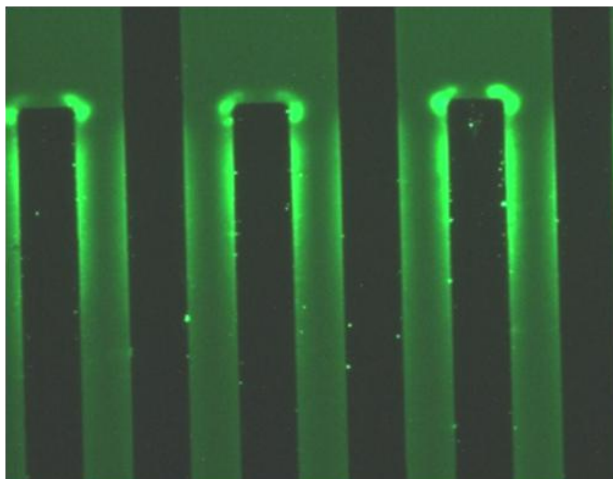
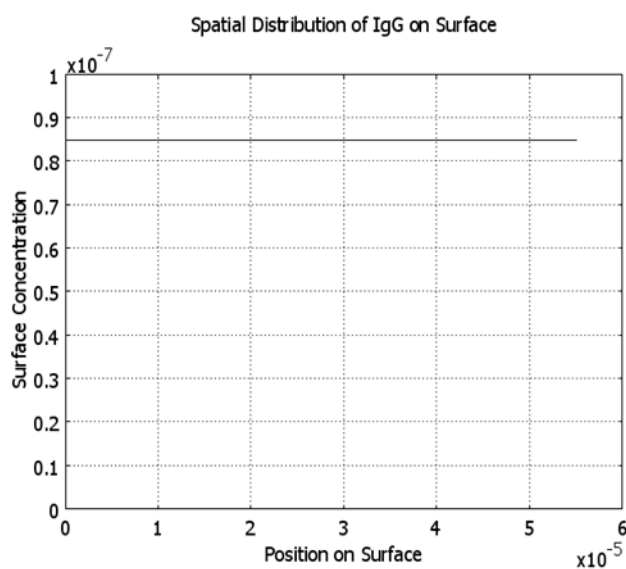


Figure 5-10: Spatial distribution of deposited IgG. Top: Simulated surface concentration as a function of position on an electrode surface. Bottom: Image of accumulated IgG on the surface of interdigitated electrodes under the presence of AC Electrokinetics.

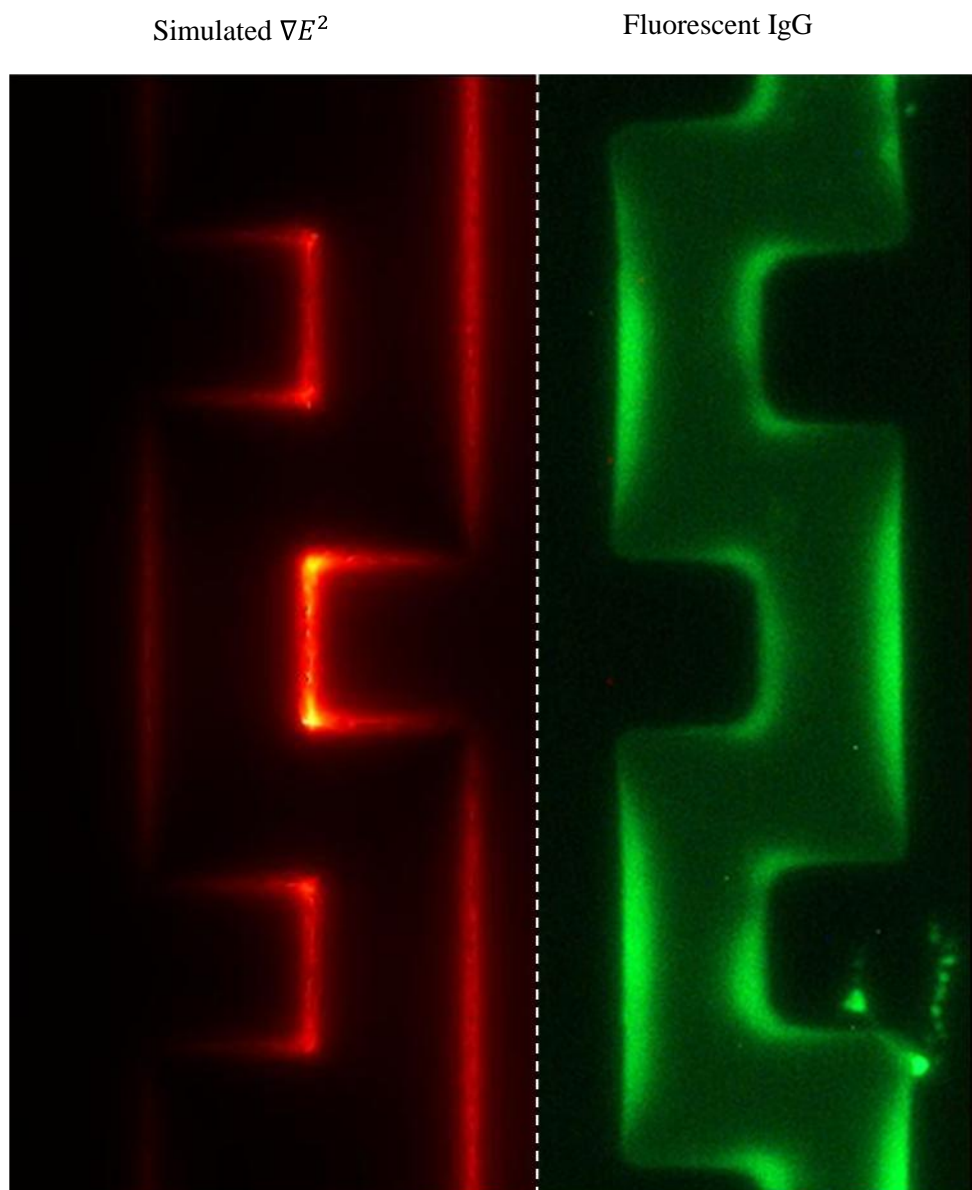


Figure 5-11: Comparison of a simulated gradient of electric field squared with fluorescent imaging of IgG on a castellated electrode that was incubated in the presence of AC electrokinetic forces.

Another alternative is that there is a type of electrophoresis occurring. The frequencies used are generally very low, 1 kHz or less, which may allow for electrostatic forces to drag the IgG to the electrode surface when the potential swings to the opposite value of the IgG resting charge. Once the IgG is bound to the surface, the ensuing potential switch does not dislodge it. To test this, a DC shift was applied to an electrode while reacting with IgG. The electrodes were unfortunately quickly destroyed by this DC shift, even when the shift was 1 mV. An image of this damage is shown in Figure IV-5. This investigation will remain as future work.

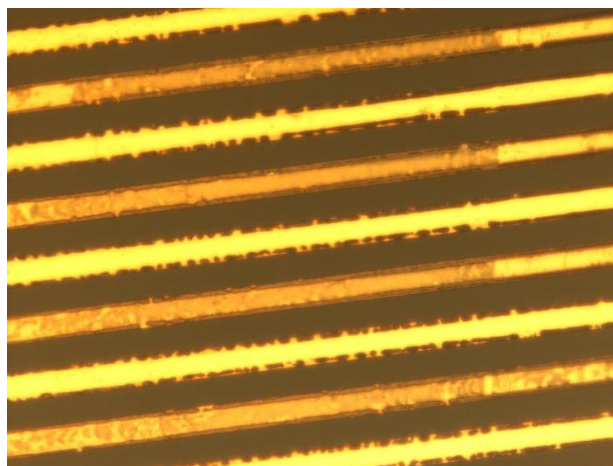


Figure 5-12: Image of electrode damage due to 10 mV DC offset to 100 Hz, 1 V_{pp} AC signal.

APPENDIX VII - PSEUDOCODE FOR RESONANCE FREQUENCY MEASUREMENT SOFTWARE IN LABVIEW

A computer equipped with LabView was connected to a Network Analyzer HP4395a with a GPIB connection and custom software was coded in order to determine the resonance frequency of a QCM in air.

LabView is a graphical programming language and the code cannot be inserted into this document for reference. However, a pseudo-code as well as selected images is shown below.

```

-----
-----
%%% Establish connection and set measurement properties %%%
Open_Connection_to_HP4395A;
Set_4395A_to_Network_Analyzer_Mode;
Set_4395A_Measurement = S21;
Set_4395A_number_of_points = 201;
Set_4395A_IFbandwidth = 1000;
Set_4395A_Channel_1 = amplitude;
Set_4395A_Channel_2 = phase;
Set_4395A_Dual_Display_mode;
%%% Find resonance frequency - progressively smaller scans%%%
    %%% First 2 scans use maximum amplitude, second 2 use phase
%%%
%%% sweep 1 100 khz span %%%
NA_Center_Frequency = 10000000;
NA_Bandwidth = 100000;
fResonance = Channel_1 Target1_search_max;
%%% sweep 2 10 khz span %%%
NA_Center_Frequency = fResonance;
NA_Bandwidth = 10000;
fResonance = Channel_1 Target1_search_max;
%%% sweep 3 1 khz span %%%
NA_Center_Frequency = fResonance;
NA_Bandwidth = 1000;
Data=(Channel_2_phaseData,frequencyData);
fitParameters = Do_linear_fit on Data(middle 100 points);

```

```
fResonance = 0_crossing(fitParameters);  
%%% sweep 4 100 Hz span %%%  
NA_Center_Frequency = fResonance;  
NA_Bandwidth = 100;  
Data=(Channel_2_phaseData,frequencyData);  
fitParameters = Do_linear_fit on Data(middle 100 points);  
fResonance = 0_crossing(fitParameters);  
Return fResonance;
```

```
-----  
-----
```


APPENDIX VIII - COMSOL MATLAB CODE FOR ACEO- ENHANCED BINDING FOR HETEROGENEOUS IMMUNOASSAYS

```

function [equilibriumTime boundMass initialRate
rate]=Binding9(volts,eSize,gSize,chamberHeight, simTime,
c0,kads,kdes,D,theta0,stopRate, timeStep)

electrodeSize=eSize*1E-6;
gapSize=gSize*1E-6;
chamberHeight=chamberHeight*1E-6;
chamberWidth=electrodeSize/2+gapSize/2;

% COMSOL Multiphysics Model M-file
% Generated by COMSOL 3.5a (COMSOL 3.5.0.603, $Date: 2008/12/03
17:02:19 $)

    flclear fem

% COMSOL version
clear vrsn
vrsn.name = 'COMSOL 3.5';
vrsn.ext = 'a';
vrsn.major = 0;
vrsn.build = 603;
vrsn.rcs = '$Name: $';
vrsn.date = '$Date: 2008/12/03 17:02:19 $';
fem.version = vrsn;

% Constants
fem.const = {'c0',num2str(c0),... '1E-4 [mol/m^3]', ...
'kads',num2str(kads),... '1E2 [m^3/mol/s]', ...
'kdes',num2str(kdes),... '1E-3 [1/s]', ...
'theta0',num2str(theta0),... '1E-7 [mol/m^2]', ...
'Ds','1E-9', ...
'D',num2str(D),... '1e-11 [m^2/s]', ...
'v_max','1.0 [mm/s]', ...
'delta','0.1 [mm]', ...
'T','300 [K]', ...
'u_ave','0.1 [mm/s]', ...
'epsilon_f','epsilon_r_f*epsilon0', ...
'eta_f','1.08e-3', ...
'vrms',num2str(volts/sqrt(8)), ...

```

```

'epsilon_r_f', '80.2', ...
'epsilon_0', '8.854188e-12', ...
'Kp', '10^11/1.764*(1.4/298/10^5)^0.5', ...
'omega', '2*pi*freq', ...
'freq', '1000', ...
'tau', 'epsilon_f/sigma_f', ...
'sigma_f', '0.0002', ...
'w', num2str(chamberWidth), ...
'po', num2str(electrodeSize/2), ...
'chamberHeight', num2str(chamberHeight), ...
'gap', num2str(50) });

% Geometry

g1=rect2('w', num2str(chamberHeight), 'base', 'corner', 'pos', {'0', '0'
'}, 'rot', '0', 'const', fem.const);
parr={point2(electrodeSize/2,0)};
g2=geomcoerce('point', parr);

% Analyzed geometry
clear p s
p.objs={g2};
p.name={'PT1'};
p.tags={'g2'};

s.objs={g1};
s.name={'R1'};
s.tags={'g1'};

fem.draw=struct('p', p, 's', s);
fem.geom=geomcsg(fem);

% Initialize mesh
fem.mesh=meshinit(fem, ...
    'hauto', 5, ...
    'hmaxedg', [2, .5E-6, 4, .5E-6], ...
    'hgradedg', [2, 1.1, 4, 1.1]);

% (Default values are not included)

% Application mode 1
clear appl
appl.mode.class = 'GeneralLaminarFlow';
appl.module = 'MEMS';
appl.gporder = {4, 2};
appl.cporder = {2, 1};
appl.sshape = 2;
appl.assignsuffix = '_mmglf';
clear prop

```

```

prop.analysis='static';
prop.weakcompflow='Off';
appl.prop = prop;
clear pnt
pnt.pnton = {0,1};
pnt.ind = [1,1,2,1,1];
appl.pnt = pnt;
clear bnd
bnd.uw0 = {0,'EOS',0};
bnd.type = {'walltype','walltype','sym'};
bnd.walltype = {'noslip','semislip','noslip'};
bnd.isViscousSlip = {1,0,1};
bnd.ind = [3,2,1,1,3];
appl.bnd = bnd;
clear equ
equ.eta = 'mat1_eta(T[1/K])[Pa*s]';
equ.gporder = {{1;1;2}};
equ.rho = 'mat1_rho(T[1/K])[kg/m^3]';
equ.cporder = {{1;1;2}};
equ.shape = [1;2;3];
equ.gamma = 'mat1_gamma';
equ.sigma = 'mat1_sigma';
equ.ind = [1];
appl.equ = equ;
fem.appl{1} = appl;

% Application mode 2
clear appl
appl.mode.class = 'FlConvDiff';
appl.sshape = 2;
appl.assignsuffix = '_cd';
clear prop
clear weakconstr
weakconstr.value = 'off';
weakconstr.dim = {'lm6'};
prop.weakconstr = weakconstr;
appl.prop = prop;
clear bnd
bnd.N = {0,'-react_surf'};
bnd.type = {'N0','N'};
bnd.ind = [1,2,1,2,1];
appl.bnd = bnd;
clear equ
equ.D = 'D';
equ.init = 'c0';
equ.v = 'v';
equ.u = 'u';
equ.ind = [1];
appl.equ = equ;
fem.appl[116] = appl;

```

```

% Application mode 3
clear appl
appl.mode.class = 'FlPDEWBoundary';
appl.dim = {'cs','cs_t'};
appl.sshape = 2;
appl.assignsuffix = '_wb';
clear prop
clear weakconstr
weakconstr.value = 'off';
weakconstr.dim = {'lm7','lm8'};
prop.weakconstr = weakconstr;
appl.prop = prop;
clear bnd
bnd.usage = {0,1};
bnd.weak = {0,'Ds*(-test(csTx)*csTx-
test(csTy)*csTy)+test(cs)*(react_surf-cst)'};
bnd.ind = [1,2,1,2,1];
appl.bnd = bnd;
fem.appl[116] = appl;
fem.frame = {'ref'};
fem.border = 1;
clear units;
units.basesystem = 'SI';
fem.units = units;

% Boundary settings
clear bnd
bnd.ind = [1,2,1,2,1];
bnd.dim = {'u','v','p','lmx_mmglf','lmy_mmglf','c','cs'};

% Boundary expressions
bnd.expr = {'react_surf',{'','kads*c*(theta0-cs)-kdes*cs'}};
fem.bnd = bnd;

% Scalar expressions
fem.expr =
{'EOScenter','1/8*epsilon_f/eta_f*(vrms)^2*G1^2/(x-
w)/(1+G1^2)^2', ...
'G1','0.5*pi*(x-w)*Kp*omega*tau', ...
'Grightright','0.5*pi*(x-3*w)*Kp*omega*tau', ...
'EOSright','1/8*epsilon_f/eta_f*(vrms)^2*Grightright^2/(x-
3*w)/(1+Grightright^2)^2', ...
'EOS','EOScenter+EOSleft', ...
'Gleft','0.5*pi*(x+w)*Kp*omega*tau', ...
'EOSleft','1/8*epsilon_f/eta_f*(vrms)^2*Gleft^2/(x+w)/(1+Gleft^2)
^2'};

% Coupling variable elements

```

```

clear elemcpl
% Integration coupling variables
clear elem
elem.elem = 'elcplscalar';
elem.g = {'1'};
src = cell(1,1);
clear bnd
bnd.expr =
{{{},'cs/w/c0/chamberHeight'},{{{},'cst/w/c0/chamberHeight'} }};
bnd.ipoints = {{{},'4'},{{{},'4'}}};
bnd.frame = {{{},'ref'},{{{},'ref'}}};
bnd.ind = {'1','3','5'},{'2','4'};
src{1} = {{{},bnd,{{{}}};
elem.src = src;
geomdim = cell(1,1);
geomdim{1} = {};
elem.geomdim = geomdim;
elem.var = {'bound_mass','rate'};
elem.global = {'1','2'};
elemcpl{1} = elem;
fem.elemcpl = elemcpl;

% Descriptions
clear descr
descr.const=
{'D','Mass','kdes','Mass','u_ave','Fluid','epsilon_r_f','ACEO','v_
max','Mass','epsilon_f','ACEO','freq','ACEO','theta0','Mass','del
ta','Channel
width','vrms','ACEO','omega','ACEO','kads','Mass','Kp','ACEO','T'
,'Fluid','sigma_f','ACEO','Ds','Mass','eta_f','ACEO','tau','ACEO'
,'c0','Mass','epsilon0','ACEO'};
fem.descr = descr;

% Library materials
clear lib
lib.mat{1}.name='Water, liquid';
lib.mat{1}.varname='mat1';
lib.mat{1}.variables.nu0='nu0(T[1/K]) [m^2/s]';
lib.mat{1}.variables.eta='eta(T[1/K]) [Pa*s]';
lib.mat{1}.variables.gamma='1.0';
lib.mat{1}.variables.sigma='5.5e-6[S/m]';
lib.mat{1}.variables.C='Cp(T[1/K]) [J/(kg*K)]';
lib.mat{1}.variables.rho='rho(T[1/K]) [kg/m^3]';
lib.mat{1}.variables.k='k(T[1/K]) [W/(m*K)]';
lib.mat{1}.variables.cs='cs(T[1/K]) [m/s]';
clear fcns
fcns{1}.type='interp';
fcns{1}.name='cs';
fcns{1}.method='piecewisecubic';
fcns{1}.extmethod='const';

```

```

fcns{1}.x={'273','278','283','293','303','313','323','333','343',
'353', ...
        '363','373'};

fcns{1}.data={'1403','1427','1447','1481','1507','1526','1541','1
552', ...
            '1555','1555','1550','1543'};
fcns[116].type='piecewise';
fcns[116].name='rho(T)';
fcns[116].extmethod='const';
fcns[116].subtype='poly';

fcns[116].expr={{'0','8.38466135E+02','1','1.40050603E+00','2',
...
                '-3.01123760E-03','3','3.71822313E-07'}};
fcns[116].intervals={'273.15','553.75'};
fcns[116].type='piecewise';
fcns[116].name='Cp(T)';
fcns[116].extmethod='const';
fcns[116].subtype='poly';
fcns[116].expr={{'0','1.20101471E+04','1','-
8.04072879E+01','2', ...
                '3.09866854E-01','3','-5.38186884E-04','4','3.62536437E-
07'}};
fcns[116].intervals={'273.15','553.75'};
fcns[116].type='piecewise';
fcns[116].name='eta(T)';
fcns[116].extmethod='const';
fcns[116].subtype='poly';
fcns[116].expr={{'0','1.3799566804E+00','1','-2.1224019151E-
02','2', ...
                '1.3604562827E-04','3','-4.6454090319E-
07','4','8.9042735735E-10','5', ...
                '-9.0790692686E-13','6','3.8457331488E-
16'}},{'0','4.01235783E-03','1', ...
                '-2.10746715E-05','2','3.85772275E-08','3','-2.39730284E-
11'}};
fcns[116].intervals={'273.15','413.15','553.75'};
fcns{5}.type='piecewise';
fcns{5}.name='nu0(T)';
fcns{5}.extmethod='const';
fcns{5}.subtype='poly';
fcns{5}.expr={{'0','1.3903230155E-03','1','-2.1392545737E-
05','2', ...
                '1.3717187260E-07','3','-4.6851166702E-
10','4','8.9823339887E-13','5', ...
                '-9.1602964729E-16','6','3.8807189536E-
19'}},{'0','1.36222834E-06','1', ...
                '-4.45388688E-09','2','4.04364450E-12'}};

```

```

fcns{5}.intervals={'273.15','413.15','553.75'};
fcns{6}.type='piecewise';
fcns{6}.name='k(T)';
fcns{6}.extmethod='const';
fcns{6}.subtype='poly';
fcns{6}.expr={{'0','-8.69083936E-01','1','8.94880345E-
03','2', ...
    '-1.58366345E-05','3','7.97543259E-09'}};
fcns{6}.intervals={'273.15','553.75'};
lib.mat{1}.functions = fcns;
lib.matgroups{1}.name='Resistivity';
lib.matgroups{1}.variables={'alphares','T0','res0'};
lib.matgroups{1}.descr={'Temperature coefficient','Reference
temperature','Resistivity at reference temperature'};

fem.lib = lib;

% ODE Settings
clear ode
clear units;
units.basesystem = 'SI';
ode.units = units;
fem.ode=ode;

% Multiphysics
fem=multiphysics(fem);

% Extend mesh
fem.xmesh=meshextend(fem);

% Solve problem
fem.sol=femstatic(fem, ...
    'u',0, ...
'solcomp',{'v','u','lmx_mmglf','p','lmy_mmglf'}, ...
'outcomp',{'v','u','p','lmx_mmglf','lmy_mmglf'}, ...
    'blocksize','auto', ...
    'hnlm','on', ...
    'linsolver','gmres', ...
    'uscale','none');

% Save current fem structure for restart purposes
fem0=fem;

% (Default values are not included)

% Application mode 1

```

```

clear appl
appl.mode.class = 'GeneralLaminarFlow';
appl.module = 'MEMS';
appl.gporder = {4,2};
appl.cporder = {2,1};
appl.sshape = 2;
appl.assignsuffix = '_mmglf';
clear prop
prop.analysis='static';
prop.weakcompflow='Off';
appl.prop = prop;
clear pnt
pnt.pnton = {0,1};
pnt.ind = [1,1,2,1,1];
appl.pnt = pnt;
clear bnd
bnd.uw0 = {0,'EOS',0};
bnd.type = {'walltype','walltype','sym'};
bnd.walltype = {'noslip','semislip','noslip'};
bnd.isViscousSlip = {1,0,1};
bnd.ind = [3,2,1,1,3];
appl.bnd = bnd;
clear equ
equ.eta = 'mat1_eta(T[1/K])[Pa*s]';
equ.gporder = {{1;1;2}};
equ.rho = 'mat1_rho(T[1/K])[kg/m^3]';
equ.cporder = {{1;1;2}};
equ.shape = [1;2;3];
equ.gamma = 'mat1_gamma';
equ.sigma = 'mat1_sigma';
equ.ind = [1];
appl.equ = equ;
fem.appl{1} = appl;

% Application mode 2
clear appl
appl.mode.class = 'FlConvDiff';
appl.sshape = 2;
appl.assignsuffix = '_cd';
clear prop
clear weakconstr
weakconstr.value = 'off';
weakconstr.dim = {'lm6'};
prop.weakconstr = weakconstr;
appl.prop = prop;
clear bnd
bnd.N = {0,'-react_surf'};
bnd.type = {'N0','N'};
bnd.ind = [1,2,1,2,1];
appl.bnd = bnd;

```



```

clear equ
equ.D = 'D';
equ.init = 'c0';
equ.v = 'v';
equ.u = 'u';
equ.ind = [1];
appl.equ = equ;
fem.appl[116] = appl;

% Application mode 3
clear appl
appl.mode.class = 'FlPDEWBoundary';
appl.dim = {'cs', 'cs_t'};
appl.sshape = 2;
appl.assignsuffix = '_wb';
clear prop
clear weakconstr
weakconstr.value = 'off';
weakconstr.dim = {'lm7', 'lm8'};
prop.weakconstr = weakconstr;
appl.prop = prop;
clear bnd
bnd.usage = {0,1};
bnd.weak = {0, 'Ds*(-test(csTx)*csTx-
test(csTy)*csTy)+test(cs)*(react_surf-cst)'};
bnd.ind = [1,2,1,2,1];
appl.bnd = bnd;
fem.appl[116] = appl;
fem.frame = {'ref'};
fem.border = 1;
clear units;
units.basesystem = 'SI';
fem.units = units;

% Boundary settings
clear bnd
bnd.ind = [1,2,1,2,1];
bnd.dim = {'u', 'v', 'p', 'lmx_mmglf', 'lmy_mmglf', 'c', 'cs'};

% Boundary expressions
bnd.expr = {'react_surf', {'', 'kads*c*(theta0-cs)-kdes*cs'}};
fem.bnd = bnd;

% Scalar expressions
fem.expr =
{'EOScenter', '1/8*epsilon_f/eta_f*(vrms)^2*G1^2/(x-
w)/(1+G1^2)^2', ...
'G1', '0.5*pi*(x-w)*Kp*omega*tau', ...
'Gright', '0.5*pi*(x-3*w)*Kp*omega*tau', ...

```

```

        'EOSright','1/8*epsilon_f/eta_f*(vrms)^2*Gright^2/(x-
3*w)/(1+Gright^2)^2', ...
        'EOS','EOScenter+EOSleft', ...
        'Gleft','0.5*pi*(x+w)*Kp*omega*tau', ...

'EOSleft','1/8*epsilon_f/eta_f*(vrms)^2*Gleft^2/(x+w)/(1+Gleft^2)
^2'];

% Coupling variable elements
clear elemcpl
% Integration coupling variables
clear elem
elem.elem = 'elcplscalar';
elem.g = {'1'};
src = cell(1,1);
clear bnd
bnd.expr = {{{}, 'cs/w/c0/chamberHeight'}, {{{}, 'cst'} };
bnd.ipoints = {{{}, '4'}, {{{}, '4'}};
bnd.frame = {{{}, 'ref'}, {{{}, 'ref'}};
bnd.ind = {'1', '3', '5'}, {'2', '4'};
src{1} = {{{}, bnd, {{{}}};
elem.src = src;
geomdim = cell(1,1);
geomdim{1} = {};
elem.geomdim = geomdim;
elem.var = {'bound_mass', 'rate'};
elem.global = {'1', '2'};
elemcpl{1} = elem;
fem.elemcpl = elemcpl;

% Descriptions
clear descr
descr.const=
{'D', 'Mass', 'kdes', 'Mass', 'u_ave', 'Fluid', 'epsilon_r_f', 'ACEO', 'v_
max', 'Mass', 'epsilon_f', 'ACEO', 'freq', 'ACEO', 'theta0', 'Mass', 'del
ta', 'Channel
width', 'vrms', 'ACEO', 'omega', 'ACEO', 'kads', 'Mass', 'Kp', 'ACEO', 'T'
, 'Fluid', 'sigma_f', 'ACEO', 'Ds', 'Mass', 'eta_f', 'ACEO', 'tau', 'ACEO'
, 'c0', 'Mass', 'epsilon0', 'ACEO'};
fem.descr = descr;

% Library materials
clear lib
lib.mat{1}.name='Water, liquid';
lib.mat{1}.varname='mat1';
lib.mat{1}.variables.nu0='nu0(T[1/K]) [m^2/s]';
lib.mat{1}.variables.eta='eta(T[1/K]) [Pa*s]';
lib.mat{1}.variables.gamma='1.0';
lib.mat{1}.variables.sigma='5.5e-6[S/m]';
lib.mat{1}.variables.C='Cp(T[1/K]) [J/(kg*K)]';

```

```

lib.mat{1}.variables.rho='rho(T[1/K]) [kg/m^3]';
lib.mat{1}.variables.k='k(T[1/K]) [W/(m*K)]';
lib.mat{1}.variables.cs='cs(T[1/K]) [m/s]';
clear fcns
fcns{1}.type='interp';
fcns{1}.name='cs';
fcns{1}.method='piecewisecubic';
fcns{1}.extmethod='const';

fcns{1}.x={'273','278','283','293','303','313','323','333','343',
'353', ...
'363','373'};

fcns{1}.data={'1403','1427','1447','1481','1507','1526','1541','1
552', ...
'1555','1555','1550','1543'};
fcns[116].type='piecewise';
fcns[116].name='rho(T)';
fcns[116].extmethod='const';
fcns[116].subtype='poly';

fcns[116].expr={{'0','8.38466135E+02','1','1.40050603E+00','2',
...
'-3.01123760E-03','3','3.71822313E-07'}};
fcns[116].intervals={'273.15','553.75'};
fcns[116].type='piecewise';
fcns[116].name='Cp(T)';
fcns[116].extmethod='const';
fcns[116].subtype='poly';
fcns[116].expr={{'0','1.20101471E+04','1','-
8.04072879E+01','2', ...
'3.09866854E-01','3','-5.38186884E-04','4','3.62536437E-
07'}};
fcns[116].intervals={'273.15','553.75'};
fcns[116].type='piecewise';
fcns[116].name='eta(T)';
fcns[116].extmethod='const';
fcns[116].subtype='poly';
fcns[116].expr={{'0','1.3799566804E+00','1','-2.1224019151E-
02','2', ...
'1.3604562827E-04','3','-4.6454090319E-
07','4','8.9042735735E-10','5', ...
'-9.0790692686E-13','6','3.8457331488E-
16'}},{'0','4.01235783E-03','1', ...
'-2.10746715E-05','2','3.85772275E-08','3','-2.39730284E-
11'}};
fcns[116].intervals={'273.15','413.15','553.75'};
fcns{5}.type='piecewise';
fcns{5}.name='nu0(T)';
fcns{5}.extmethod='const';

```

```

    fcns{5}.subtype='poly';
    fcns{5}.expr={{'0','1.3903230155E-03','1','-2.1392545737E-
05','2', ...
    '1.3717187260E-07','3','-4.6851166702E-
10','4','8.9823339887E-13','5', ...
    '-9.1602964729E-16','6','3.8807189536E-
19'}},{'0','1.36222834E-06','1', ...
    '-4.45388688E-09','2','4.04364450E-12'}};
    fcns{5}.intervals={'273.15','413.15','553.75'};
    fcns{6}.type='piecewise';
    fcns{6}.name='k(T)';
    fcns{6}.extmethod='const';
    fcns{6}.subtype='poly';
    fcns{6}.expr={{'0','-8.69083936E-01','1','8.94880345E-
03','2', ...
    '-1.58366345E-05','3','7.97543259E-09'}};
    fcns{6}.intervals={'273.15','553.75'};
    lib.mat{1}.functions = fcns;
    lib.matgroups{1}.name='Resistivity';
    lib.matgroups{1}.variables={'alphanes','T0','res0'};
    lib.matgroups{1}.descr={'Temperature coefficient','Reference
temperature','Resistivity at reference temperature'};

fem.lib = lib;

% ODE Settings
clear ode
clear units;
units.basesystem = 'SI';
ode.units = units;
fem.ode=ode;

% Multiphysics
fem=multiphysics(fem);

% Extend mesh
fem.xmesh=meshextend(fem);

% Solve problem
fem.sol=femtime(fem, ...
    'u',fem0.sol, ...
    'solcomp',{'c','cs'}, ...
    'outcomp',{'v','u','c','lmx_mmglf','p','lmy_mmglf','cs'}, ...
    'blocksize','auto', ...
    'tlist',[colon(0,timeStep,simTime)], ...
    'estrat',1, ...
    'tout','tlist', ...

```

```

        'rtol',0.001, ...
        'tout','tlist', ...
        'tsteps', 'strict',...
        'uscale','none');%,...
    %'stopcond',['(rate-' num2str(stopRate)
    ')']);

    % Save current fem structure for restart purposes
    fem0=fem;

    % Plot solution
    % figure
    % postplot(fem, ...
    %
    % 'tridata',{'U_mmglf','cont','internal','unit','m/s'}, ...
    %         'trimap','Rainbow', ...
    %         'solnum','end', ...
    %         'title','Time=2000      Surface: Velocity field
    [m/s]', ...
    %         'axis',[-4.373801715491907E-5,7.87380180897341E-
    5,-4.999999873689376E-6,1.0499999734747689E-4]);
    %         title(num2str(volts*sqrt(8)));

    % figure
    %
    % Plot solution
    % postplot(fem, ...
    %
    % 'tridata',{'c','cont','internal','unit','mol/m^3'}, ...
    %         'trimap','Rainbow', ...
    %         'solnum','end', ...
    %         'title','Time=20      Surface: Concentration, c
    [mol/m^3]', ...
    %         'axis',[-3.7320552796974694E-5,7.232055373178974E-
    5,-4.999999873689376E-6,1.0499999734747689E-4]);
    %
    % figure
    %
    % Plot solution
    % postplot(fem, ...
    %
    % 'tridata',{'c','cont','internal','unit','mol/m^3'}, ...
    %         'trimap','Rainbow', ...
    %         'solnum','end', ...
    %         'title','Time=100      Surface: Concentration, c
    [mol/m^3]', ...
    %         'axis',[-3.7320552796974694E-5,7.232055373178974E-
    5,-4.999999873689376E-6,1.0499999734747689E-4]);
    %
    % figure

```

```

%      %
%      % Plot solution
%      postplot(fem, ...
%
%      'tridata',{'c','cont','internal','unit','mol/m^3'}, ...
%      'trimap','Rainbow', ...
%      'solnum','end', ...
%      'title','Time=1000      Surface: Concentration, c
[mol/m^3]', ...
%      'axis',[-3.7320552796974694E-5,7.232055373178974E-
5,-4.999999873689376E-6,1.0499999734747689E-4]);

%      Global variables plot
%      figure
%      postglobalplot(fem,{'bound_mass'}, ...
%      'title','bound_mass', ...
%      'axislabel',{'Time','bound_mass'});
%
%      mass=postglobaleval(fem,{'bound_mass'});
%      boundMass=[mass.y];

absMass=boundMass.*(electrodeSize+gapSize).*c0.*chamberHeight;
a = 0.1*size(mass.y);

rateStruct=postglobaleval(fem,{'rate'});
rate=[rateStruct.y];

initialRate=rate(1);
equilibriumTime = 0.1*size(find(rate>(initialRate*1E-3)),1);

end

```